ADVANCING NUCLEAR MAGNETIC RESONANCE SPECTROSCOPY USING QUANTUM SENSORS IN DIAMOND

by

DI WANG

(ORCID: 0000-0002-9656-5705)

A thesis submitted in total fulfillment for the degree

Doctor of Philosophy

on

June 2025

in the

School of Physics

Faculty of Science

The University of Melbourne

ABSTRACT

Nuclear magnetic resonance (NMR) spectroscopy is a cornerstone in modern-day science. Its applications span areas from molecular chemistry to medical sciences and even the search for dark matter. It hails success from being non-invasive to the target of interest, the ability to provide highly detailed molecular information and its versatility to study a wide range of samples in their natural form. However, its main weakness is the lack of sensitivity. The recent development in quantum sensing based on atomic-scale systems, namely the Nitrogen-Vacancy (NV) centre in diamond, has shown great promise in addressing the underbelly of conventional NMR. This thesis will extend the developments of NV-based NMR through various studies.

Chapter 1 encapsulates an overview of NMR, which discusses its working principles, advantages and limitations. Chapter 2 presents the fundamentals of the NV centre and the overall methodology of using it to perform NMR spectroscopy. It includes a survey of published reports relevant to NV NMR and discusses the key challenges, such as diffusion at the nanoscale, reduced coherence time and stability for near-surface NVs.

Chapter 3 presents a postprocessing protocol that improves nanoscale NV NMR experiments through readout optimisations. It outlines a photophysics model that is used to report sensory information and demonstrates an increase in NMR signal-to-noise (SNR) ratio of 36%. This protocol, unlike the common approach of diamond material engineering, does not have significant overheads and costs, the only one being the increase

in computation power, and it is capable of being extended to alternative NV-based experiments.

Chapter 4 investigates experiments involving an ensemble of NVs. The previously introduced postprocessing method is tested at the ensemble scale, and concluded that the limitations of this protocol are amplified. The performance of this protocol suffers from the lack of optical excitations, and a more accurate description of the photophysics is necessary. Chapter 4 then investigates the impacts of optical noise on ensemble NV NMR experiments. Two different lasers were used for a comparison study. The results show that despite having a laser profile that is an order of magnitude less noisy, the SNR of the measured NMR is only 25% higher. With supporting modelling, it is concluded that laser noise should not be the sole focal point when performing technical upgrades.

Chapter 5 presents the journey of building an NV NMR apparatus with high spectral resolution, which the previous chapters lacked due to information loss caused by nanoscale diffusion. The method uses the quantum heterodyne (Qdyne) protocol, and sub-Hz spectral resolution is demonstrated. It was found that at high spectral resolution, additional technical aspects of the apparatus need addressing. These include the impact of timing control and synchronicity, magnetic uniformity and stability, optical collection methods and materials considerations. The chapter ends on a plan to combine NV NMR with microfluidic-based flow chemistry, which opens the door for real-time in situ reaction monitoring. The final chapter of this thesis explores future directions of NV-based NMR, including the prospects of using Qdyne with diffusion noise and zero- to ultralow-field (ZULF) NMR.

DECLARATION

I, Di Wang, declare that this thesis titled, Advancing Nuclear Magnetic Resonance Spectroscopy using Quantum Sensors in Diamond and the work presented in it are my own. I confirm that:

- the thesis comprises only my original work towards the Doctor of Philosophy except where indicated in the preface;
- due acknowledgement has been made in the text to all other material used; and
- the thesis is fewer than the maximum word limit in length, exclusive of tables, maps, bibliographies and appendices as approved by the Research Higher Degrees Committee.

Signature

12 June 2025

Date

STATEMENT OF CONTRIBUTION

This thesis encapsulates experimental and computational works undertaken in the quantum sensing groups led by A/Prof. David Simpson in the School of Physics and Dr. Liam Hall in the School of Chemistry. Because of the group environment, some of the work presented in this thesis had inputs from other sources. Here, I state the contributions that I or others have had on the thesis.

Chapter 1 is a review of NMR spectroscopy based on existing literature. Chapter 2 introduces the NV sensor and its relation to NMR. It mainly serves as an introduction and motivation of the methods that are used later in the thesis and the current progress of the field. However, there are some experimental data shown in Chapter 2 to aid the introduction. These data are measured by me using the apparatus described in Chapter 5.

Chapter 3 details a postprocessing technique used to improve NV readout performance. The development of this protocol requires theoretical and computational work, which was modelled by me with inputs from Dr. Liam Hall and Dr. Sepehr Ahmadi. The work also required experimental data to support the model. These were measured using existing infrastructures in the quantum sensing group in the School of Physics, with adjustments from me to cater for this particular investigation, except for data presented in figure 3.2, which was measured by Dr. Alexander Wood. The diamond sample was supplied by the group through Dr. Alexander Healey. Postprocessing of the data through the new model was completed by me. The work in this chapter is submitted for publication.

Chapter 4 investigates NMR performance using an ensemble of NVs. In the first part of the chapter, I extend the modelling work from the previous chapter and used same experimental infrastructure. The ensemble NV diamond sample was supplied by the group through Dr. Alexander Healey. In the second part, I explored optical performance using two laser sources, one of which was directly purchased, and the second was purchased and required assembly that was done by Dr. Christopher Lew. The measurement was done using an existing widefield microscope in the quantum sensing group in the School of Physics, with modifications to fit the additional laser sources. The fitting process was done by me and Dr. Christopher Lew. The measurements and the subsequent modelling were conducted by me.

Chapter 5 describes the development of an NV NMR apparatus that can achieve high spectral resolution. The majority of this work is done in the School of Chemistry through the supervision of Dr. Liam Hall. The starting point to this project is an empty optical bench. I worked on the design, assembly and testing of this apparatus, including optomechanical parts, electrical parts and control and timing software. Later on, Dr. Sepehr Ahamdi, who joined the group during my PhD candidatur,e also supported the project. His contribution included the design of the microfluidic channels in section 5.8. Also, he, with Mr. Trent Ralph performed the magnetic field simulations in section 5.7.

PUBLICATIONS

D. Wang, S. Ahmadi, F. Meneses, A. A. Wood, D. A. Simpson, and L. T. Hall. “Readout optimisation for spin-based quantum sensing using the nitrogen vacancy centre in diamond” Accepted in: Journal of Physics D: Applied Physics

ACKNOWLEDGEMENTS

Throughout my candidature, I have had the pleasure of meeting amazing people who celebrated my ups and supported me through my downs. First, I would like to thank my supervisors, A/Prof. David Simpson and Dr. Liam Hall. Their generosity and pool of knowledge guided me through this journey, which I could not have done without. I still cannot believe how lucky I am to end up in their groups. I would also like to acknowledge Prof. Matthew Dolan, who chaired numerous committee meetings and made himself available if I needed him.

Throughout my PhD, I had the privilege of working in Melbourne, where a significant NV diamond community is located. I was able to interact with multiple groups spanning numerous institution and I would like to thank the community, which includes, but is not limited to, the following people. First thanks go to the past and present members of the Simpson group and the Hall group, Dr. Nikolai Dontschuk, Dr. Julia McCoey, Dr. Daniel McCloskey, Dr. Robert de Gille, Dr. Alexander Healey, Dr. Erin Grant, Dr. Sam Scholten, Dr. Mina Barzegaramiriolya, Dr. Christopher Lew, Dr. Fernando Menese, Dr. Eliza Rokhsat, Dr. Nadarajah Athavan, Alister Chew, Ella Walsh, Charlie Pattinson, Tuesday Couzens, Hunter Johnson, Trent Ralph, Angela Hermann, Galya Haim, Islay Robetson, Gabriel Abrahams, Avan Whaite, Jake Willett, Dhilan Vallury, Dr. Sepehr Ahmadi, Dr. Daniel Creedon, Dr. Mitchell Conway, Calire Dawson, Yang Li and people I regretfully forgot to mention. Thank you for putting up with me in the offices and labs, and much obliged for helping me when in need, whether professionally or personally. It has been an awesome working environment and a massive motivation for me to go to the university. Special shutout goes to Sepehr, who was involved in multiple projects with me. Thank you for listening to my constant complaints when the lab equipment did not meet my silly expectations. I would also like to thank the following people, A/Prof. Jean-Philippe Tetienne, Dr. David Broadway, Dr. Brett Johnson, Prof. Alistair Stacey, Dr. Scott Lille, Dr. Michael Barson, Dr. Alexander Wood, Prof. Brant Gibson and the rest of the Melbourne diamond community. I think one of the best aspects of working in NV diamond is that the field is not short of talented professionals and inspirational conversations. I feel extremely lucky to have so many closely located colleges throughout my PhD.

More thanks go to Spiro Gicev, Michael Jones, Nicolas Collins, Henry Tan and Russell Goldblatt, who are part of the masters and doctorate cohort. Many thanks to the School of Chemistry for welcoming us into your labs and offices, especially to the members of the nanoscience lab. Additionally, I would also like to acknowledge the involvement with two research centres, the exciton science centre and the quantum biotechnology centre. I would like to acknowledge the Australian Government, the University of Melbourne and the Laby Foundation for providing me with their generous scholarships and bursaries.

Lastly, I would like to thank my family. Huge thanks to Mum and Dad, who are always there when I need them; a great deal of family support was needed to go through a PhD, especially during a pandemic. Finally and most importantly to Yihan, I cannot thank you enough for your loving care. This could not be achieved without you.

CONTENTS

Part I

INTRODUCTION

This part of the thesis serves as an introduction to the existing NMR landscape. Chapter 1 introduces NMR spectroscopy to the reader, including the history, the working principles, and technical aspects. It concludes with a discussion of the hallmark NMR problem, sensitivity. Chapter 2 presents the NV centre in diamond, which has the potential to boost NMR sensitivity. Chapter 2 will introduce the NV centre and explainthe protocols that lead up to NMR spectroscopy. It will end on the current limitations of NV NMR, which the rest of the thesis aims to address.

1

INTRODUCTION TO NMR

In today's world, gaining knowledge largely hinges on the scientific method. The formulation and verification of scientific theories are fundamental to research practices, highlighting the necessity for precise and informative methods of evidence evaluation. Thus, the development of instruments to validate hypotheses is a key cornerstone of modern science.

In chemical and biological settings, one of the widely used instruments for hypothesis validation is the nuclear magnetic resonance (NMR) spectrometer. It provides accurate and specific information on molecular structures, which is useful for a vast span of applications, and its implications extend from impacting our daily lives through the invention of magnetic resonance imaging (MRI) to understanding the far reaches of the universe.

The opening chapter of the thesis will focus on NMR spectroscopy. It begins with a historical journey from its discovery to its present-day influence. Then followed by a discussion of its working principle, applications, advantages over other techniques and its limitations.

1.1 HISTORY OF NMR

The story begins in 1921, when Otto Stern conceived an experiment testing the Bohr-Sommerfeld atomic model, which hypothesised the quantised nature of an atom's angular momentum. In February 1922, Otto Stern and Walther Gerlach at the Goethe University Frankfurt passed a beam of silver atoms through a magnetic field and measured the deflections of the atoms. The results revealed a set of discrete deflections, proving the quantised nature of angular momentum in atomic systems [57]. It was later found that the deflections were caused by the quantised electronic spins.

In 1932, Otto Stern performed a similar experiment and measured the magnetic moment of a proton for the first time [53]. Stern was subsequently awarded the Nobel Prize in Physics in 1943. In 1937, Isidor Rabi at Columbia University performed a modified version of Stern's experiment by using oscillating magnetic fields at a fixed frequency. By sweeping the strength of the static magnetic field, Rabi discovered that there is a resonant condition where the magnetic moment of the nuclear spin can be flipped [133]. Rabi called this phenomenon nuclear magnetic resonance and was awarded the Nobel Prize in physics in 1944.

In December 1945 and January 1946, two independent groups of physicists led by Edward Purcell at Harvard University and Felix Bloch at Stanford University measured the same resonance phenomenon in solids and liquids instead of molecular beams [20, 129]. Purcell and Bloch shared the Nobel Prize in physics in 1952.

It was in the 1950s that people started to realise that NMR can be used as a spectroscopic tool to solve problems in chemistry. Together with developments in condensed matter physics that enabled superconducting magnets, electronics that enabled sophisticated coil design and computing that enabled numerical

Fourier analysis, NMR started to transform from a physicist's tool to study atomic science to a gold standard in chemical elucidation. One significant step along this journey is the development of pulsed and multidimensional NMR spectroscopy. Erwin Hahn [70] (University of California, Berkeley) and others have contributed to the development of pulsed NMR spectroscopy and Richard Ernst (ZTH Zurich) [88], who was awarded the Nobel prize in chemistry in 1991, played a significant role in pioneering the Fourier transform (FT) NMR spectroscopy. These works enabled an increase in sophistication in the NMR spectra obtained that can be used to fingerprint organic molecules with high chemical specificity.

Besides physics and chemistry, NMR also has uses in biology and medicine. A method that uses the nuclear overhauser effect (NOE) NMR spectroscopy (NOESY) pioneered by Kurt Wuthrich in ZTH Zurich allows for the determination of 3D structures in proteins by tracking the transfer of spin polarisation to adjacent atoms. This can be used to reverse engineer the spatial information of biomolecules, such as the 3D structure in solution. Along with X-ray crystallography, NMR is one of the most used tools in biology to experimentally determine biological structures [170]. Wuthrich was awarded the Nobel Prize in Chemistry in 2002.

By introducing magnetic field gradients to encode spatial information into frequency, NMR images (MRI) can be obtained. This can be used to image bones, organs, muscles and blood in a non-invasive manner. Paul Lauterbur (University of Illinois) and Sir Peter Mansfield (University of Nottingham) were awarded the Nobel prize in physiology or medicine 2003 for their development of MRI [90, 107].

Solid-state NMR (ssNMR) and dynamical nuclear polarisation (DNP) have also begun attracting attention in the past few decades. By transferring highly polarised electron spins to nuclear spins, DNP has the capability to help NMR spectroscopy measure targets with weak signals. When coupled with ssNMR, it has found uses in material science such as solar cells, high temperature superconducting materials and a new field called NMR crystallography has emerged [2, 46, 103, 112, 159]. In the past few years, developments using zero- to ultralow-field (ZULF) NMR have emerged that have promising outlooks in a new way of chemical structure determination, such as dark matter detection, which can be further boosted by particle accelerator coupled radiation-detected NMR (RDNMR) [36] and using J-spectroscopy to study chemical exchange and chirality [11]. NMR is still a rapidly expanding field in the present day, and in this thesis, I will demonstrate how quantum technology can play a role in this evolving landscape.

1.2 WORKING PRINCIPLES AND APPLICATIONS OF NMR

1.2.1 *The nuclear spin*

The underlying physics of NMR relies on the spin properties of the nuclei of interest, and the spin number has to be non-zero. The nucleon composition (protons and neutrons; antiprotons and antineutrons are not considered in this thesis) of the nucleus determines the spin number (I). For a nucleus with an odd number of nucleons, spin number is fractional (for example, ^{1}H, $I = 1/2$; ^{11}B, $I = 3/2$), for an even number of nucleons with an odd number of protons or neutrons, I is an integer (^{14}N,

$I = 1$). In the case of an even number of nucleons and an even number of protons and neutrons, $I = 0$ (^{12}C,^{16}O), which implies that they are not NMR active [68].

Most NMR applications deal with $I = 1/2$ species, which include ^{1}H and ^{13}C that are common in life sciences. For $I > 1/2$, the NMR complexity increases as the spatial charge distribution becomes nonspherical, which allows the interaction with an electric field gradient [148], characterised by the electric quadrupole moment (eQ). This interaction causes NMR line broadening, which limits the information obtained. This effect becomes more significant when the local molecular symmetry is lowered.

The broadening is caused by an increase in relaxation rate induced by the electric field gradients (more details to follow). The upside of this feature is that it allows for nuclear quadrupole resonance (NQR), which is similar to NMR, that does not require a magnetic field, and its sensitivity also does not depend on the magnetic field. NQR spectroscopy is commonly used for solid-state materials in trace analysis [72]. However, there are some $I > 1/2$ isotopes with a relatively lower electric quadrupole moment that do not get affected by line broadening as much, such as ^{6}Li.

Other NMR-related spin properties of the nuclei are the natural isotopic abundance and the gyromagnetic ratio (γ). If artificial isotopic enrichment is not used, an isotope with low abundance will exhibit a lower signal [68]. An important example of this is carbon, where the NMR active ^{13}C has a natural abundance of 1.1% with the remaining being non-NMR active ^{12}C or the other unstable isotopes. The gyromagnetic ratio is a proportional constant between the magnetic moment of an isotope and its angular momentum. A higher $|\gamma|$ means a higher NMR signal, as higher $|\gamma|$ spins exhibit larger magnetic signals.

1.2.2 *NMR interactions*

When the NMR active nuclei is placed under a static magnetic field (B_0), it will undergo Zeeman splitting and create $2I+1$ quantised energy levels at $-\gamma m\hbar B_0$, where $m = -I, -I+1, \ldots, I-1, I$ and $\hbar$ is the reduced Planck's constant [150]. In addition to the Zeeman effect, other higher-order interactions are also present. The accurate evaluation of these energy levels forms the basis of NMR spectroscopy, because the origin of these higher-order effects is related to the local molecular environment [68].

Consider a spin-1/2 nucleus in a molecule under only a static magnetic field in the z-direction. Its Hamiltonian is given by

$$H_{NMR} = H_Z + H_{CS} + H_J + H_{other}, \tag{1}$$

where H_Z describes the Zeeman interaction, H_{CS} describes the chemical shift experienced by the local nuclei due to effects such as shielding, H_J is the local interaction between one nucleus and another within the molecule called J-coupling and H_{other} describes other higher order effects [150]. H_z is given by

$$H_Z/\hbar = -\gamma \hat{I}_z B_0, \tag{2}$$

where

$$\hat{I}_i = \frac{\hbar}{2}\sigma_i, \tag{3}$$

where σ_i are the Pauli matrices.

The chemical shift effects can be encapsulated in its Hamiltonian, given by

$$H_{CS}/\hbar = -\gamma \hat{\mathbf{I}} \cdot \boldsymbol{\sigma} \cdot \mathbf{B}_0, \tag{4}$$

where $\mathbf{B}_0$ is the static magnetic field vector and $\boldsymbol{\sigma}$ is the dimensionless chemical shift tensor. σ_{ij} represents the field created or induced towards the i direction when an external field in the j direction is applied. This effect is a consequence of the overall direction of the molecule with respect to the static field and the electron distribution around a nucleus, which can alter the effective field around a neighbouring atom.

The scale of chemical shift depends on the atomic mass [165]. In proton NMR, chemical shifts are on the order of 10 ppm of the static field, and heavier elements such as carbon can exhibit 200 ppm of chemical shift [68]. In organic chemistry, shielding effects can originate from the electronegativity of a particular atom. For example, a molecule with fluorine functional groups can draw the electron density of the other atoms towards the fluorine, increasing the other atoms' experienced field. Other chemical properties, such as resonance structures or hybridisation of electrons, can also affect chemical shift, hence this effect is critical to understanding the chemical properties of the target [68].

The J-coupling effect between nuclear spins 1 and 2 can be described by its interaction Hamiltonian, given by

$$H_J/\hbar = 2\pi \hat{\mathbf{I}}_1 \cdot \mathbf{J} \cdot \hat{\mathbf{I}}_2, \tag{5}$$

where **J** is the J-coupling tensor in frequency units. The origin of this effect is from the bonding electrons between adjacent atoms. Consider two atoms sharing two electrons through a covalent bond. If the first nuclear spin is in an aligned state, then its electron is energetically favoured to be anti-aligned, which means the other electron from the other atom that is in the bond will be aligned due to the Pauli exclusion principle, and hence the other nuclear spin will likely be anti-aligned. This creates a coupling between two nuclear spins that is mediated through its bond rather than space [68]. J-coupling can also be extended between more than one bond. The effect of J-coupling splits the energy levels and the NMR resonances.

J-couplings beyond the fourth bond are not usually detectable [104].

It is worth noting that the scale of J-coupling is not influenced by the external field; it is also known as the scalar coupling, and it is the dominating effect in the context of ZULF NMR [11]. Also, because the tensor is usually not time varying, unless there is a chemical exchange (for example, a reaction), ZULF NMR can be used to measure J-coupling changes to understand the dynamics of a reaction [12]. More information on ZULF NMR will be discussed in a later chapter. Usually, the scale of the J-coupling is around a few Hz for organic molecules and diminishes with increasing bond length. Because of this weak interaction, J-coupling is not usually easy to interpret for large molecules and proteins.

The Hamiltonians considered so far only concern a static picture of the target molecule. To understand the NMR effects of targets in solution (and in contrast to ssNMR), the motion averaging is discussed next. This is combined with the secular approximation, where, because a large static field is used, effects that are not aligned with B_0 are neglected.

The secular approximation does not apply to ZULF NMR.

To understand tumbling effects in solution and its contrast to ssNMR, consider the dipolar interaction between two nuclear spins and its Hamiltonian [149], given by

$$H_D/\hbar = \frac{\mu_0 \gamma_1 \gamma_2}{4\pi r^3} \hat{\mathbf{I}}_1 \cdot \mathbf{D} \cdot \hat{\mathbf{I}}_2, \tag{6}$$

where μ_0 is the permeability constant, r is the distance between the nuclear spins, and $\mathbf{D}$ is the dipolar interaction tensor, given by

$$\mathbf{D} = \begin{bmatrix} 1 - \sin^2\theta\cos^2\phi & 3\sin^2\theta\sin\phi\cos\phi & 3\sin\theta\cos\theta\cos\phi \\ 3\sin^2\theta\sin\phi\cos\phi & 1 - 3\sin^2\theta\sin^2\phi & 3\sin\theta\cos\theta\sin\phi \\ 3\sin\theta\cos\theta\cos\phi & 3\sin\theta\cos\theta\sin\phi & 1 - 3\cos^2\theta \end{bmatrix}. \tag{7}$$

Because the dipolar interaction is typically around 20 kHz compared to the Zeeman interaction of sub-GHz, the secular approximation can be applied [46], where only the components aligned to the external field are retained ($\hat{I}_z$), H_D is now given by

$$H_D/\hbar \approx \frac{\mu_0 \gamma_1 \gamma_2}{4\pi r^3}(3\cos^2\theta - 1)\hat{I}_{1z}\hat{I}_{2z}. \tag{8}$$

This is an important outcome for ssNMR, because dipolar coupling poses a significant unwanted linebroadening effect for solid state samples due to a diverse spread of interaction strengths within the solid state sample as r varies. Hence, techniques such as magic angle spinning (MAS) have been developed in ssNMR to reduce this effect, whereby spinning the sample at an angle where $\cos^2\theta = 1/3$ to the external field, the H_D effects can be minimised [46].

MAS-NMR usually spins the sample at usually up to ~10^5 rotations per second [104].

On the contrary, for an isotropic liquid state sample, motion averaging can be applied, because the molecular translational and rotational diffusions are fast and can be averaged out in the NMR timescales [94]. Hence, the angular average of H_D equals to zero as $\int_0^{2\pi}\int_0^{\pi}(3\cos^2\theta - 1)\sin\theta d\theta d\phi = \pi^2$, thus $\langle H_D \rangle = 0$. However, there is a caveat to note for motion averaging that at a very small scale (~ nm), it is valid to assume random diffusion, but at a larger scale, this is not valid as there is a spatial constraint, because the diffusion time increases with scale. However, because H_D~$1/r^3$, long-range interactions are not significant here.

Note that even when $\langle H_D \rangle = 0$, under motion averaging in space for liquids, it still affects the NMR process in the time domain as the stochastic variations in $H(t)$ cause spin relaxations (more details to follow).

In the chemical shift context, the secular approximation suggests that operators that do not commute with $\hat{I}_z$ will diminish. Motion tumbling implies that non-isotropic terms are averaged and only the trace of $\boldsymbol{\sigma}$ survives. The now reduced Hamiltonian under these approximations is given by [94]

$$H_{CS}/\hbar \approx \frac{-\gamma B_0}{3}\mathrm{tr}(\boldsymbol{\sigma}). \tag{9}$$

In ssNMR, where the motion tumbling is less prominent, the difference between σ_{xx}, σ_{yy} and σ_{zz} can be observed. This technique is called chemical shift anisotropy (CSA) and can be used to study the structures of solids and macromolecules [46].

In the J-coupling context, similar to chemical shift, motion tumbling reduces **J** to $\frac{\mathrm{tr}(\mathrm{J})}{3}$. And secular approximation removes all contributions from the off-diagonal terms [94], the reduced Hamiltonian is given by

$$H_J/\hbar \approx J\hat{I}_{1z}\hat{I}_{2z}. \tag{10}$$

Without secular approximation, there are still some surviving off-diagonal terms, and those can be studied in ZULF antisymmetric J-coupling experiments that can be used to investigate chiral molecules [85].

1.2.3 *Boltzmann distributions of nuclear spins*

Besides the Hamiltonian, the statistical behaviour of the samples is discussed next. NMR signals are usually considered to be weak; this is mostly caused by the Boltzmann distributions of nuclear spins [68]. Under a magnetic field, there will be a distribution of aligned and anti-aligned spins, and the net difference becomes the observable signal, which is given by

$$\frac{N_\uparrow}{N_\downarrow} = \exp(-\Delta E/k_B T), \tag{11}$$

where k_B is the Boltzmann constant, T is the temperature in Kelvin and $\Delta E = -\hbar\gamma B_0$ is the energy difference between the two states, therefore

$$\frac{N_\uparrow}{N_\downarrow} = \exp(-\hbar\gamma B_0/k_B T). \tag{12}$$

These results suggest that for a proton sample at 300 K and 1 T, only an excess of 2×10^{-5} portion of the spins contribute to the NMR signal. This is usually the reason that NMR is regarded as a relatively insensitive measurement and hence, there is a significant interest in developing techniques to overcome this constraint via hyperpolarisation (see section 1.3).

1.2.4 *Nuclear quadruple resonance*

The interactions discussed so far are only relevant to $I = 1/2$ spins. When $I > 1/2$, the nuclear quadrupole effect becomes dominant, and it is given by [94]

$$H_Q/\hbar = \frac{eQ}{2I(2I-1)}\hat{\mathbf{I}} \cdot \mathbf{V} \cdot \hat{\mathbf{I}}, \tag{13}$$

where e is the electron charge, Q is the nuclear quadrupolar moment in units of distance squared and $\mathbf{V}$ is the electric field gradient (EFG) tensor in volts per distance squared, comprised of second-order partial derivatives of the electric potential. Under motion averaging, the effects become zero, NQR is only used for solid-state samples. Also, H_Q does not depend on the static magnetic field, so it can used at a low field setting and its magnitude can reach up to MHz, which makes it a more sensitive technique in certain scenarios such as explosive detection in airports [72], because ΔE in equation 11 is only dependent on the EFG.

Secular approximation not always valid in NQR, because of NQR's high order of magnitude relative to the Zeeman effect [94].

The NMR effects discussed so far are commonly used in the present day. However, there exist other effects that are less used, but still relevant in NMR studies, such as spin-rotation effects

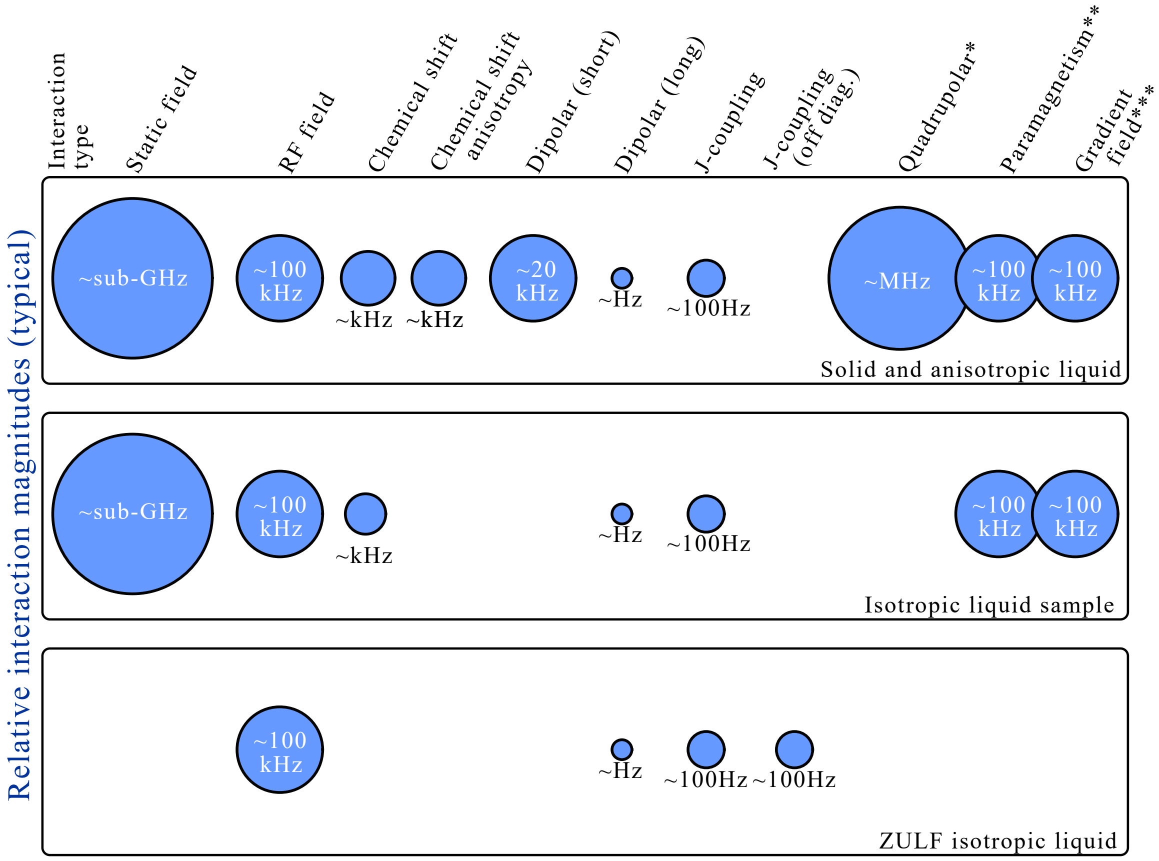

Figure 1.1: An illustration of the relevant interactions in NMR and their typical relative magnitudes in solid, liquid and ZULF environments. *Quadrupolar interactions are only available for samples with $I > 1/2$. **Paramagnetism is only available when paramagnetic substances such as radicals or metal complexes are present. ***Gradient fields are typically used in an MRI setting.

for gas state NMR and paramagnetic interactions for transition metals [94]. In MRI, field gradient effects are prominent too. The dominant effects for different NMR scenarios are summarised in Figure 1.1.

1.2.5 *Pulsed NMR spectroscopy*

So far, only the static properties of NMR systems in thermal equilibrium have been discussed. In order to describe modern NMR measurements, experiments with pulsed RF signals to drive these systems into non-equilibrium states and subsequent spin dynamics [69] will be introduced. The time-dependent Hamiltonian is then given by [150]

$$H_{RF}/\hbar = -\gamma \hat{I}_x \mathbf{B_1(t)}, \tag{14}$$

where $\mathbf{B_1(t)}$ is the oscillating RF field. It is given by

$$\mathbf{B_1(t)} = \begin{bmatrix} B_1(t)\cos(\omega t + \phi(t)) \\ 0 \\ 0 \end{bmatrix}, \tag{15}$$

where $B_1(t)$ is the magnitude of the RF field, typically around ~mT, hence H_{RF}~ sub-MHz and $\phi(t)$ is the phase of the pulse.

Similar approaches can be used in the Hilbert space, but it is less tedious in the Liouville space.

To understand the dynamical NMR processes with respect to RF pulse time t, the Liouville Von Neumann equation can be applied [49]. If an on resonance RF pulse is applied at the x-axis, the average expectation value for the spin operator is defined to be $\langle \hat{I}_i \rangle = \mathrm{tr}(\hat{\rho}\hat{I}_i)$, where $\hat{\rho}$ is the density operator and they are given by

$$\begin{aligned} \langle \hat{I}_x \rangle &= 0 && (16) \\ \langle \hat{I}_y \rangle &\propto \sin(\omega_1 t) && (17) \\ \langle \hat{I}_z \rangle &\propto \cos(\omega_1 t), && (18) \end{aligned}$$

where the proportionality factor is $\frac{\hbar\gamma B_0}{2k_B T}$. This implies that the RF pulse in the x direction causes a rotation around $\hat{I}_x$ at a rate of ω_1. And there exists a certain amount of RF pulse time where the $\langle\hat{I}_x\rangle$ and $\langle\hat{I}_z\rangle = 0$, this is known as a 90° or $\pi/2$ pulse where the spin operator is flipped onto the xy plane. When an on-resonance 90° pulse is applied at ω, the average expectation value for the spin operators after the pulse (t') is

$$\begin{aligned} \langle\hat{I}_x\rangle &= \frac{\hbar\gamma B_0}{4k_B T}\cos(\omega t') && (19)\\ \langle\hat{I}_y\rangle &= -\frac{\hbar\gamma B_0}{4k_B T}\sin(\omega t') && (20)\\ \langle\hat{I}_z\rangle &= 0. && (21) \end{aligned}$$

This suggests that at the xy plane, the spin vector will oscillate around the z axis at a rate of ω. This phenomenon is known as the Larmor precession. During an NMR experiment, the magnetisation (M) is measured, and it is given by $M_i = \gamma\hbar\rho\langle\hat{I}_i\rangle$, where ρ is the density of nuclear spins per unit volume.

By measuring the Lamor frequency after a 90° pulse using a Fourier transform (FT) on the detected magnetisation oscillations, the resonance frequency spectrum and the associated chemical information can be obtained. This is known as a free induction decay (FID) experiment [68], shown in figure 1.2a.

In NMR, M_z is not measured; the detection coils are designed to measure M_{xy}.

Pulse NMR spectroscopy was only popularised in the 1980s due to the advancement of computing technologies that allowed for digital Fourier transforms. Prior to this, continuous wave (CW) NMR was the standard procedure. This was achieved by sweeping the RF frequency at a fixed B_0 and monitoring for the resonance condition. However, compared to pulsed NMR, sweeping individual frequencies is a slow process [68, 104] and

It was cheaper to sweep the RF frequency than to change the current in the electromagnets for B_0.

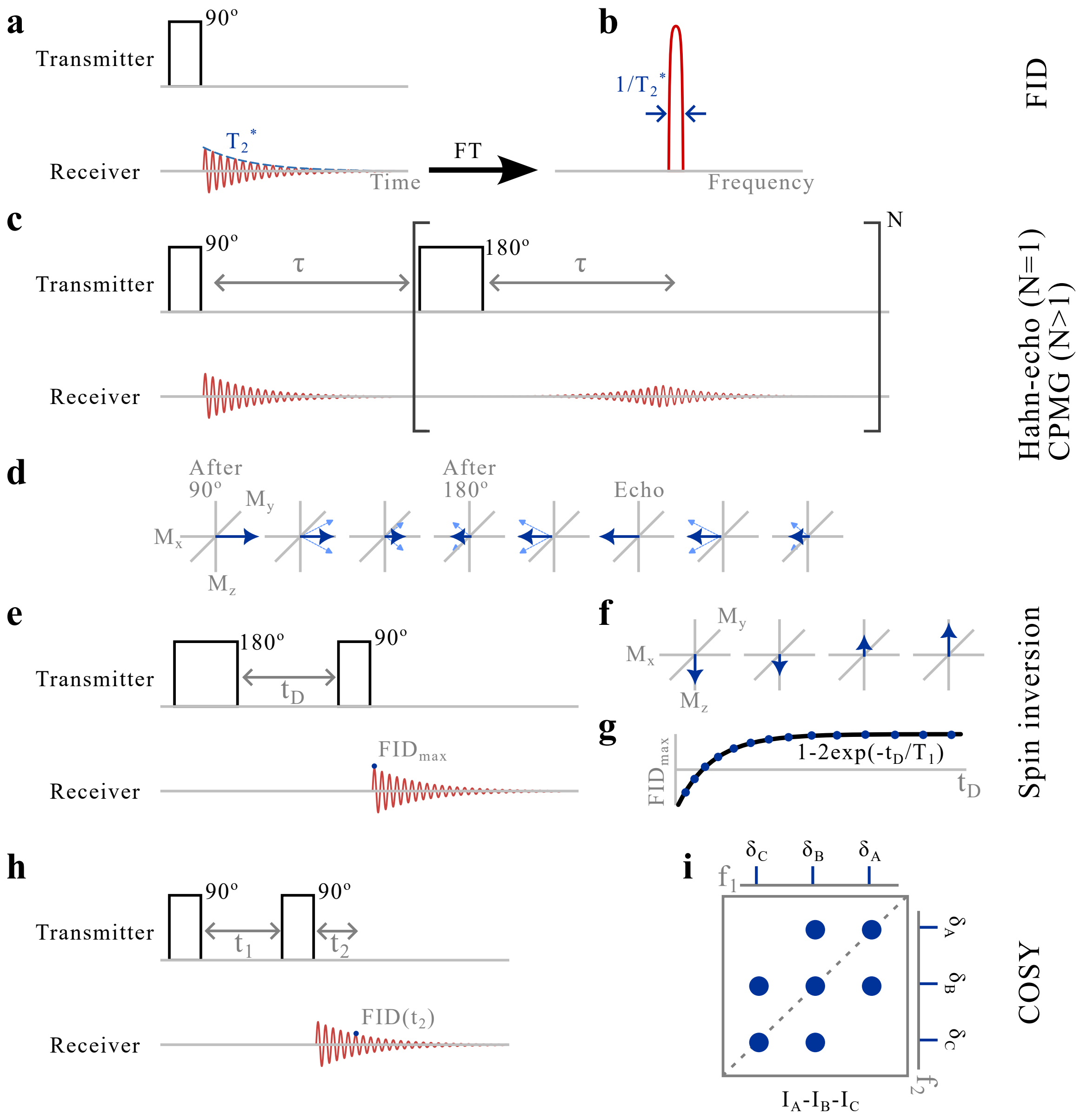
a
Transmitter
90°
Receiver
T_2^*
Time
FT
b
$1/T_2^*$
Frequency
FID
c
Transmitter
90°
τ
180°
τ
N
Receiver
Hahn-echo (N=1)
CPMG (N>1)
d
After 90°
M_y
M_x
M_z
After 180°
Echo
e
Transmitter
180°
t_D
90°
Receiver
FID_{max}
f
M_y
M_x
M_z
g
FID_{max}
$1-2\exp(-t_D/T_1)$
t_D
Spin inversion
h
Transmitter
90°
t_1
90°
t_2
Receiver
$FID(t_2)$
i
f_1
δ_C
δ_B
δ_A
δ_A
δ_B
δ_C
f_2
$I_A-I_B-I_C$
COSY

Figure 1.2

Figure 1.2: A collection of NMR pulse sequences. **a** shows a typical FID experiment. After a 90^o pulse, an oscillation at the Larmor frequency is picked up with a decay rate of $1/T_2^*$. A spectrum is shown in **b** by applying a Fourier transform to the measured FID. The linewidth is the inverse of the observed decay time. **c** shows an extension of the T_2^* using echos. This is achieved by applying a 180^o pulse at time τ after the initial pulse, and the echo appears at τ after the 180^o pulse. This is referred to as the Hahn-echo pulse sequence if one echo ($N = 1$) is measured and CPMG when more than one echos ($N > 1$) are induced. **d** shows the behaviour of M_{xy} during a Hahn-echo experiment. After the application of the 180^o pulse, there is a refocusing effect whereby flipping the M_{xy}, faster precessions are now behind the slower ones, and the signal begins to recover. **e** shows the spin inversion pulse sequence used to measure the T_1 decay time. An initial 180^o pulse is used to flip the magnetisation to the anti-aligned state. Then a subsequent FID experiment is applied, and the FID signal amplitude becomes proportional to M_z. By varying the delay time t_D between the pulses and tracking the FID amplitude, evolution of M_z illustrated in **f** can be measured as shown in **g**. Note that the direct measurement of M_z is not possible, so the FID experiment is used in spin inversion and the factor of 2 in **g** originates from the fact that T_1 is defined to be the relaxation from the xy plane to the +z direction and the measurement begins from the -z projection. **h** shows the pulse sequence for COSY. By applying two 90^o pulses, sweeping the interpulse duration t_1 and acquisition time t_2 and applying a double FT, a 2D NMR contour map can be achieved as exemplified in **i**. **i** shows an illustrative 2D COSY spectrum of a molecule containing spin I_i with chemical shift δ_i, where $i = A, B, C$. The example structure of the molecule indicates that spin I_A is coupled to I_B, but not to I_C. The COSY spectrum shows self-correlation at the diagonal positions and correction between I_A and I_B at the off-diagonal positions, but no I_A and I_C correlations.

it is inefficient because signal-to-noise ratio (SNR) scales as the square root of time.

1.2.6 *Relaxations in NMR:* T_1 *and* T_2 *effects*

To obtain meaningful information for an FT NMR spectrum, the linewidth needs to be on a comparable scale to the relevant energy of the target of interest. For example, small organic molecule NMR spectra need to have Hz resolution to identify J-coupling effects. The linewidth of an FT spectrum depends on the error rate of the oscillation. If the time domain information is infinitely long, the spectral linewidth will be infinitesimally narrow (from the definition of a delta function). However, if the signal has been truncated or decayed, as Larmor precession cannot last forever, the transformed spectral linewidth will broaden as a result. In the NMR context, to achieve Hz-scale spectral resolution, the magnetisation oscillation needs to have seconds-scale decay times, which is normally the case.

In a FID experiment, the decay time is usually thousands of ms, and the dominant decaying effect is the observed transverse relaxation (T_2^*), which can be extended to T_2 by applying more than one RF pulse (see a later subsection) [68]. The origin of this decay rate comes from the decoherence caused by a fluctuating local magnetic environment. This leads to an instantaneous variation of individual Larmor precessions, which on the macro scale leads to a measured decay in transverse magnetisation (M_{xy}). There also exists a dipolar interaction where the two spins exchange angular momentum (also known as spin-spin flip-flop) instantaneously, and this also adds to the transverse relaxation rate [94]. Static field inhomogeneities can also lead to an apparent transverse relaxation as variations in B_0 lead to variations in ω [94]. This inhomogeneity can be recovered by changing the direction of the magnetisation on the xy plane using additional RF pulses. And magnetic fluctuation slower than the addition pulse repetition rates will be suppressed, which includes the field inhomogeneities, thus extending T_2^* to T_2. Besides magnet and RF pulse engineering, NMR spectrometers physically spin the sample tube to counter this effect too [68].

In addition to transverse relaxation, longitudinal relaxation (T_1) can affect the measured signals. T_1 relaxation occurs when the magnetisation vector in the xy plane after the RF pulse begins to return to the energetically favoured z axis. The redistribution of the perturbed state back to the thermal state requires energy transfers. Thus, it depends on B_0 and T. Also, many other mechanisms can impact the energy transfer rate, such as molecular collisions, vibrations, interactions described in the previous hamiltonians, such as dipolar and quadrupolar interactions, but the dominant effect lies near the Larmor frequency [94]. For example, paramagnetic defects such as oxygen gas, radicals or gadolinium metal complexes cause fluctuations near the ω [68] or the diffusion, rotation and the size effects of the target may sometimes cause tumbling rate to be comparable to ω, for example fats and proteins have shorter relaxation times compared to smaller molecules [94]. Size also affects the motion averaging of certain terms of the Hamiltonian; for example, CSA effects are commonly studied in macromolecules [46].

Almost all T_2 effects occur with T_1 relaxation and generally $2T_1 \geqslant T_2$ [27]. In the context of spectroscopy, T_2 limits the linewidth, because the Larmor precession measurements are usually con-

There are debates surrounding the possibility of $T_2 > 2T_1$ *[145].*

ducted on the xy plane. However, T_1 also contains information, and there are pulse sequences designed to measure the longitudinal relaxation, such as the inversion recovery experiment (see figure 1.2f), and they are mostly used in MRI to distinguish water from fat, for example. In NMR spectroscopy, T_1 time also sets the lower limit between subsequent measurements, because the spins need sufficient time (usually $3T_1$) to recover to their thermal state prior to any subsequent pulsing.

1.2.7 *NMR pulse sequences*

The FID pulse sequence is one of the most basic forms of an NMR pulse sequence, and most modern-day operations are equipped with complex pulse designs, as FID is inherently limited by the T_2^* time. The transverse magnetisation is a macroscopic measurement, and when it is observed to be zero, it does not necessarily mean that all individual Larmor precessions are diminished. It is observed to be diminished because the local phases are different due to variation in local fields. This apparent loss in M_{xy} can be recovered by an extra 180^o RF pulse at τ time after the initial 90^o pulse. This effectively flips the M_{xy} and the faster precessions before the flip are now behind, and the slower ones begin to catch up (see figure 1.2d). This leads to the recovery of the observed magnetisation, and it occurs at τ time after the 180^o RF pulse, giving an additional signal and improving the spectral linewidth. This is commonly referred to as a Hahn-echo [70]. Other RF combinations, in addition to the 90-180-echo sequence, are also available in NMR. First, the duration of the pulse can be altered, for example, 90-90-echo is usually used in MRI. Then the number of pulses can be increased, such as the 90-180-echo-(180-echo)^N; this is known as the Car-Purcell-Meiboom-Gill (CPMG) echo train (see figure 1.2c) [68]. Depending on the electronics available in the spectrometer, the direction of the pulse (rotation around the y-axis instead of the x-axis) or the shape (sinc function-shaped pulse instead of square) can also be altered. In MRI or diffusion experiments, gradient fields are also used in sequences such as gradient echoes.

There are also multidimensional NMR pulse sequences that correlate bonding information of compounds within a molecule, such as the 2D correlation spectroscopy (COSY) (see figure 1.2h) [68]. By leveraging the NOE, protein scientists can, for example, transfer proton polarisation to adjacent nitrogen spins in amino acids and sequences such as the heteronuclear single quantum coherence (HSQC) or NOESY can be used to determine 3D protein structures [94].

1.2.8 *Spectrometer hardware: magnets and coils*

The engineering aspects of the spectrometer itself will be discussed next. The schematic of a typical NMR spectrometer is shown in Figure 1.3. The magnetic field strength is one of the most important key performance indicators for a conventional NMR spectrometer. It affects the signal strength (from Boltzmann's distribution in equation 11) and spectral resolution (chemical shifts are further apart with higher B_0, allowing for detailed examination of the spectrum). It is usually characterised by the proton Larmor frequency at the centre of the magnet where the sample is expected to be placed. For example, a 400 MHz spectrometer means a 9.4 T magnetic field at the sensing volume.

Low field portable spectrometers usually use rare earth magnets. [31]

This scale of magnetic field strength is usually achieved using superconducting magnets, which require liquid Nitrogen and Helium to get below the critical temperature [68]. The NMR magnetic field record at the time of writing is 1.2 GHz [18], and some of the spectrometers cannot maintain continuous operation at the GHz field due to overheating of the coils.

Besides the strength of the magnetic field, the temporal stability and spatial uniformity of the magnet are also critical. Due to the imperfections in the static magnet, the field it generates will drift over time (roughly a few Hz per hour), so the Larmor frequency is also affected. The main source of the drift is the change in resistivity of the magnet coils due to temperature variations. If untreated, this leads to an increase in spectral linewidth and information such as J-couplings is buried under the widened peaks. To counter this effect, NMR spectrometers have a "locking" mechanism that monitors the resonance peaks and adjusts the measured spectra in postprocessing, so the subsequent measurements are adjusted so that no spectral broadening occurs from the drift [68].

Besides drifts in time, spatial inhomogeneity of the magnets over the sensing volume is also critical to NMR operations, as an inhomogeneous field can also distort the spectral linewidth. To optimise the field uniformity, a "shimming" mechanism is used. This is achieved by using a set of coils that generate weak static magnetic fields to compensate for the inhomogeneous main magnetic field [68]. Shimming is usually an automated procedure, which aims to maximise the NMR signal after locking by varying the currents in the shim coils. Shimming is performed after locking is achieved.

Locking and shimming are best performed using a chemical with a sharp NMR line, such as chloroform and chemicals with long T_1 relaxation times should be avoided, because they react more slowly to changes in magnetic fields and will lengthen the shimming process [68].

The RF coils in NMR spectrometers have dual purposes, delivering and receiving the RF signals. Due to the complex NMR pulses used in modern-day operations, transmitters and receivers are generally separated. In NMR spectroscopy, single-coil probe designs are usually used and can be finely tuned at different receiving and transmitting frequencies by varying the capacitance in a bridge circuit. When measuring a different isotope, a new probe is required, and when doing 2D heteronuclear NMR experiments such as HSQC, a second set of coils is needed [68]. In MRI, more complex coil designs can be found, such as parallel phase arrays [66]. MRI coils are also capable of generating circularly polarised RF fields [66].

Phased array receivers can also be found in military radars.

1.3 CURRENT LIMITATIONS OF NMR

The previous section has outlined some of the key working principles of NMR spectroscopy and its wide breadth of applicable scenarios from small molecules to large biological complexes. In addition to its versatility and low invasiveness, the high chemical selectivity provides detailed molecular structure information. However, despite these successes, the technique has a significant drawback in sensitivity. For a conventional NMR spectrometer, the typical lowest detection limit requires the active spin concentration to be around sub-mM (or sub-mg of purified compound) [68]. For isotopes with lower gyromagnetic

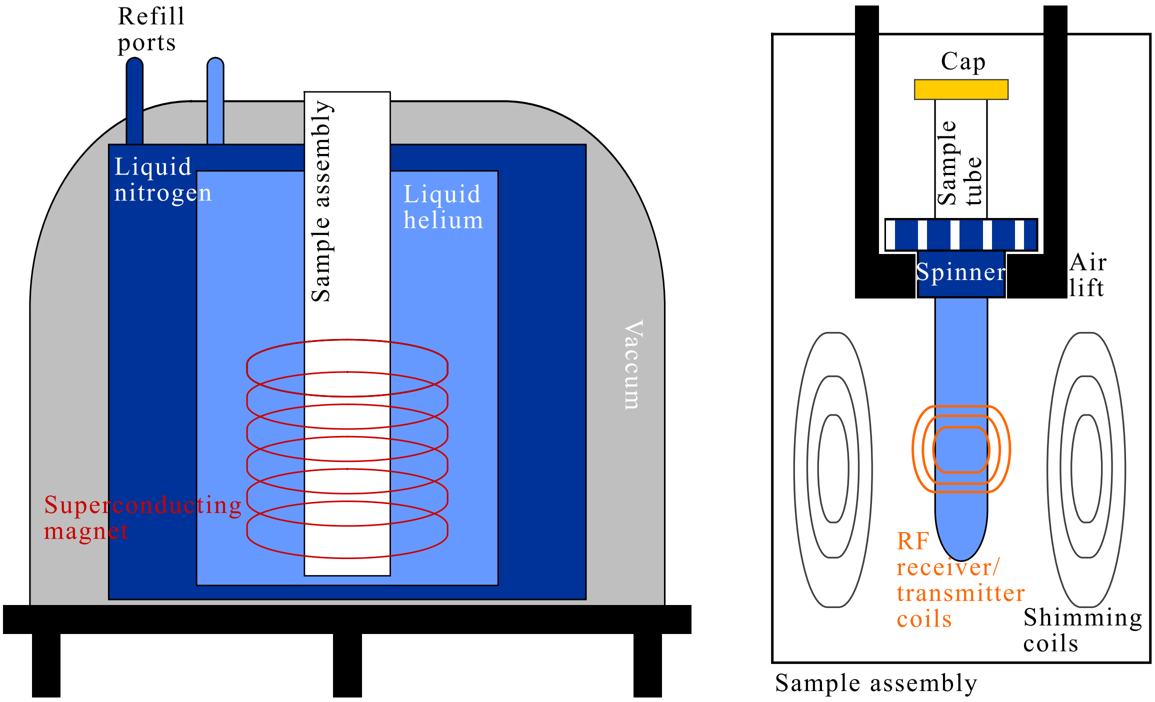

Figure 1.3: Schematic of an NMR spectrometer. **Left** shows the main magnetic component. A cryogenic superconducting magnet is positioned at the centre of the spectrometer surrounding the sample assembly. Usually, liquid helium and nitrogen are used to maintain superconductivity, and an extra layer of vacuum is in place to insulate the magnet. The cryogens need to be refilled during servicing. **Right** shows a detailed schematic of the sample assembly. The analyte is placed in a sample tube, which is held by a spinner. The spinner is lifted using an air lift, which ensures that the sample is floating in the middle of the sensing volume. A set of shimming coils surrounds the sensing volume to maintain spatial uniformity of the magnetic field, and RF receiver and transmitter coils are placed perpendicular to the B_0 field, hence only transverse magnetisation M_{xy} is directly observed in NMR and not M_z. The spinner physically rotates the sample tube along the z-axis, usually at 20 rotations per second. This is performed to increase spectral resolution by mitigating poor shimming performance. Not all spectrometers support spinners, and during multidimensional measurements (for example, COSY), spinning should be stopped to avoid artificial sidebands. The sample tube (usually ∼7-8 inches long and 5 mm in outer diameter) is typically made from borosilicate glass, which does not contain NMR interfering metal complexes. Higher quality grade tubes (Class A glass) are used when measuring larger biomolecules or using higher field magnets to minimise artefacts.

ratios or natural abundance, the concentration requirement increases; for example, ^{13}C NMR spectroscopy typically requires mg of samples and hours of acquisition time. Thus, when the availability of the sample is limited (common in a synthesis experiment where the product yield is low) or the product is unstable or dynamic (photoactive or biological samples), the operator may not always obtain the desirable information. This section will discuss the factors influencing NMR sensitivity and pathways of improvement.

1.3.1 *Energy*

NMR is widely used, but when sensitivity becomes an issue, operators tend to seek alternative techniques to complement the limited NMR information. In photochemistry or radical chemistry, the lifetime of targets of interests are typically significantly lower than the NMR acquisition time or in single molecule biology, where individual biological samples are studied instead of the collective effect; complementary techniques with lower chemical specificity or higher sample invasiveness, such as ultrafast lasers, electron-microscopy (EM) and X-ray crystallography (XRD), are available. These methods can probe the behaviour at the nanoscale or fs time scale due to the higher energy photon used. Induction coil NMR typically probe RF photons with relatively lower energy and higher wavelength (m scale), thus rendering it difficult to reach microscale sensitivity, which is an inherent hurdle to the induction coil NMR spectrometers.

A direct method of addressing this low-energy issue is to utilise an upconverted photon source that can be modulated by

NMR effects. On the extreme end, RDNMR uses beta decays from radioactive elements in a beamline such as the Isotope Mass Separator On-Line facility (ISOLDE) at CERN to probe NMR effects [36]. Because the oscillating NMR field can interact with the radioactive element and alter the direction of the beta ray, which is 10 orders of magnitude more energetic than RF photons. However, the obvious challenge is the size, weight and power (SWaP) and cost requirements. Also, typically, the RDNMR experiments require the NMR sample to be prepolarised in order to impact the radioactive species and can cause damage or alter its properties (see next subsection).

Visible photons can also be used to report NMR effects. The nuclear spin induced optical rotation (NSOR) experiment has demonstrated that nuclear spins can affect the polarisation direction of a laser and can be used to study the bond angle of molecules [138]. However, the interaction is relatively weak and sometimes requires prepolarised targets to detect the change. An alternative visible photon reporter is the NV centre in diamond, which will be discussed further in the following chapters.

1.3.2 *Thermal polarisation*

Another contributor to the sensitivity issue is the inherent low signal strength of the NMR spins due to the thermal Boltzmann polarisation detailed in the last section. There have been significant efforts in recent decades to alter the distribution of the spins and create a hyperpolarised target spin bath to achieve a signal boost and reduce measurement time or concentration requirement. The general strategy for hyperpolarisation is the use of external spins that can achieve beyond the Boltzmann distribution through methods such as chemical reaction and optical pumping by lasers or microwaves. These spins require a sufficient T_1 time to build up the polarisation and need to transfer the polarisation to the NMR targets, sometimes achieving a NMR sensitivity boost by 5 orders of magnitude.

Distortionless enhancement by polarisation transfer (DEPT) is a NMR technique that is usually used to distinguish between CH, CH_2 and CH_3 groups. Although it is not usually considered a hyperpolarisation tool, its working principle is based on polarisation transfer, and it can improve sensitivity.

Parahydrogen-induced polarisation (PHIP) is one of the methods. Parahydrogen is one of the spin states in the H_2 gas ($\frac{1}{\sqrt{2}} \left|\uparrow\downarrow\right\rangle - \left|\downarrow\uparrow\right\rangle$), which can be generated in a chemical reaction at low temperature. It can be enriched from 25% at room temperature to 50% at liquid nitrogen temperature and more when colder [63]. Then the parahydrogen can be attached to a chemical compound through a hydrogenation reaction or signal amplification by reversible exchange (SABRE), which uses a metal catalyst for attachment [50]. PHIP is usually used in studying low-yielding organic molecules. Its major drawback is that the efficient polarisation transfer (4-5 orders of magnitude improvement) can only be achieved at very short interaction distances, normally through J-coupling. As a consequence, effective PHIP is achievable for a limited number of compounds whose chemical precursor can be incorporated with parahydrogen. Often, the use of PHIP requires the chemical reaction design to be centred around hydrogenation or be compatible with SABRE, which limits the scope of this technique, and it suffers from low scalability.

For longer range interactions, there exists of better candidates such as Nobel gases when performing gas phase collision mediated polarisation transfer, also known as spin exchange optical pumping (SEOP). SEOP is usually used to boost MRI contrast in lungs [83].

Electron spins can also be used for hyperpolarisation, which is known as dynamic nuclear polarisation (DNP). Because the gyromagnetic ratio of electrons is 628 times higher than that of a proton, which produces a higher polarisation that can be transferred. The electrons are usually in the form of a radical and can be radiated by resonance microwaves to achieve their own hyperpolarised state [158]. The polarisation transfer can be mediated through NOE in liquid or electron-nuclear spin-spin interaction in solids. Cross effects and thermal mixing can also lead to polarisation transfer [113].

DNP is, to an extent, combining aspects of NMR and electron spin resonance (ESR), thus it requires additional MW generators, which adds to the SWaP requirements. Hurdles that are unique to ESR also apply, such as the inability to use water as a solvent due to its high dielectric constant that hinders MW delivery. Radicals are also highly reactive, which can alter the target of interest, for example, reacting with biomolecules or altering the structures of proteins. They can be short-lived due to their poor stability (minutes), thus diluting their benefits when doing long NMR scans, such as carbon or 2D experiments. Due to its paramagnetic nature, high concentrations of radicals can also lead to an increased rate of nuclear spin lattice relaxations, which broadens the spectral linewidth.

However, despite these challenges in liquid state DNP, most hurdles do not apply in ssNMR, which suffers more from sensitivity issues such as the presence of an oscillating background field from the MAS, thus time varying Boltzmann distribution and the broadened NMR peaks. So, DNP enhancements are more popular in studying the solid state materials where electron-nuclear pairs are more common and cryogenic temperatures that can reduce spin relaxation rates can be applied [113].

Hyperpolarisation techniques can boost the low NMR signal and achieve higher sensitivity. However, due to the fact that it can interfere with experimental design (PHIP) and the analyte itself (liquid state DNP), their scope of use is reduced to limited scenarios, so the use of hyperpolarisation tools can be contradictory to the NMR advantage of high versatility and low invasiveness.

1.3.3 *Electronics and other factors*

The SNR of an induction coil NMR spectrometer is given by $\mathrm{SNR}_{\mathrm{NMR}} \propto \mathrm{SNR}_{\mathrm{target}} \cdot \mathrm{SNR}_{\mathrm{instr}}$, where $\mathrm{SNR}_{\mathrm{target}}$ is the SNR contribution from the sample and $\mathrm{SNR}_{\mathrm{instr}}$ is from the instruments and they are given by [75, 77]

$$
\begin{aligned}
\mathrm{SNR}_{\mathrm{target}} &\propto N_t T_t^{-1/2} \gamma^{11/4} V_t I(I+1) && (22) \\
\mathrm{SNR}_{\mathrm{instr}} &\propto K B_{1ind,xy} B_0^{7/4} \eta_{fill} \left(\frac{Q_c V_c}{F_{preamp} T_c \Delta f R_c}\right)^{1/2}. && (23)
\end{aligned}
$$

The factors from the above equations are listed as follows,

- N_t, number of target spins contributing to the FID signal **per unit volume**;
- T_t, average temperature of the target;
- B_0, magnetic field strength experienced by the spins;
- γ, gyromagnetic ratio of the spins
- I, spin number of the target;

- K, a factor that describes the shape of the detection coil and its effectiveness in picking up current from the NMR signals uniformly;
- $B_{1ind,xy}$, the field induced in the pick up coils;
- η_{fill}, the filling factor of the coil;
- Q_c, quality factor of the coil;
- V_c, total volume enclosed by the coil;
- F_{preamp}, noise of the preamplifier;
- T_c, temperature of the coil;
- Δf, bandwidth of the detector;
- R_c, resistance of the coil.

The sensitivity thus can be defined by dividing the square root of the total acquisition time by the SNR. In this thesis, sensitivity is defined as the lowest detection limit; a smaller number means more sensitivity.

From equation 22, ^{13}C compared to ^{1}H NMR under similar conditions is three orders of magnitude less sensitive due to its lower natural abundance and gyromagnetic ratio.

Equations 22 and 23 encapsulate some of the key points discussed in this chapter. The SNR naturally will increase with higher natural abundance (or number of spins N_t), at lower temperatures T_t, higher magnetic fields B_0, higher spin numbers I and higher gyromagnetic ratio γ. It is worth noting that the power dependencies of B_0 and γ are sometimes reported differently, but are usually between 1.5 to 2 and 2.5 to 3, respectively [93]. This is due to different analysis methods when considering the noise levels in the instruments. When electrical induction noise is not considered, the upper bound of the power dependency applies.

This subsection will briefly discuss the other aspects of NMR operation that can limit its sensitivity. First, the electrical aspects will be considered. The primary source of noise in conductors stems from the random motion of the electrons, and it is dependent on the temperature; this is known as the Thermal Johnson noise. This is featured in equation 23 as $(T_c \Delta f R_c)^{1/2}$. In NMR coil design, this noise can be minimised by lowering the local temperature of the coils by using cryoprobes. The material used for the conductor can also be improved in order to reduce resistance. Uniformity (K), quality factors of the coil (Q) and the noise profile of the preamplifier (F_{preamp}) can also impact. For more detailed discussions, see reference [75].

The size of the coils also impacts the sensitivity by increasing $B_{1ind,xy}$, which is proportional to the diameter of the coil squared. There have been recent developments of microscale pickup coils that have enabled nanolitre scale NMR, which has the promise of integration with flow chemistry and single cell biology, thus offering gains in spatial sensitivity [4, 64]. However, by reducing scale, concentration sensitivity or the lowest detection limit is negatively affected by the reduction in V_c and V_t, and concentration-limited samples may not benefit from microcoils. On the other hand, for mass-limited samples, nanolitre solvent use allows for a boost in SNR by an increase in N_t.

Another method of increasing N_t is the use of susceptibility plugs [39], which can boost sensitivity by a factor of three. Sharp changes in magnetic susceptibility can adversely affect NMR performance. The NMR tubes are filled to a length that is 3 times higher than the length of the coils to divert the solvent-air interface further away. This creates a less efficient region of analyte that is not being detected effectively and reduces its concentration. The plugs create a solid medium with similar susceptibility that fills up this space and boosts sensitivity through concentration.

Over the past 50 years, there have been significant developments in addressing the NMR's hallmark weakness, sensitivity. Key inventions such as superconducting magnets, cyroprobes and DNP have surfaced to tackle some of the limitations discussed in this section. Owing to these efforts, the current minimum number of molecules required in an induction coil spectrometer is reduced to the nmol range [52]. However, it is still 14 orders of magnitude away from a single molecule. This thesis will discuss an alternative approach to induction coil NMR spectroscopy that uses quantum sensors with the potential for better sensitivity.

2

INTRODUCTION TO THE NV CENTRE IN DIAMOND

The NV centre boasts numerous advantages that can be translated to NMR spectroscopy. It offers sensitivity boosts through the reduction of interaction distance and sensing volume. It reports NMR signals as visible photons, which has smaller wavelength compared to RF and allow for microscopy-based imaging. The noise profile is also altered from the temperature-dependent thermal electric noise to the intensity-dependent photon shot noise. This chapter will introduce the working principle of the NV centre and its current progress in NMR experiments.

2.1 THE STRUCTURE OF THE NV CENTRE

The NV centre is an atomic substitutional defect in the diamond lattice, where two adjacent Carbon atoms are replaced by a Nitrogen and a vacant lattice site [38, 42] as illustrated in figure 2.1. The vector joining the Nitrogen and the vacancy site is defined to be the NV axis, and it can be aligned along any one of the four tetrahedral orientations in the diamond lattice. The diamond also has different crystallographic orientations, which are commonly referred to as the <111>, <100> and <110> diamond, which is when one of the NV axes is pointing towards the surface, the edge and the side of the diamond rectangular cuboid, respectively.

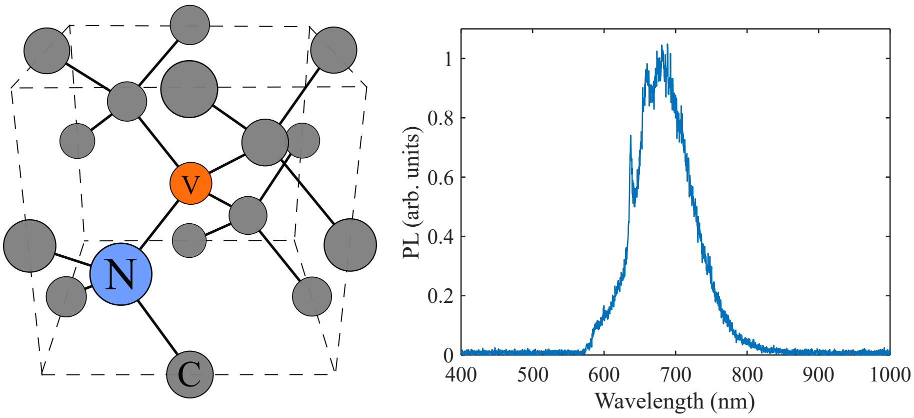

Figure 2.1: **Left** shows an illustration of the atomic structure of the NV centre. **Right** is an example of NV emission spectrum excited at 532 nm. The NV PL wavelength is around 630 - 800 nm and the zero phonon line is at 637 nm.

In its neutral charge state, the NV hosts three electrons from the dangling bonds to the neighbouring Carbon and a lone pair of electrons from the Nitrogen. When it captures an additional electron, the singly negatively charged state exhibits an electronic spin-1 system [43]. Unless otherwise stated, in this thesis, the NV centre refers to the -1 charged state. The significance of this charge state is that at its excited state, usually accessed by illumination of a 532 nm laser, the dominant relaxation pathway is dependent on the spin state. The $m_s = \pm 1$ states have a probability of relaxing non-radiatively, and $m_s = 0$ state is more likely to emit a red photon [108]. An example of the emission spectrum is shown in figure 2.1. This spin-state-dependent PL emission is a cornerstone of NV sensing, which is usually achieved by exposing the spin to external influences and measuring the PL. The PL difference between the spin states is known as the contrast. The readout process is generally achieved by illuminating the diamond with a green laser of µs duration. To obtain the maximum PL contrast, the total PL counts are usually integrated within the first few hundred ns of the laser pulse. When the laser pulse duration is longer (ms scale), there is a photon pumping mechanism that the spin state distribution will converge to the $m_s = 0$ state. This is known as a polarisation pulse and can be applied at the start of each experiment. A detailed discussion of the NV photophysics can be found at subsection 3.2.2. In this thesis, $m_s = +1$ states are not accessed, thus the NV spin can be treated as a two-level system between the $m_s = 0$ and -1 states.

The NV defect can be found in natural diamonds, but in most applications, the defects are synthesised due to the need for a more controlled spin environment. Chemical vapour deposition (CVD) is commonly used to fabricate the diamond host material. CVD uses methane and hydrogen gas heated at around 1000°C and under RF to generate radicals in a plasma and form additional carbon-carbon bonds to a seed crystal, which is usually another polished diamond substrate [102]. Then, to generate additional nitrogen and/or vacancy sites, ion implantation, electron irradiation or gas doping during the CVD process can be used [102, 132, 177]. By annealing the diamond at approximately 1000°C, the vacancies are then mobile and can be captured by a nitrogen to form the NV centre [78, 119]. The surface of the diamond can then be acid-treated to finish the process. To characterise the sample, spectroscopic (visible and/or infrared) techniques are commonly used [102]. In the context of this thesis, impurities generating unwanted NMR signals or affecting NV stability are to be avoided, for example, surface spin and charge when using shallow NVs (nm deep) [116]. And for measurements that are sensitive to the NV intrinsic coherence time, for example, dynamical decoupling (see next section), spin noise from substitutional nitrogen can also affect quantum decoherence and NMR performance [15].

2.2 DYNAMIC PROCESSES OF THE NV SPIN

To facilitate NV NMR spectroscopy, certain quantum sensing protocols are required prior to. Most of the NV protocols in this thesis revolve around the concept of magnetic resonance, and thus, they share certain similarities with the techniques that are used in conventional ESR or NMR, which are discussed in the previous chapter. The major difference is in the final part of the pulse sequence. For induction coil NMR, the transverse magnetisation (M_{xy}) is directly measured by the coils that are perpendicular to the NMR static magnetic field, but longitudinal components (M_z) cannot be directly detected. This implies that at the end of the pulse sequence, the magnetisation vector needs to be projected back to the xy plane. As a consequence, protocols that measure M_{xy}, such as FID, are more convenient than M_z. For example, in practice, in an induction NMR experiment, when measuring T_1, which is in the longitudinal direction, the inversion recovery protocol needs a final 90^o pulse that reprojects the vector to the xy plane for readout. On the other hand, for NV optical readouts, the spin state-dependent PL is a measure of spin population difference between the $m_s = 0$ and $m_s = \pm 1$ states, which is in the longitudinal direction. Thus, NV T_2 measurements, which are in the transverse direction, need a reprojection back to the longitudinal direction and NV T_1 protocols are more convenient. To summarise, when inspecting sequences between the two scenarios, optical NV T_2 or induction

NMR T_1 measurements usually have an extra 90° pulse towards the end compared to their counterparts.

The first step in NV NMR is to determine the resonance frequency of the NV centre by performing ESR via the PL readout method, commonly referred to as the optically detected magnetic resonance (ODMR) [124].

Conventional ESR can also be used, but ODMR provide extra SNR due to the use of optical polarisation.

The resonance conditions are dictated by the NV spin Hamiltonian, given by [42]

$$H_{NV} = D(T)\hat{S}^2_{NV_z} + \gamma_e \mathbf{B} \cdot \hat{\mathbf{S}}_{\mathbf{NV}} + \hat{\mathbf{S}}_{\mathbf{NV}} \cdot \mathbf{A} \cdot \hat{\mathbf{I}}_{\mathbf{N}} + H_{other}, \quad (24)$$

where $D(T) = 2.88\,\text{GHz}$ is the temperature dependent zero-field splitting at the ground state, $\hat{S}_{NV_i} = \frac{\hbar}{\sqrt{2}}\sigma_i$ are the NV spin vectors, $\gamma_{NV} = 28.025\,\text{GHz}/\text{T}$ is the NV electronic gyromagnetic ratio, $\mathbf{B}$ is the external magnetic field, $\hat{\mathbf{I}}_{\mathbf{N}}$ is the spin vector of the parent Nitrogen, $\mathbf{A}$ is the hyperfine interaction tensor and H_{other} represents other terms such as electric field effects. From the Hamiltonian, the relevant interactions measurable in a magnetic resonance experiment can be deduced. To perform an ODMR measurement, a green laser is used for NV polarisation and readout and a variable frequency microwave (MW) source is swept while the PL is being monitored. When a resonance condition is met, a reduction in contrast can be observed, shown in figure 2.2. The laser and MW can be applied at the same time, referred to as CW ODMR or separated, referred to as pulsed ODMR [121]. Pulsed ODMR offers the advantage of a more controlled and efficient manipulation of optical and spin states, which offers an increase in spectral resolution at the expense of timing control equipment. The linewidth of pulsed ODMR is the inverse of the T_2^* time, which is influenced by MW and magnetic field gradients, interactions with other spins such as ^{13}C and substitutional Nitrogen, lattice strains and more.

Because the resonance condition can report external magnetic field strength, NV is often used as a magnetometer. For NMR, the signal of interest can also be treated as an oscillating magnetic field $\mathbf{B}(t)$ at the Larmor frequency of hundreds of MHz, but ODMR is considered to be relatively slow measurement due to the timing overheads needed for laser and MW delivery and does not have the bandwidth to access the MHz range, thus other dynamic techniques are needed and ODMR serves as a preliminary measurement to determine the resonance frequency for $m_s = 0$ to $m_s = \pm 1$ transitions (ω_{NV}).

This bandwidth argument is similar to the CW vs FT NMR comparison in the last chapter.

Equipped with ω_{NV}, the next step required for the NV NMR experiment is to measure the duration of MW application needed to transfer populations between the spin states, which is known as a Rabi experiment [80]. To perform this measurement, on resonance MW will be applied to the polarised NV state and its duration is varied as shown in figure 2.3. By inspecting contrast vs MW duration, a sinusoidal population and depopulation of the spin states can be observed, and by inspecting the time taken between maximum and minimum contrast, the π pulse (and thus $\pi/2$) duration can be obtained. This is analogous to the NMR 180^{o} pulse. $T_{1\rho}$ is the decay time observed in the Rabi oscillation,s and it is usually influenced by magnetic noise near the Rabi frequency and external field inhomogeneities.

The NVs can now be manipulated to the superposition state by a $\pi/2$ pulse. In conventional NMR spectroscopy, at the superposition state, Larmor precession is measured. However, for NV sensing, the relative phase Larmor precession acts as a reporting mechanism to external influences. By applying dynamic de-

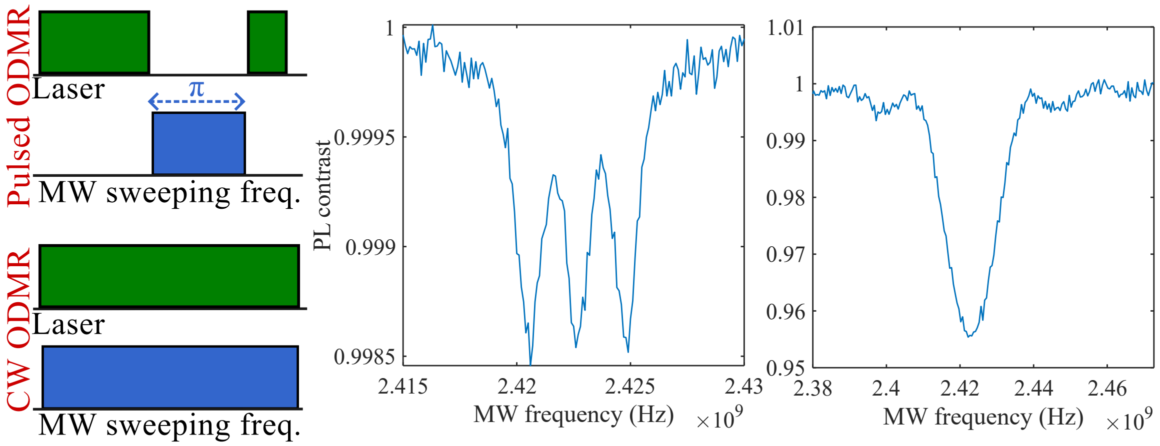

Figure 2.2: **Left** shows the pulse sequence used for ODMR measurements using pulsed (Top) and CW (Bottom) sources. To achieve ideal ODMR linewidth and contrast, pulsed ODMR should be employed. A ms polarisation laser initialises the NVs to the $m_s = 0$ state, then a MW π pulse (from a Rabi experiment) with variable frequency is applied, and a μs readout laser is used. **Centre** is an example of pulsed ODMR spectrum measured at an aligned background magnetic field of $B_0 = 16\,\text{mT}$. When the resonance condition from $m_s = 0$ to -1 state is met, a reduction of PL contrast is observed. The three peaks are due to the hyperfine interaction with the parent ^{14}N. The transition to the +1 spin state is expected at $D(T) + B_0\gamma_{NV} = 3.3\,\text{GHz}$. **Right** is an example of CW ODMR at higher laser and MW power. This introduces linebroadening, and the hyperfine interactions are no longer resolvable, but at higher powers, there are more transitions towards the $m_s = -1$ state, thus a higher PL contrast is observed. Multiple lattice orientations of NVs family can create up to 4 sets of peaks. PL contrast can increase when 2 or more families of NV orientations experience the same magnetic field strength (overlap), a preferentially aligned NV sample is used and when the excitation laser polarisation is aligned to a NV axis. The full-width-half-maximum (FWHM) of the individual peaks can be used to determine the observed decoherence time, T_2^*.

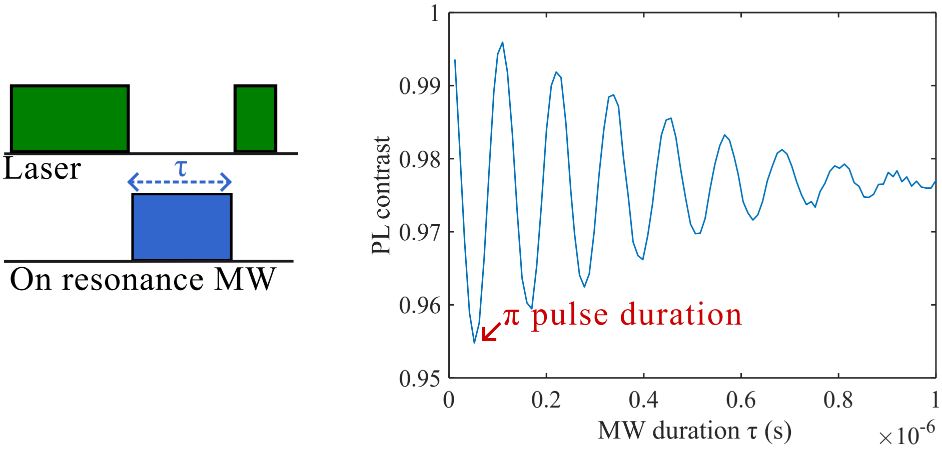

Figure 2.3: **Left** is the pulse sequence used for a Rabi experiment. An on-resonance MW with varying duration is applied, and it transfers population between the $m_s = 0$ and ± 1 states. Such a transfer causes an oscillation in PL behaviour as shown in **Right** and the π can be obtained. During the Rabi experiment, spin relaxations occur and can cause a reduction in the averaged PL over time. The time of reduction is known as the spin lock time ($T_{1\rho}$) and can be characterised by the first-order exponential decay time constant in the oscillation envelope. The mechanism of $T_{1\rho}$ is similar to T_1, but it is more sensitive to energy transfer near the Rabi frequency (dressed state resonance) instead of the (bare state) resonance frequency. Field inhomogeneities can also lead to an additional contribution to the observed $T_{1\rho}$.

coupling (DD) sequences to the superposition, such as Hahn-echo [80] or XY8-N pulse sequences [91], decoherence time T_2 can be measured as shown in figure 2.4. T_2 can be influenced by the environment; NVs experiencing a higher level of spin noise (for example, a diamond with more other defects such as substitutional Nitrogen) will exhibit a shorter intrinsic T_2 time. This can also be used as a spectroscopic tool to deduce the source of influence (more details in the next section). NMR signals are within the RF band of the electromagnetic spectrum, and the DD protocols introduced so far are suitable for the scope of this thesis. Nonetheless, there exists a wide range of NV sensing protocols that are not discussed in this thesis and serve different applications, such as sensing GHz signals from ESR using relaxometry protocols [25].

2.3 INTRODUCTION OF NMR SPECTROSCOPY USING NVS

The decoherence mechanism is a key process in performing NV-based NMR spectroscopy. The previous section outlined the procedures needed to perform a T_2 measurement; this section will explain the spectroscopic filtering needed to perform NMR on targets of interest. The NV phase shift can be expressed as [71]

$$\Phi = \gamma_e \int_0^{\tau_{tot}} B(t)\mathcal{F}\{g(f_{DD})\}\,dt, \tag{25}$$

where $\mathcal{F}\{g(f_{DD})$ is an FT of a filter function $g(f_{DD})$ that depends on the pulse sequence used, and τ_{tot} is the total time that NV is exposed to external noise during the experiment.

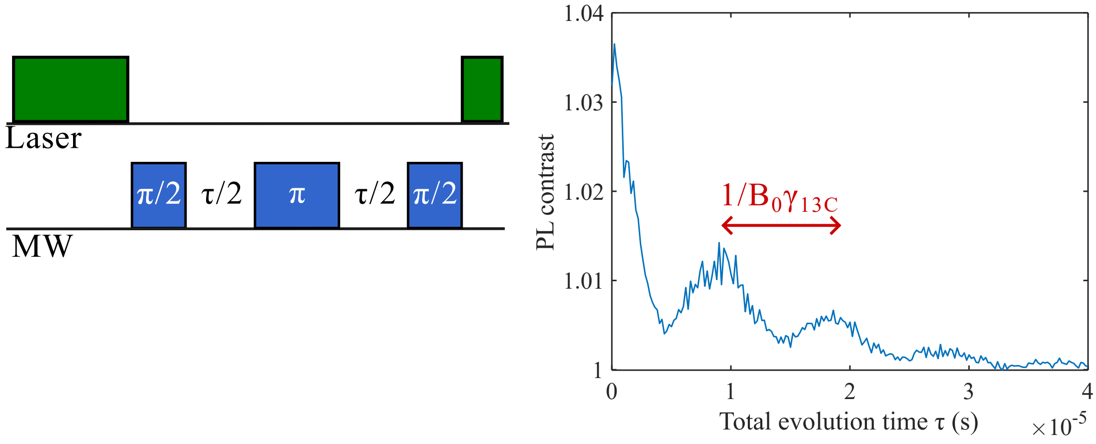

Figure 2.4: **Left** is the Hahn-echo DD pulse sequence, similar to the NMR Hahn-echo sequence discussed in the previous chapter, with the exception of an addition $\pi/2$ pulse at the echo for readout projection purposes. **Right** is an example Hahn-echo measurement. As spin dephasing occurs, the observed magnitude of the NV spin vector reduces and hence the PL too. The spin decoherence time (T_2) can be obtained by the first-order exponential decay time constant in the oscillation envelope. The oscillations in this measurement are caused by the coupling to nearby ^{13}C spins, and the rate of oscillation is their Larmor frequency.

Recall that in conventional NMR, Hahn-echo sequences provide a refocusing mechanism to the magnetisation vector and provide additional signals in the form of echos thus extending measured T_2 and improving spectral linewidth. In frequency space, echo trains act as a filter; by flipping the vector at a certain frequency, noise outside the filtering range will be suppressed, thus extending T_2. The effectiveness of the filtering can also be extended by applying additional DD pulses (for example, CPMG trains). Mathematically, this is a reduction of the filter function ($g(f_{DD})$) linewidth and, as a result, a further reduction of exposed noise and longer T_2. The spectral position of the filter function f_{DD} can also be altered by adjusting the rate of application of DD pulses (or interpulse spacing). This is the linchpin in NV NMR spectroscopy, by varying f_{DD}, the magnetic frequency space can be swept, and when f_{DD} is on resonance with a distinctive noise at a certain frequency, for example, NMR Larmor precession of a target of interest, an additional decoherence rate can be observed. Thus, by examining the NV contrast with respect to the interpulse space of a DD protocol, an NMR spectrum can be obtained as exemplified in figure 2.5. This is referred to as decoherence-based NV NMR spectroscopy, and it is largely applied in part II of this thesis. In part III, an additional modulation to this protocol, known as quantum heterodyne, is discussed.

It may seem that this is a roundabout way of performing NMR spectroscopy by applying electron magnetic resonance to detect nuclear spins instead of directly measuring the NMR signals from coils. However, the NV centre has demonstrated nanoscale sensitivity, which the induction NMR spectrometer lacks, while maintaining a reasonable SWaP requirement.

There is an upper limit to f_{DD} caused by the finite duration of the π pulses (tens of ns), thus these protocols are more suited to examine MHz signals than GHz and higher.

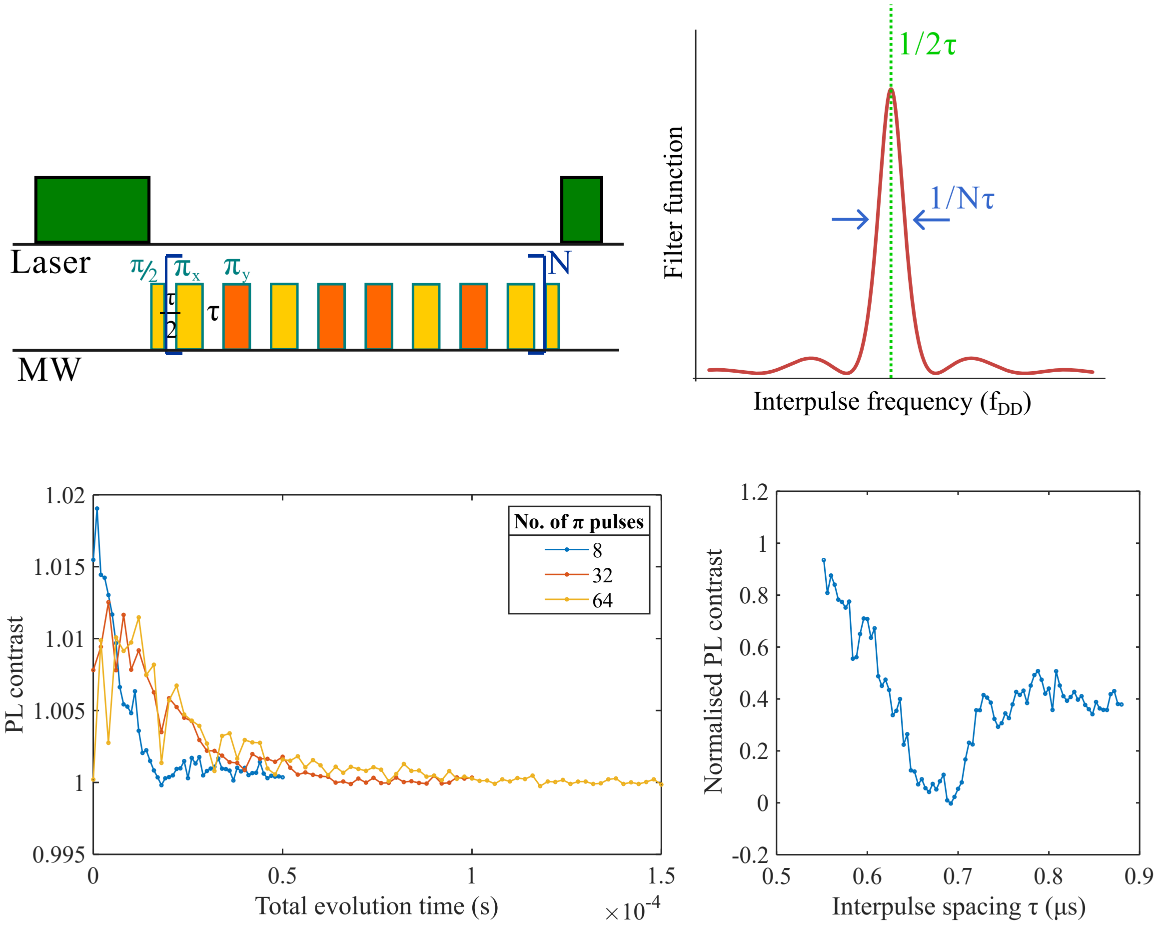

Figure 2.5: **Top Left** shows the pulse sequence used for a XY8-N DD experiment. First, a $\pi/2$ pulse is applied to transfer the NV spin to the superposition state. Then a series of π pulses with alternating MW phases are applied up to integer multiples (N) of 8, with the pattern of $(x\text{-}y\text{-}x\text{-}y\text{-}y\text{-}x\text{-}y\text{-}x)^N$ is applied, and readout pulses are used after. One of the advantages of using alternating phases is its ability to correct for any pulse errors [51] that can come from MW inhomogeneities or electronic timing resolution constraints. **Bottom Left** shows examples of XY8-N decays with 8, 32 and 64 π pulses. As N increases, the observed decoherence slows due to the narrowing of the filter function and therefore the reduction of external influences. However, the initial contrast of the NV reduces as higher N needs a longer duration of MW exposure and spin lock relaxation increases. **Top Right** is an illustration of the XY8-N filter function. Its width can be reduced by increasing N and thus extending coherence. Its spectral position is dependent on the interpulse spacing (τ). When sweeping the filter frequency by changing τ, spectroscopy can be performed as shown in **Bottom Right**, which exemplifies a ^{13}C NV NMR spectrum at 65 mT.

The sensitivity gain stems from a range of factors. Compared to the size of induction coils that is limited by fabrication constraints, the NV centre, due to its intrinsic atomic size, can be placed nm away from the target of interest at the diamond surface, which is chemically inert and stable. This reduction in distance increases interaction strength and the NMR signal. Also, the NV reports the magnetic environment by emitting visible photons that are six orders of magnitude more energetic. This allows for optical-based detection methods, which are shot noise-limited. The shot noise is dependent on the square root of the number of photons, which is easier to scale compared to the reduction in temperature for the induction coils. In addition, the visible photons can also be used in microscopy. Compared to conventional MRI, which requires the spatial scanning of induction coils and gradient fields, which are difficult to construct at the sub-micro scale, the NV microscope can offer MRI capabilities at the optical diffraction limit.

The significant downside of NV-based NMR is the optical interference from the laser and PL. The target of interest should be unaltered by green illumination and should not emit a significant amount of overlapping photons, which reduces the NV PL contrast. This can place exclusions in studying photoactive materials such as fluorescent dyes, quantum dots and photocatalysts. Other limitations in NV NMR are discussed throughout the rest of the thesis.

A number of NV NMR achievements have been reported in the literature so far. In 2013, Staudacher et al. and Mamin et al. reported the detection of NMR signals use near surface single NV centres 5 and 20 nm away from the surface [106, 152]. Both demonstrations have achieved nanoscale spatial sensitivity, which is a significant improvement over the microscale-limited induction-based NMR spectroscopy. Then Lovchinssky et al. [100] demonstrated the capability of resolving NMR spectroscopy originating from a single protein, and Muller et al. [115] reported spatial information in NMR spectroscopy at the nanoscale, thus a pathway to MRI. However, there are potential pitfalls with nanoscale NMR experiments. The spatial resolution is dependent on the NV target distance, which incentivises the NV to be as close to the surface as possible. However, due to material constraints, shallow NVs suffer from low coherence time, poor photostability and are hard to produce at deterministic atomic sites [65, 84, 116]. In addition, nanoscale targets require immobilisation techniques to avoid information loss due to rapid diffusion away from the sensing volume [3, 45]. As a consequence, sub-nm resolution or single small-molecule NV NMR have yet to be achieved, and these demonstrations all used targets that are either solid state or immobilised. Part II of this thesis will explore potential methods to improve NV performance at the nano and sub-micro scale.

Despite the gains in spatial sensitivity, nanoscale NV NMR also suffers from poor spectral resolution, which can be affected by target diffusion broadening and low coherence time (see more in subsection 4.4). So far, the usual nanoNMR linewidth is limited to kHz, which is capable of distinguishing different elements [40], but not enough to resolve key molecular structure information such as J-coupling and chemical shifts. Correlation or heterodyne approaches have been used to boost spectral resolution. Aslam et al. [7] reported NV NMR resolution of 200 Hz. This is achieved by bypassing the NV coherence time limit through the use of the longer Nitrogen nuclear spin memory and correlation approaches. At 3 T, such resolution is capable of resolving chemical shifts. The diffusion limitation is mitigated by using viscous Fluorine targets in a larger sensing volume (NV depth 50 nm). The spectral resolution can then be further improved by using heterodyne approaches. Glenn et al. [60] have also demonstrated mHz of linewidth and J-coupling resolved NMR spectra on molecules with similar viscosity to water. However, the demonstrations were conducted on a large ensemble of molecules, which exhibits statistical polarisation and requires µm deep NV ensembles, significantly reducing the sensitivity (see more in subsection 5.4). Thus, presently, there is usually a trade-off in natural liquid state NV NMR between spatial sensitivity and spectral linewidth. Part III of this thesis will explore similar protocols that offer high spectral resolution and discuss key performance-related factors when applying these microscale experiments to microfluidic-based flow chemistry applications.

In the face of these challenges, NV is still a promising alternative NMR platform to induction coils. It is still a relatively new field; the room for improvements and key gaps have been identified, thus, arguably, the potential for NV sensors is not fully realised yet. Also, NV sensors can offer alternative approaches to the current NMR applications, such as NMR under extreme conditions [16], NMR in conjunction with atomic force microscopy (AFM) [105], ZULF NMR [28] and more. The final part of this thesis will briefly explore two future pathways in NV NMR, ZULF NMR and the combination of high spectral and spatial resolution NMR.

Part II

NV NMR AT THE NANOSCALE

This part of the thesis aims to tackle problems in the nanoscale NV NMR experiments. In Chapter 3, I present a postprocessing technique that can be used to increase SNR. I'll detail the theory and the supporting experimental evidence. In the end, this technique can achieve a 36% gain in sensitivity by using additional computation resources and can be widely applied to NV protocols other than NMR. In Chapter 4, the work is extended to using an ensemble of NVs. I'll first attempt to adapt the postprocessing protocol to NV ensemble experiments and explain its limitations at this scale. The main problem is the low laser excitation rate experienced when an ensemble is used. The second portion of Chapter 4 will explore how optical noises impact NV wide-field experiments. I conducted a comparison study between two laser sources and investigated NMR performance. I then simulated the laser noise profile and showed that raw laser performance gains are not fully translatable to NV NMR. I'll conclude by discussing the linewidth limitations of NV NMR at this scale, which serves as a motivation for Part III of the thesis.

3

IMPROVING NANOSCALE NMR SPECTROSCOPY USING SINGLE NV VIA READOUT SIGNAL PROCESSING

Quantum sensors based on NV defects in diamond have a demonstrated capability to detect NMR spectra from proximate molecular nuclei, thereby promising an alternative with higher sensitivity to conventional NMR spectrometers for micro-scale samples. In previous chapters, the mechanism underpinning the NMR spectroscopy process using NV centres in diamond has been detailed. In this chapter, the development of a new protocol to enhance the NV-NMR performance will be explored. This protocol will focus on the readout workflow of the NV sensor, drawing insights from the underpinning photophysics of the PL emissions to extract key spin state information of the NV centre.

The fluorescence-based readout of these sensors suffers from low throughput and poor photostability, meaning there is still significant scope to maximise their sensitivity and temporal resolution. In this chapter, a new readout protocol based on parameter fitting to a precise model of the NV photo-physics is demonstrated. Whereas typical approaches to improvement involve expensive diamond material, optical and microwave engineering, this method can be readily implemented into existing NV quantum sensing protocols. The improvement is demonstrated on single NV experiments with an emphasis on nanoNMR, showing an increase in measurement speed by 36%.

3.1 INTRODUCTION

Understanding molecular structure is of critical importance to pharmaceutical design, material science, and biological engineering [59, 92, 126]. One of the most powerful tools for discerning molecular structure is NMR spectroscopy, which provides key information such as chemical shifts and J-couplings for samples ranging from small organic molecules to large biological complexes in a non-destructive manner [8]. However, minimum detection limits for conventional NMR restrict the sample volumes to mL and target analyte concentrations to micromolar ranges [14, 123]. These shortcomings render conventional NMR unsuitable for probing sub-micron samples or fast dynamics, which are common in photochemistry, catalysis, and single-molecule biology. This necessitates the use of alternative techniques such as mass spectrometry and cryo-electron microscopy, which are invasive to the sample or bioassays and ultrafast laser spectroscopy, which lacks versatility in types of samples that can be analysed [9, 34, 86, 147].

The restrictions in conventional NMR largely stem from the inductive pickup coils used for detection, which are challenging to fabricate at the micron scale, and suffer from electronic noise when detecting small numbers of spins [5]. An alternative detection scheme replaces the inductive coils with the use of atomic-sized quantum sensors, the most promising of which is the NV centre in diamond [3, 45, 127].

As detailed in the previous chapter, the NV centre exhibits several quantum sensing advantages, including a chemically-inert interface, stable host material, long quantum coherence times at room temperature, spin-state dependent PL, and relatively low size, weight and power requirements. It has thus attracted great interest in recent years in fields such as magnetometry, thermometry, chemical sensing, biological studies, and material science [42, 71, 87, 110, 160, 163]. Translation of these techniques to other fields, however, will require the optimisation of key-performance parameters such as sensitivity and measurement speed [10, 120].

Previous pioneering works have established the working principles of NV-based nanoNMR, and key achievements such as single protein sensing have been demonstrated [40, 96, 100, 106]. However, at this scale, there exists a trade-off between sensitivity and photo-stability due to fluctuations in NV charge states. The signals of interest are typically reported by a single NV centre, exhibiting poor sensing speed (due to the limited PL emission rates from the single emitter) and additional complexities with NV-target co-location, when compared with large NV ensembles. Measurement times scale with the standoff distance between the target and NV centre, motivating the engineering of the NV centres to within nanometers of the diamond surface [115, 152]. The proximity to the diamond surface results in both reduced spin coherence time due to nearby surface paramagnetic defects and charge instability due to variable electric fields near the surface [89, 134], rendering improvements to temporal resolution a significant challenge at these scales.

Typical approaches to enhancing sensitivity can involve material improvements to increase the spin coherence time, or tailored quantum control sequences to filter unwanted noise; both of which have demonstrated improvement [51, 73]. However, for nanoscale NMR, the material gains become limited by the surface spin noise and in the majority of cases, complex quantum control sequences reduce the sensing bandwidth [37, 58, 122]. This chapter explores an alternate approach to enhancing the nanoscale NMR sensitivity in the form of optical spin readout optimisation. This approach can be applied generally across all quantum sensing protocols to achieve a speed-up in measurement time.

The most common approach to determine the spin state population is to integrate the PL at the beginning of an optical readout pulse when the spin state contrast is maximum. Then this is self-referenced against a flat portion of the PL towards the end of the pulse for common noise rejection at the µs scale. Previous work has demonstrated spin readout improvements via maximum likelihood, Bayesian and spin-to-charge conversion techniques [69, 118, 146, 174, 175]. These approaches have led to signal-to-noise ratio (SNR) gain of up to 20% using maximum likelihood estimation [69, 118, 174] or 28.6% via Bayesian optimisation [175]. There is also an interest in converting information in the NV spin to NV charge states [146], or electrical spin readout [67], both of which can improve the SNR at the expense of additional equipment and reduced bandwidth.

This chapter proposes and demonstrates a technique that improves sensitivity and temporal resolution via a tailored signal-processing approach. This approach models the dependence of NV PL subject to experimental parameters associated with laser pulse amplitude and duration. The new results are then compared with the conventional NV readout approaches in a nanoNMR experiment.

3.2 METHODS

3.2.1 *Experimental setup*

To image and identify single NV centres in diamond, the NV fluorescence from a bulk single crystal diamond using a purpose-built inverted confocal microscope was used, as shown in figure 3.1. A green excitation 532nm laser (Laser Quantum Gem FS) is used to excite the NV defects, and a single-photon avalanche diode (SPAD, Excelitas SPCM-AQRH-12FC) is used to collect the filtered PL. The excitation beam is modulated by an AOM (AA Opto-Electronic MT200-A0.5-VIS), which is in turn controlled by a TTL signal originating from a programmable Pulse-Blaster (PB, SpinCore PBESR-PRO-500-PCIe). Although the laser power control is kept constant in current mode for stability, an adjustable neutral density filter is used to control the laser power for calibration. The green laser is then focused into a single-mode fibre (Thorlabs P1-460B-FC-1), collimated using a lens (Thorlabs ACL12708U, f = 8 mm) and then onto the diamond by an immersion oil objective (Nikon 60x, NA1.4). The same objective is then used to capture the red PL from the NV, and a dichroic bandpass filter is used to decouple the red PL from the green laser. The PL is passed through a band-pass filter (Semrock FF01-731/137) and focused into a multimode fibre (Thorlabs M42L01) by an achromatic lens (Thorlabs AC254-100-B-ML), which acts as a confocal pinhole. The fibre then delivers the PL into the SPAD, and the individual photons are counted, then time tagged by a Fast ComTech P7882 multiscaler time of flight counter. The PL data are time tagged at the resolution of 0.1 ns and binned to 0.8 ns. The data streaming process can also be controlled to store data in predefined timing intervals throughout the experiment.

A background magnetic field of 77 mT is applied to the sample to lift the degeneracy of the NV spin states and to polarise the nitrogen nuclear spin [30] associated with the single N-V centre. A piezo-electric stage (Physik Instrumente P-611.3 NanoCube) is used to move the sample stage in three directions, and it is controlled by a Data Acquisition System (National Instruments DAQ PCIe-6323).

To manipulate the NV spin state for the experiments, microwaves are generated by a vector signal generator (Rohde & Schwarz SMBV100A). The MW is delivered by a custom gold omega antenna, deposited onto a glass coverslip, where the diamond is placed on top and adhered using immersion oil. A MW amplifier (43 dB gain, Amplifier Research 20S1G4) is used to generate 0.3 W of MW power to the antenna.

The diamond substrate is an electronic grade ([N] $<$ 5 ppb) sample produced via chemical vapour deposition (Element Six). The sample was then subjected to electron irradiation at 10 MeV with a dose of 10^{14} cm^{-2} and annealed at 900°C in vacuum for two hours.

3.2.2 *Theoretical description*

A seven-state rate equation model (SSM) was used to evaluate the NV signal. The PL response is dictated by the spin-dependent relaxation through and cycling between the neutral and negative charge states, shown in Fig. 3.4. In the negative charge state, there exists a group of ground triplet states ($m_s = 0$, denoted state $|1\rangle$; and $m_s = \pm 1$, denoted state $|2\rangle$) and excited triplet states ($|3\rangle$ and $|4\rangle$) separated by 1.95 eV. In these experiments, a permanent static magnetic field is used to Zeeman split the triplet states and only the $m_s = 0$ ($|1\rangle$ and $|3\rangle$) and $m_s = -1$ ($|2\rangle$ and $|4\rangle$) states are considered. Excitation to $|3\rangle$ and $|4\rangle$ occurs at rate βk_r, which is proportional to the 532 nm excitation intensity, parameterised by β. From state $|3\rangle$ and $|4\rangle$, there are three possible transition pathways, with their own individual decay rates. These transitions (non-radiative decay via $|5\rangle$ or direct radiative decay) are the cause of the spin-state dependent PL and optical polarisation of $m_s = 0$, because the $|3\rangle$ state is more likely to relax in a spin-conserving manner back to the $|1\rangle$ states and $|4\rangle$ (relatively to $|3\rangle$) is more likely to relax via $|5\rangle$, where a spin-phonon interaction occurs and the spin state is flipped [157].

In the model, a photo-ionisation pathway to the neutral NV state ($|6\rangle$) is included with the rate given by βk_{ion}. In $|6\rangle$, there is an optical excitation in the charge state with the rate βk_{rc} to $|7\rangle$. The NV^0 excited state may relax radiatively (k_{rc}) or return to the NV$^-$ ground states (βk_{rec}) with no spin-dependency [169]. In these experiments, the NV^0 emission is optically filtered, and only a fraction ($\alpha = 0.3$) is collected.

These spin state dynamics can be modelled by using a set of rate equations [161], given by

$$\frac{d\mathbf{p}(t)}{dt} = \mathbf{A}(\beta, k_r, k_{35}, ...)\mathbf{p}(t = 0), \tag{26}$$

where $\mathbf{p}(t)$ is a column vector representing the populations of the seven states at time t, given by

$$\mathbf{p}(t) = \left(P_{|1\rangle}, \ldots, P_{|7\rangle}\right) \tag{27}$$

and

$$\mathbf{A} = \begin{bmatrix} -\beta k_r & 0 & k_r & 0 & k_{51} & 0 & \beta k_{rec}/3 \\ 0 & -\beta k_r & 0 & k_r & k_{52} & 0 & 2\beta k_{rec}/3 \\ \beta k_r & 0 & -k_r - k_{35} - \beta k_{ion} & 0 & 0 & 0 & 0 \\ 0 & \beta k_r & 0 & -k_r - k_{45} - \beta k_{ion} & 0 & 0 & 0 \\ 0 & 0 & k_{35} & k_{45} & -k_{51} - k_{52} & 0 & 0 \\ 0 & 0 & \beta k_{ion} & \beta k_{ion} & 0 & -\beta k_{rc} & k_{rc} \\ 0 & 0 & 0 & 0 & 0 & \beta k_{rc} & -k_{rc} - \beta k_{rec} \end{bmatrix} \tag{28}$$

is the matrix of rate coefficients defining the evolution of $\mathbf{p}(t)$, from which the evolution of the system may be determined via

$$\mathbf{p}(t) = \exp\big((t - t')\,\mathbf{A}\big)\mathbf{p}(t'). \tag{29}$$

In the SSM, β is defined to be a constant for $t > 0$, meaning that the laser is always switched on with a stable power for the duration t. Additionally, the assumption $P_{|3\rangle}(0)$, $P_{|4\rangle}(0)$, $P_{|5\rangle}(0)$ and $P_{|7\rangle}(0) = 0$ is employed, implying that before the laser is turned on, the populations are in the thermally populated ground states. $P_{|1\rangle}(0) \equiv 1 - P_{|2\rangle}(0)$ is defined for convenience. The exact rate constants used in $\mathbf{A}$ are available in the table 1.

The stable power assumption holds better in a setting where the PL is saturated compared to an unsaturated regime, usually in ensemble NV experiments. The next chapter will explore the laser fluctuation effects.

By solving the rate equations in equation 29, the populations of each individual state as a function of laser time can be determined, hence the time dependence of the PL of the NV centre can be deduced, which is given by

$$\mathrm{PL}(t) \propto P_{|3\rangle}(t)k_r + P_{|4\rangle}(t)k_r + \alpha P_{|7\rangle}(t)k_{rc} \tag{30}$$

Parameter	k_{35}	k_{45}	k_{51}	k_{52}	k_{ion}	k_{rec}	k_r	k_{rc}
Rate (MHz)	10	55	7	1.5	10	100	65	40

Table 1: A table listing the rate constants used in **A**.

and also shown in figure 3.4, where there is an excellent agreement between the modelled and measured PL for a single NV emitter.

In the SSM, **A** is assumed to be constant, implying that $PL(t)$ is only dependent on $\mathbf{p}(0)$. Calibration experiments are performed (see next subsection), and the measurements show $\beta = 0.7$ and $P_{|6\rangle}(0)$ to be 30% of the total initial population.

3.2.3 *Calibration of the SSM*

Rate parameters used

Table 1 outlines the rate constants used for the SSM, mostly based on Tetienne et al. [161]. It is noted that the charge state-related transition rates (k_{ion} and k_{rec}) are not well defined and can vary depending on the local charge environment [109]. Some of the parameters are experiment or sample-dependent; if the reader wishes to apply the SSM to their own dataset, it is advised to adjust the parameters accordingly.

Excitation parameter calibration

To reduce the degrees of freedom in the fit, some experimental dependent parameters are calibrated to reduce computation time and to avoid overfitting (details in the fitting procedure are in the next section). An adjustable neutral density filter is used to change the laser intensity at the diamond. Then the $m_s = 0$ state PL data are measured and fitted for β, shown in figure 3.2.

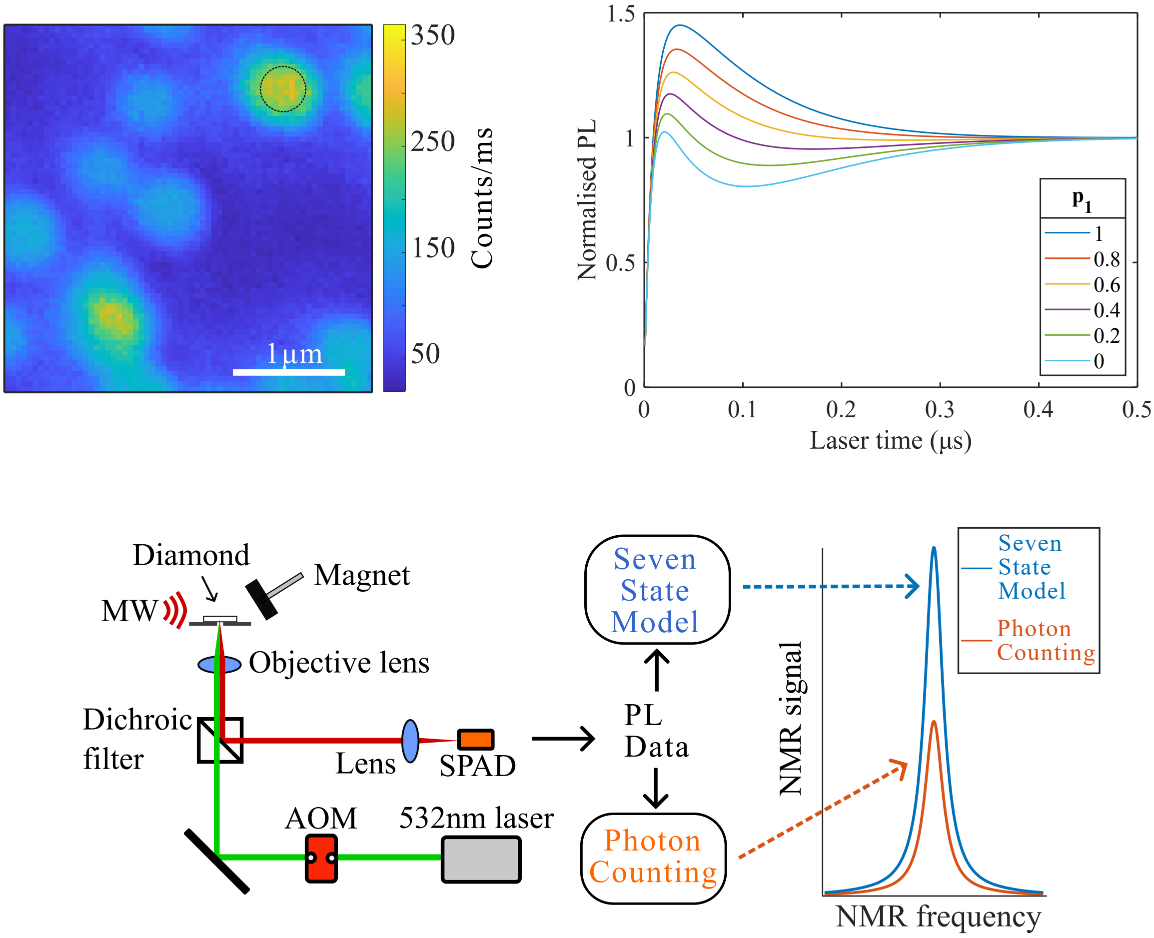

Figure 3.1: **Top Left** shows a typical confocal image with a single NV emitter highlighted. **Top Right** shows simulated emissions using the SSM at different populations of the $m_s = 0$ state (p_1). **Bottom** is a schematic of a confocal setup; PL data is collected by an SPAD and analysed in two different methods (seven-state model and photon counting), resulting in different signal-noise ratios.

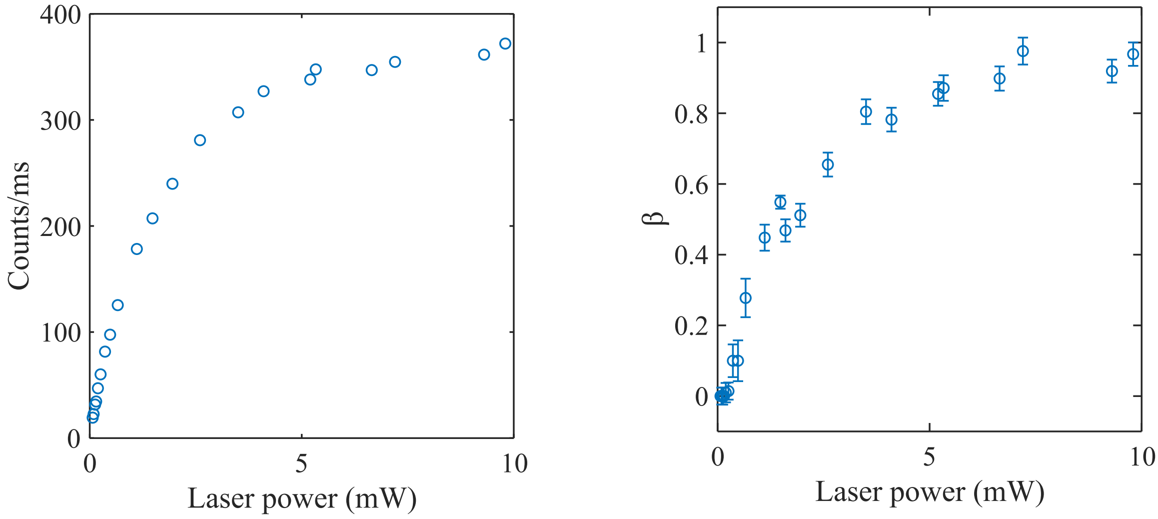

Figure 3.2: **Left** shows the number of red photons collected vs laser power, showing an agreement in behaviour between this calibration curve and the calibration of β. **Right** shows fitted β vs laser power.

3.5 mW of 532 nm light was used before the microscope objective, which translates to $\beta = 0.7$.

Charge state population calibration

The steady state charge state distribution was investigated. This measurement aims to determine the NV$^-$ charge state initialisation percentage after a typical green laser pulse. It involves an orange laser (594 nm, 2 µW, 50 ms) to excite the NV states without significant perturbation to the charge distribution. The subsequent PL under spectral filtering will alternate between different fluorescent rates depending on the present charge state of the single NV centre [101]. This will result in a bimodal distribution in a histogram analysis as shown in Figure 3.3. A red laser diode (630 nm, 300 µW, 100 µs) was used for charge state initialisation, which can efficiently transfer the NV charge population to the neutral state [136]. Then under an orange readout (594 nm, 2 µW, 50 ms), an unimodal distribution of emission rates was observed, which was used to define

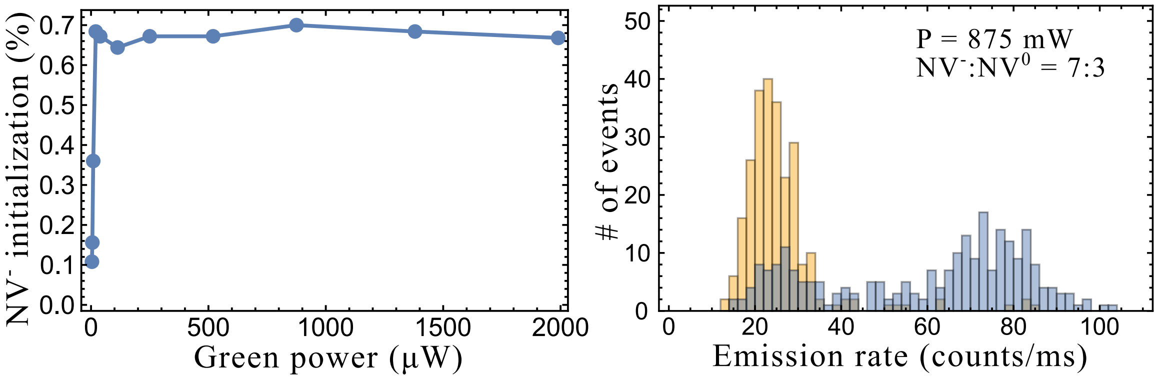

Figure 3.3: **Left** shows the percentage of NV$^-$ charge state at different laser power (P), showing that under sufficient illumination, 70% of the NVs are in their negative charge states, which supports the parameter used in the SSM. **Right** presents an example of the distributions under different initialisation conditions, the emission events labelled in yellow are initialised by the red laser and blue are by the green laser at 875 μW.

that emission rates under 45 photons per millisecond are due to the NV^0. A green laser with variable power (P) for the same orange readout procedure was use,d and the emission events were counted. It was concluded that at the power used in the main experiment, $\mathrm{NV}^0 : \mathrm{NV}^- = 3 : 7$, shown in figure 3.3, which is in agreement with literature [43, 166] and validates the parameter used in the SSM.

3.2.4 *Post processing and analysis of PL data*

Experimentally, the time-tagged PL data from a single NV centre is captured and integrated over a chosen time interval at the end of each measurement sequence (figure 3.4). Each individual PL trace is then analysed using two different methods. The first method, photon counting (PC), integrates the section of data where PL changes the most with $\mathbf{p}(0)$, resulting in a spin state-dependent contrast readout. The integration region is defined by a rectangle with a width of 300 ns starting from the 50 ns after the onset of the laser readout pulse. This is usually determined on an *ad hoc* basis to maximise SNR due to different PL responses with β. The second method, SSM, investigates the PL data with more complexity. $P_{|1\rangle}(0)$ was determined by fitting the SSM to measured PL data using MATLAB's trust-region fitting procedure, instead of a simple integration in a boxcar-shaped region (see figure 3.4). By fitting to a more complete model, the method captures more features in the PL and extracts additional spin information that may either fall outside the boxcar region or have a more complex dependence than a change in counts (for example, the shape of the PL trace changes, but total counts within the integration region remain similar). In addition, the PC method can only achieve a maximum contrast of 30%. This limit is caused by the fact that there is still a probability of up to 70% that the $m_s = -1$ excited state relaxes radiatively, thus the collected PL contrast (that is, the difference in PL intensity between the $m_s = 0$ and -1 states) is limited. In the SSM, the full photophysics description accounts for the different transition pathways and probabilities, so its output recovers the full spin information/"contrast", surpassing the 30% limit.

During the fit, a weighting factor offset based on the difference in calculated PL between $m_s = 0$ and $m_s = -1$ states was used in the fit. This is the modelled region, where the greatest change in PL dependency on $P_{|1\rangle}(0)$ is expected. The fitting procedure is an exercise to sweep the parameter space to reduce fitting residuals; by introducing the weighting factor, the method places a higher emphasis on regions of data where the

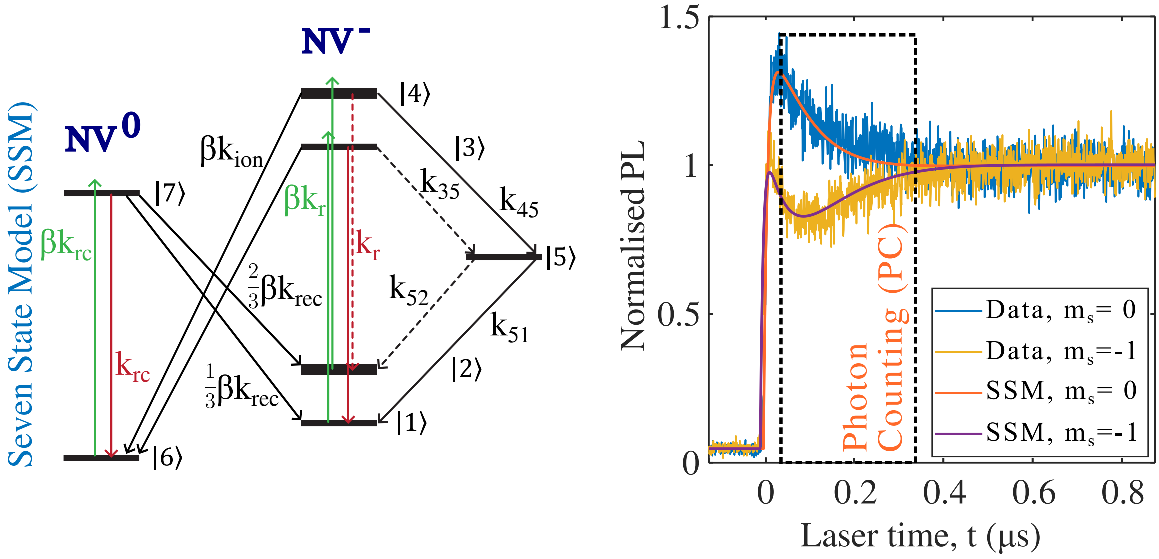

Figure 3.4: **Left** shows the NV electronic structure and transitions illustrated by the SSM. The green transitions are induced by the 532 nm laser, red transitions are radiative and dotted transitions are less probable. **Right** shows PL data measured (blue and yellow lines) and fitted by the SSM (orange and purple lines) with and without a MW π pulse prior to measurement. The region for photon counting is shown by the dotted box.

PL has strong physical dependence on the spin states and filters out unwanted non-spin-related PL information. In addition to $P_{|1\rangle}(0)$, the fitting procedure also evaluates a timing offset, which shifts the SSM PL forwards and backwards in time to account for timing errors such as clock mismatches. The other empirical parameters (β and $P_{|6\rangle}(0)$) are held constant to reduce fitting complexity and computing speed.

3.3 RESULTS

The results obtained via these two readout methods were then compared in two quantum sensing protocols. In the first, a coherent spin-state manipulation of the NV via an applied microwave field is demonstrated; otherwise referred to as a Rabi experiment. In the second, the NV spin is used to detect nuclear magnetic resonance signals from nearby ^{13}C nuclei in the diamond lattice. Both of these experiments are of fundamental importance to NV-based measurements, demonstrating the broad applicability of the method developed in this work.

3.3.1 *Demonstration via coherent microwave driving*

In the case of a Rabi experiment, resonant MW pulses of varying duration, τ, are applied to achieve τ-dependent degrees of NV spin population transfer from $|1\rangle$ to $|2\rangle$, as shown in figure 3.5. After each MW pulse, a laser readout pulse of 5 µs is used, and PL data is collected. Before the next MW pulse, a wait time of 1.5 µs is employed to ensure the populations relax to the ground spin states. The pulse sequence is repeated for a total photon integration time of t_{avg}, and the accumulated PL data is recorded at every t_{avg} = 1 s. Due to memory constraints, the experiment is paused after every 5 min to transfer the PL data and refocus the laser onto the NV centre in response to any drift that may have occurred.

The PL data from the Rabi experiment are analysed by the two methods described in subsection 3.2.4. The extracted contrast and $P_{|1\rangle}(0)$ determined from the SSM fit are plotted against the MW time (examples are shown in figure 3.5). It is worth noting that the values of contrast and $P_{|1\rangle}(0)$ are different due to the methods employed. The PL contrasts are obtained by integrating PL counts from $t = 50$ to 350 ns and dividing them by the integrated counts at the back of the laser pulse (4.5 to 4.8 µs). For a single NV centre, the maximum dark state to bright state

PL contrast is usually 30%. This can be explained by the photo physics described in section 3.2.2. For the experiment in this subsection, the high laser intensity of 400 kW/cm^2 ensured the single NV centre was saturated and not susceptible to laser intensity fluctuations. This resulted in a measured spin contrast of 20%. For the SSM, the values of $P_{|1\rangle}(0)$ are bounded between 0 to 1. Using the same set of data, the processed results using the SSM exhibit greater SNR over the measurement period when compared to the PC technique.

To quantify the improvement, a fast Fourier transform (FFT) is applied to the Rabi oscillations, then the FFT data is scaled to the same noise floors, shown in figure 3.5. The FFT data were fitted, and the peaks were compared. The signal-to-noise ratio was defined to be the fitted amplitude divided by the standard deviation of the noise floor. This quantification confirms that there is a significant SNR gain using the SSM method. An alternative SNR quantification method comparable to previous literature [118] that explores the residuals from a sinusoidal fit of the Rabi time data was also employed, and showed similar improvements (see next subsection). This comparison shows that postprocessing using the SSM method results in an SNR increase by a factor of 2 for a measurement time of 60 seconds, as shown in figure 3.5.

3.3.2 *An alternative signal-to-noise ratio (SNR) quantification method*

In the previous subsection, the SNR of the Rabi experiment was quantified by using a Fourier transform and defined to be the fitted amplitude divided by the standard deviation of the noise floor. In this subsection, an alternative SNR quantifi-

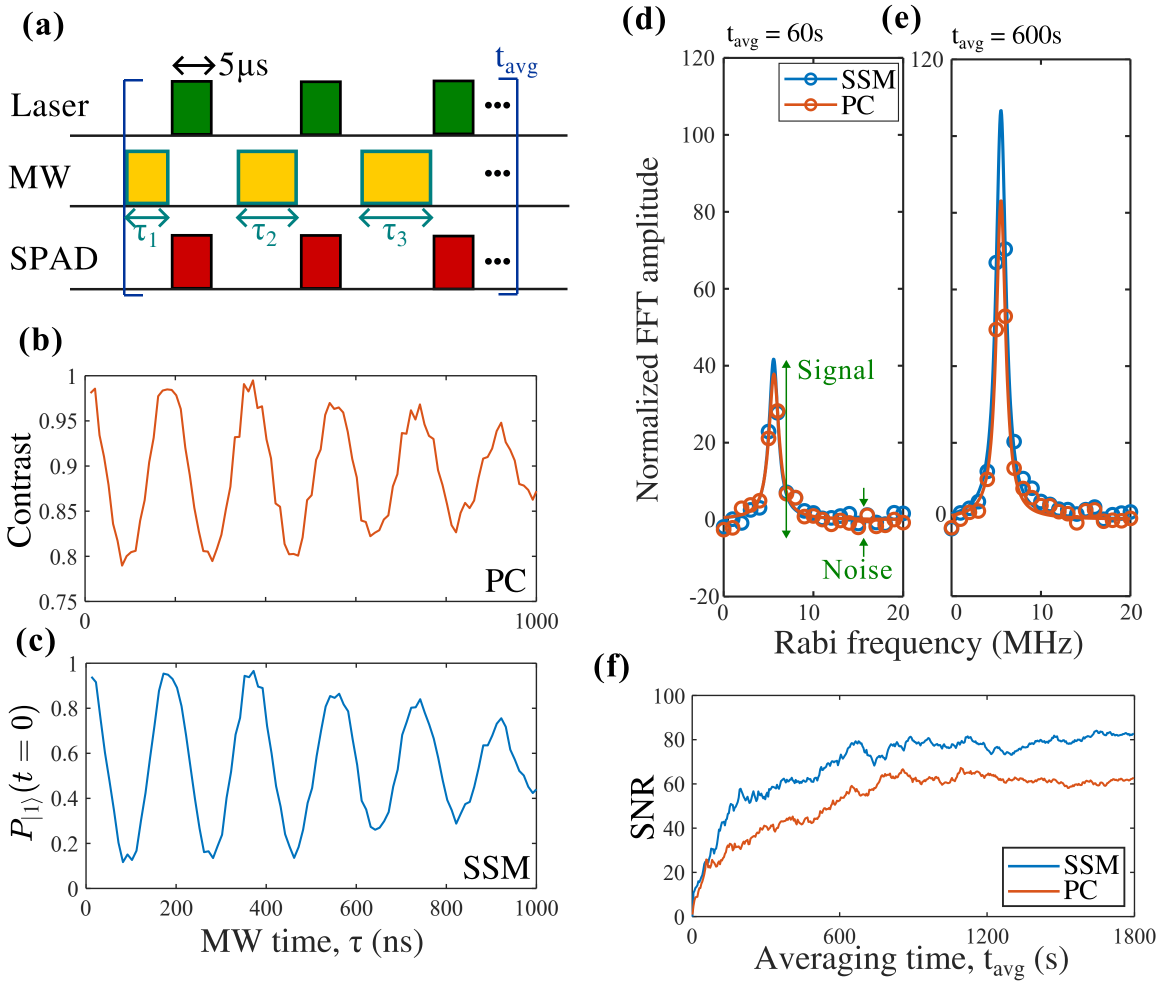

Figure 3.5: **a)** shows ulse sequence for coherent MW driving experiments. MW pulses are swept from 12 ns to 1 µs to vary the spin population, each followed by a laser pulse (5 µs) for readout. The SPAD is turned on during the laser pulses, with a maximum sampling rate of 10 GHz binned to 1.25 GHz (or 0.8 ns). The sequence is repeated for $t_{avg} = 1$ s intervals for a total time of 1800 s. **b) and c)** demonstrates the same Rabi measurement processed by PC and SSM at t_{avg} = 600 s, showing qualitative agreement between the two. **d) and e)** are the scaled (to the same noise floor) FFT comparisons at t_{avg} = 60 and 600 s, showing that SSM provides higher SNR compared to PC. **f)** presents variation of SNR with respect to t_{avg}, showing that SSM can achieve SNR gain of up to a factor of 1.5 and always above 1 for the t_{avg} considered here.

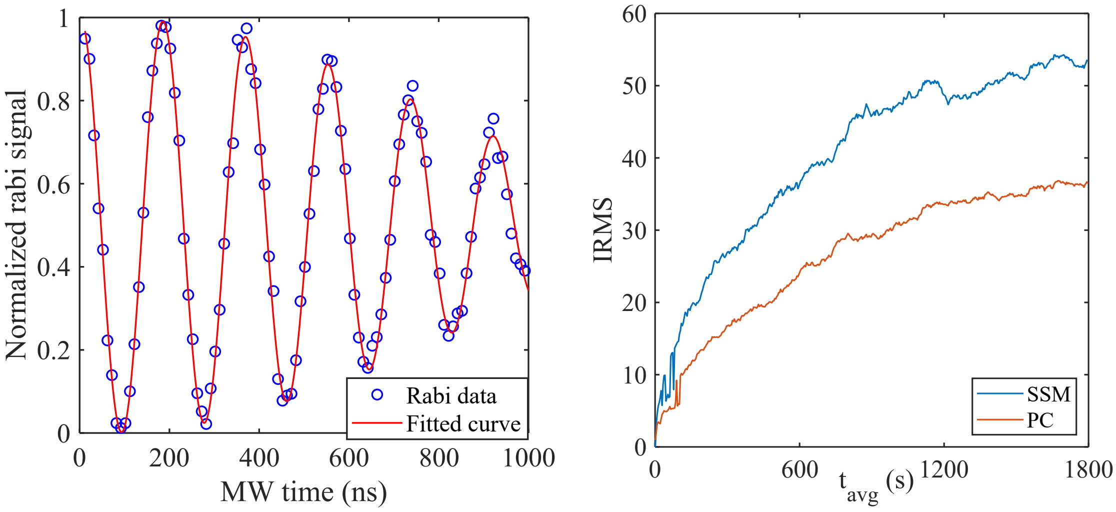

Figure 3.6: **Left** shows an example of a Rabi curve fit using the same data from the previous subsection. All Rabi data are normalised-from 0 to 1. **Right** presents an analysis of the SNR, which is calculated as the IRMS of the residuals from the Rabi fit at different t_{avg}, showing an agreement with figure 3.5.

cation method used in previous studies [118] is explored. The SNR of the Rabi oscillation can be calculated by fitting the normalised results to a decaying sinusoidal function of the form $A\cos(ft+\phi)\exp(-(t/a)^s)+c$, where A is the amplitude of the Rabi signal, f is the Rabi frequency, ϕ is the phase of the oscillation, a is the Rabi decay time, s is a stretch factor that accounts for a variation in the decay rates, c is an amplitude offset and t is the independent variable of MW time. The SNR is defined to be the inverse root-mean-square (IRMS) of the fitting residuals. Figure 3.6 illustrates the quantification method and shows the SNR improvement as a function of averaging time (t_{avg}).

Both methods show a similar trend and level of improvements, showing that the use of the Fourier transform method is consistent with previous literature. Although both methods can be used in a Rabi experiment, the Fourier-transformed data is a clearer illustration of the SNR, and its shape is comparable to an NMR spectrum.

3.3.3 *Demonstration via nanoscale detection of nuclear magnetic resonance*

As a second demonstration of this method's utility, a nanoscale NMR spectroscopy experiment was performed on a nearby ^{13}C nuclear spin. The NMR experiment is conducted by using an XY8-N pulse [40], as detailed in figure 3.7. The inter-pulse spacing time, defined by τ is swept, and a significant change in the $|1\rangle$ population is observed when ^{13}C Larmor period is matched to 2τ; which serves to define the NMR spectrum. The accumulated PL data for the NMR experiment is collected at every t_{avg} = 1 min throughout the single NV experiment.

Using a comparison method similar to the Rabi experiment in section 3.3.3, the SSM is then utilised for the NMR experiment where spectroscopy is performed on nearby ^{13}C nuclei within the diamond, illustrated in figure 3.3. The PL data from the XY8-N experiment are analysed using SSM and PC methods. The results are scaled to the same noise floor, and the peaks are fitted similarly to the Rabi FFT results in section 3.3.1 as shown in figure 3.3. From this comparison, an improvement in SNR of 1.36 is demonstrated via the utilisation of SSM versus PC approaches. This translates to a measurement time reduction of $1.36^2 = 1.85$.

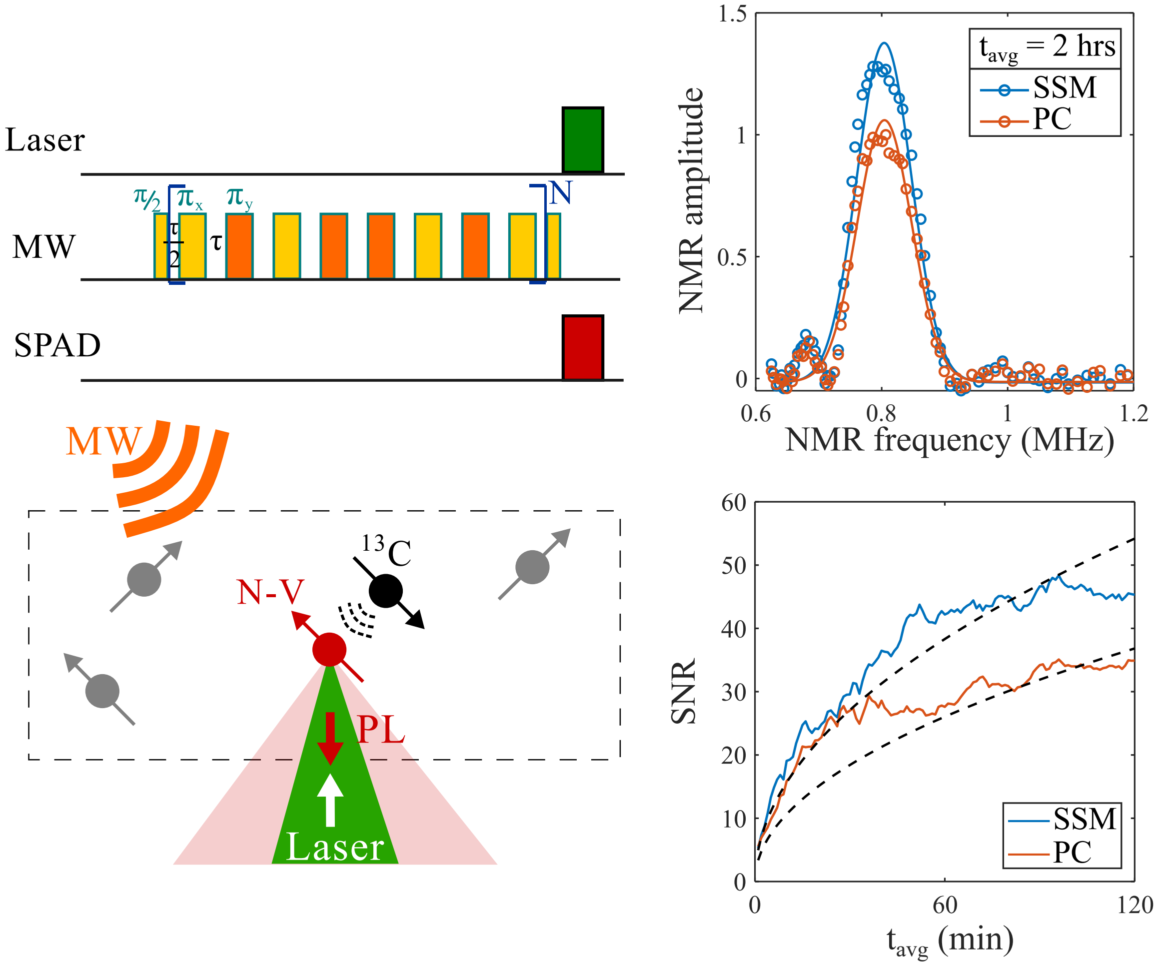

Figure 3.7: **Top Left** presents the pulse sequence for an XY8−N experiment. A MW π pulse is the duration of MW application needed to flip the NV spin state from $|1\rangle$ to $|2\rangle$. MW pulses shown in orange (y) have a phase shift of $\frac{\pi}{2}$ relative to the yellow (x) pulses, and $N = 2$ was taken for the experiment. **Bottom Left** illustrates the local spin environment to the NV centre. During an XY8−N experiment, a coupling to nearby ^{13}C spins was facilitated, thereby changing the NV spin state when close to resonance. This occurs when the inter-pulse spacing (defined by τ) is matched to the nuclear spin precession rate, which, for this experiment, was 0.825 MHz. **Top Right** demonstrates the scaled (to the same noise floor) NMR spectra of the ^{13}C, showing resonances at 0.825 MHz. The side-bands (the most significant at 0.7 MHz) are tentatively attributed to hyperfine interactions with nearby ^{13}C clusters, similar to that seen by Dréau et al. [44]. The data was fit to a Gaussian function with the 0.7 MHz side-band excluded. This demonstrates that SSM has a greater SNR compared to PC. **Bottom Right** shows an the evolution of SNR with respect to t_{avg}, taken at 1 minute intervals up to 2 hours.The rates of evolution are fitted to $a\sqrt{t_{avg}}$ (dashed lines) showing an SNR gain of $a_{SSM}/a_{PC} = 1.36$.

3.4 DISCUSSION

In this work, a new readout protocol for spin-based quantum sensing with the NV centre in diamond has been demonstrated. It is based on parameter fitting to a precise SSM of the NV photo-physics, from which the relevant spin state populations can be accessed. By introducing the SSM into the post-processing procedure, a sensitivity improvement of a factor of 1.36 is quantified in a nanoscale NMR experiment, implying an improvement in data acquisition times of a factor of 1.85, with the only expense being additional computation power. In addition to post-processing the data, this method may also be implemented during the experiment, owing to the fact that a calibrated SSM only requires the fitting of two parameters, namely, the spin state population and a timing offset.

Leveraging the improvements demonstrated here, the time to generate a nanoNMR spectrum on an external target near the diamond surface can potentially be sped up from a few hours to tens of minutes. This can also aid the laborious search process of co-locating the target of interest to an NV centre with unwanted spin noise contributions from its immediate surroundings. Such improvements can also be applied to other sensing protocols that have traditionally relied on the same approach to counting PL data, such as relaxometry and Ramsey interferometry. Opportunities for further improvement to the SSM include more refined measurements of the rate constants for the near-surface NV centres and alternatives to the fitting algorithms, which could come from machine learning protocols. [131].

The measurement speed enhancements demonstrated here provide critical performance improvements to time-limited experiments such as near-surface nanoscale quantum sensing. Extension into an ensemble of NVs for high-resolution NMR [60, 140], for example, would enable time-dependent monitoring of NMR chemical shift signals to improve the understanding of reaction dynamics in complex chemical systems.

4

NMR USING AN ENSEMBLE OF NVS

The previous chapter presented a novel method that can boost the SNR of a nanoscale NMR experiment using a single NV centre. Experiments at this scale allow the detection of nuclear spin clusters sized around a few nanometres on the diamond surface. Despite having a desirable spatial resolution, it suffers from certain drawbacks, including the use of a singular atomic-scale sensor [45], leading to slow signal acquisition. This chapter will discuss methods that address these drawbacks using an ensemble of NVs.

4.1 INTRODUCTION

Gaining NMR information at the nanoscale is critical for understanding behaviours of targets such as single molecules, spin networks and interface chemistry. Despite the successful demonstration of single protein NMR spectroscopy [100], single NV NMR spectroscopy remains elusive as the following technical challenges are yet to be resolved.

First, due to the small sensing volume, detection of liquid state samples typically requires the target to be stationary at the diamond surface. Otherwise, the target will diffuse out of the liquid volume before the measurement is complete [35].

One method of localising the target to the diamond surface is the use of functionalisation groups that can tether the target with high chemical selectivity [81, 111, 164]. However, the nanoscale surface environment of the diamond is complicated due to a variation of surface features, and creating uniformly distributed functionalisation groups with high selectivity can be challenging [171]. Furthermore, it is difficult to precisely create single NV centres at a desired lattice site [65]. Hence, the process of co-locating an NV centre to a desired target at a precise location on the diamond surface is based on probability, increasing overall experiment time and reducing reproducibility [100, 127].

Another technical challenge that requires addressing is the difficulty in controlling and passivating surface spin and charge environments. This can lead to poor charge stability of the NV centre from band bending and reduced coherence time from surface spin noise [134, 137, 176], rendering it difficult to address NV centres within 5 nm of the surface. As a result, both effects can reduce the interaction strength to the external target. Hence, due to these challenges, although single nuclear spin NMR sensitivity has been demonstrated [100, 156], detecting external targets with single spin resolution still remains challenging [45].

The detection of an external individual nuclear spin remains an outstanding goal for the field. In the near term, due to the aforementioned constraints, it is difficult to realise its full potential in chemical or biological settings. And the single NV experiments mostly find their use in proof-of-principle investigations and solid-state devices. To bypass these technical gaps, the use of an ensemble of NV centres can be considered at a cost of spatial resolution [180].

To address an ensemble of NVs, the laser spot size is usually a few microns across in diameter, and the NV areal density is usually higher than $10^{11}\,\mathrm{cm}^{-2}$. This allows for an increased sensitivity compared to a single NV measurement, because sensitivity is inversely proportional to the square root of the number of NVs [143]. Also, by increasing the sensing volume and subsequently the number of targets and sensors, the target-sensor co-localisation and low throughput issues are alleviated.

The poor charge stability of shallow NVs near the diamond surface and surface spin noise remain issues for an ensemble NV sample [162]. In addition, an unwanted byproduct of increased substitutional nitrogen defect density is introduced when creating an ensemble of NVs, which leads to a decreased coherence time [15].

In most cases, the increased PL rate from the increased NV sensors addressed outweighs the negative effects from NV ensembles and allows for a more robust and simple NV NMR operation. This also allows for widefield microscopy, enabling NV MRI applications at the sub-micron scale [180]. The main disadvantage of NV ensemble NMR is that the spatial resolution is no longer at a few nm scale [141], and the increase in NV density leads to higher susceptibility to laser technical noise [173], given that the traditional laser densities do not saturate a high number of NVs.

This chapter will introduce two pathways to a boost in NV ensemble performance via spin readout improvements. Section 4.2 will reintroduce the SSM for an ensemble sample using the same confocal microscope as the last chapter. A major advantage of using NV ensembles is the capability of performing imaging on external targets, such as MRI [180]. Using scanning-

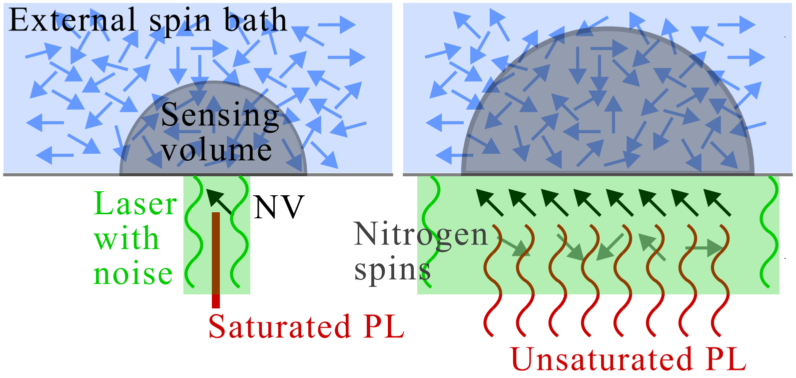

Figure 4.1: A summary of comparisons between sensing external NMR active spins (light blue arrow) using a single NV (black arrow) as shown on **Left** and an ensemble of NVs as shown on **Right**. Comparing the two, for a single NV, the sensing volume and hence, spatial resolution is significantly lower (nm scale) relative to an ensemble. The coherence time for a single NV can be up to ms [73], while for a near-surface ensemble, it is usually around tens to a few hundreds of µs [167]. For an ensemble, despite having unsaturated PL output and lower coherence time, it can achieve enhanced sensitivities of sub-pT/$\sqrt{\text{Hz}}$ [168] compared to a single NV of nT/$\sqrt{\text{Hz}}$ [178] from the increased PL count rate.

based methods such as confocal microscopy offers advantages such as resolving PL information with ns time resolution, which enables postprocessing enhancements and producing clearer in-focus images with depth control. However, compared to widefield methods, it suffers from slower imaging rate due to the scanning nature, higher chances of inducing phototoxicity to external samples due to a more focused laser spot and limited field of view, hence the easier to operate widefield camera based microscopy methods are more suitable and flexible in imaging NV response to external stimuli such as NMR effects in a real world application setting. Section 4.3 will discuss the impacts of laser technical noise on a widefield NV ensemble experiment. The description of the widefield setup can be found in section 4.3.1.

4.2 READOUT OPTIMISATION VIA POST PROCESSING

To further optimise the measurement speed of an NV NMR measurement, one can consider utilising the boost in throughput in an ensemble of NVs by applying post-processing readout optimisation protocols, similar to the method introduced in the previous chapter. The main workflow of the SSM remains unchanged for an ensemble of NVs, and a similar procedure was carried out. The same confocal microscope was used, and the laser intensity has been increased to 10000 $\mathrm{kW/cm^2}$ at the diamond surface with the same diffraction-limited confocal spot size. This corresponds to a laser power of 7 mW at the back of the objective, then focused onto a circular spot with a diameter of 300 nm. Meanwhile, neutral density filters were applied to the stimulated PL before the SPAD to keep the PL count rate below 1000 counts/ms, which is within the linear regime of the instrument's response curve; artefacts from the SPAD will be introduced.

The diamond sample used in this section employed a CVD overgrown layer with nitrogen gas introduced in the process at 0.002 sccm. The layer was then subject to a 10 keV Carbon implant with a dose of 10^{11} cm^{-2} and annealed at 1100°C under vacuum. The estimated NV density is $2 \times 10^{11}\ cm^{-2}$.

The first step of the workflow is to calibrate the parameters in the SSM for this ensemble sample. With the increase in NV density, it is now expected that the pumping rate of the SSM will be decreased, and hence the laser power parameter, $\beta = 0.028$, has been calibrated as shown in 4.2, using the same procedure as the last chapter. Time resolved PL traces at $m_s = 0$ and -1 states are manipulated by gating on resonance MW pulse duration is shown in figure 4.3 with the respective SSM simulation. It is observed that when comparing this with the single NV PL data as shown in figure 3.4, the ensemble data exhibits fewer features. The single NV data has an initial rise in the PL profile and a subsequent decrease before rising to the steady state point, and the ensemble data showcases a singular rise feature only. This is caused by the reduced pumping rate of βk_r from the NV$^-$ ground state to the excited state, where the rate entering the excited states is slower than the sum of the leaving rates, $2\beta k_r < 2(k_r + \beta k_{ion}) + k_{35} + k_{45}$.

Under these parameters, when the additional features are no longer present, the limitations of the SSM fitting protocol become amplified. This is demonstrated in figure 4.4 where the conventional photon counting method in a Rabi experiment results in a higher SNR compared to the SSM. The SNR quantifi-

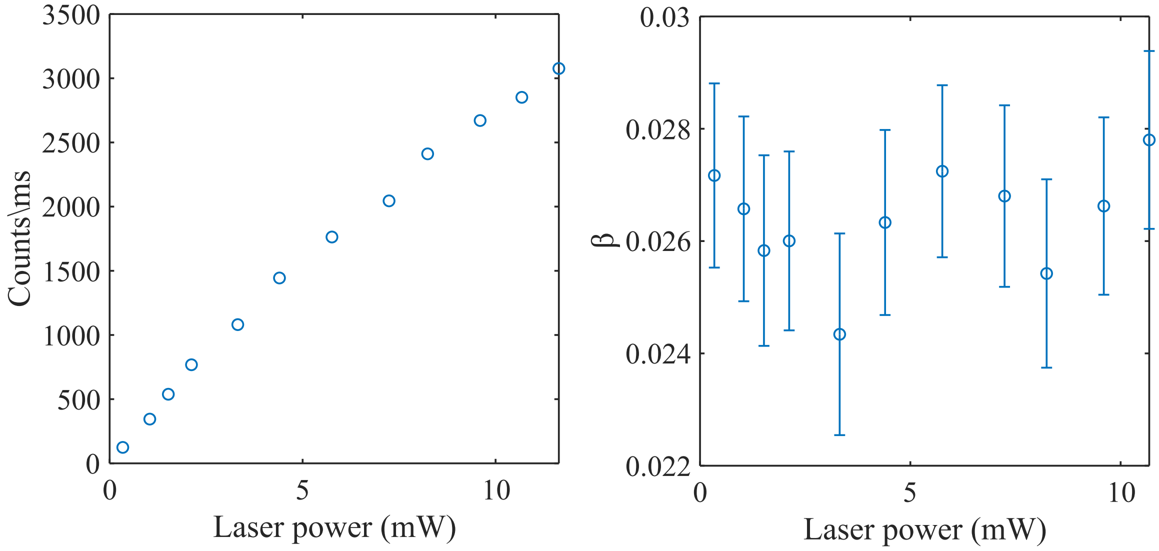

Figure 4.2: **Left** shows the PL count rate of the sample when excited at different laser powers. There is no saturation behaviour for this measurement, because an ensemble of NVs is used and the laser power that is accessible is not sufficient to saturate the NV density of $2 \times 10^{11}\,\mathrm{cm}^{-2}$. **Right** shows a calibration of β used in the SSM, and due to the use of an ensemble, the obtained $\beta = 0.028$ is significantly lower than the single NV case.

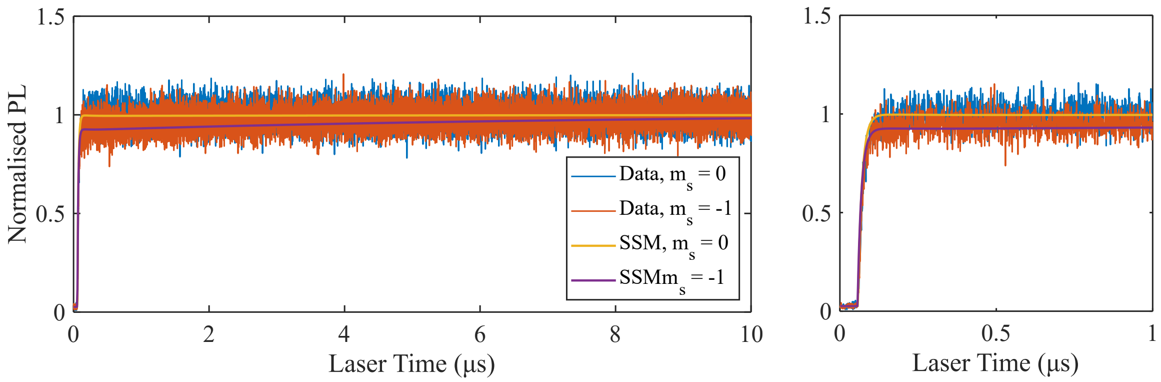

Figure 4.3: **Left** shows the PL response measured under a readout laser pulse of 10 µs for an ensemble sample at different spin states, shown in blue ($m_s = 0$) and orange ($m_s = -1$). The simulated responses are shown in yellow ($m_s = 0$) and red ($m_s = -1$). **Right** shows the response zoomed at the first µs of the measurement, showing that the PL only features a rising behaviour.

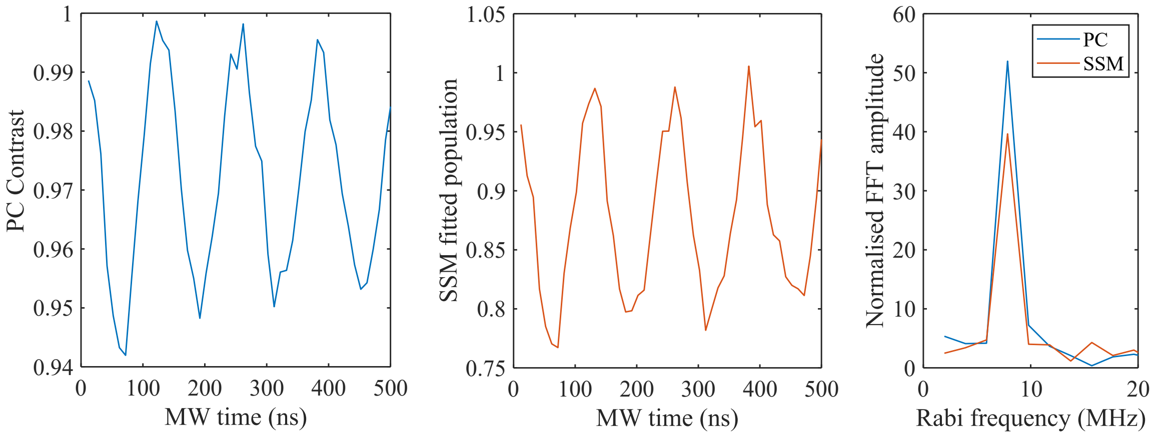

Figure 4.4: Rabi oscillations obtained using the photon counting method shown in **Left** and the SSM shown in **Centre** using the same PL data with $t_{avg} = 100\,\text{s}$. The photon counting method integrated the first μs of the PL and referenced against the last μs. The SSM method used the same parameters as the last chapter, except for $\beta = 0.028$. Although the oscillations obtained using the SSM resembles of that in the PC method, the SNR analysis shown on **Right** suggests that the SNR from the SSM is 24% less than the PC. The analysis is performed by comparing the peaks of the Rabi FFT with the noise floor normalised to the same level.

cation method remains unchanged from the previous chapter. The main limitation of the model is attributed to the fact that the rate parameters are not orthogonal to each other, so changes in PL behaviour can have multiple causes. For example, the charge state cycling rates and k_{45} can alter the NV PL in a similar way. In the case of a single NV experiment, such rates can be bounded more accurately compared to an ensemble, where it is reasonable to expect a distribution of certain transition rates due to variations in the local environment. If SSM's transition rates are not or cannot be accurately determined, the ability to achieve accurate relative initial spin state population from the fitting procedure erodes.

This is compounded by the fact that the measurement setup used in this section does not allow for a saturated coupling between the NV ensemble and the laser. The lack of laser power experienced by the NVs reduces the difference between the measured PL at different spin states, hence the reduction in contrast. This reduced variation in PL with respect to the spin states contributes to the reduced performance of this postprocessing method, in addition to the lack of features in the PL. Also, when the PL is no longer saturated, the measured emissions are more prone to laser noise. This is explored in detail in the next section.

Although in this particular experiment, the advantages of the SSM have yet to be realised, there exists of other scenarios where the SSM can achieve a better SNR for ensemble samples by increasing optical excitation power density. For sensing applications of non-biological samples where phototoxicity is not a consideration, such as magnetometry and solid state material characterisations, SSM is expected to provide an improvement when a higher power laser or optical cavities are in place [1]. In addition to laser power increase, if equipped with pulsed variable wavelength lasers, the NV transition rates can be more accurately determined by performing an excited state lifetime measurement. This will provide additional insights into the sample-dependent parameters used in the SSM and create a more accurate description of the PL model [76, 169]. In ensemble NV NMR experiments, the utility of SSM degrades due to difficulties in achieving PL saturation; the results presented here are an underestimate of its full potential. With additional tools, the SSM still has the potential of providing benefits to the NV readout.

4.3 IMPACTS OF LASER NOISE

The previous section has outlined that when an ensemble of NVs is used, optical saturation can be difficult to achieve and exposes the NV PL to laser technical noise. This section will explore how the laser noise impacts the NV ensemble-based NV-NMR measurements using a widefield camera.

4.3.1 *Comparison between two excitation sources*

A custom-built widefield microscope was employed for the experiments described in this section. Its general optical layout is similar to the work in the previous chapter, as shown in figure 3.1. The major differences are that a Complementary Metal–Oxide–Semicondu (CMOS) camera (Andor Zyla 5.5-W USB3) is used instead of the SPAD, and optical fibres are not used.

A diode-pumped solid-state laser (DPSSL, Laser Quantum Opus 2W) and a diode laser (Nichia NDG7575) are used in this comparison study. Both beams are modulated using an AOM (AA Opto-Electronic MQ180-AO, 25-VIS) and focused onto the diamond using an objective (Nikon CFI Plan Fluor 20x, NA = 0.5). The power of both laser sources is set to a maximum, where there is no significant power fluctuation to ensure proper stability during measurement. The laser spot size is approximately 50 µm in diameter and the laser power at the diamond is 70 mW. The PL is filtered using a dichromic mirror, and in postprocessing, the camera captured PL images are cropped to reduce dark noise. Similar electronics to those in the previous chapter are used to deliver MWs. The diamond sample used in this section is a CVD substrate (Delaware Diamond Knives) implanted with Nitrogen at 4 keV with 10^{13} cm^{-2} dose and subsequently annealed at 1000°C under vacuum.

The characteristics of the laser and PL were measured first. The PL was collected by illuminating the diamond with a CW laser and capturing a video where the exposure time per frame is 10 ms. The laser is measured in a similar manner by replacing the diamond with an optical mirror. Both sets of data are shown in figure 4.5. It is clear that the DPSSL performed better than the diode laser; under continuous illumination and monitoring, it demonstrates a tenfold improvement in RMS noise. The relatively noisy diode laser may be more susceptible to vibrations, or the spatial profile of the laser is inconsistent, as the video trace shows multiple surges in count rate. Figure 4.6 further confirms the noise level differences in spectrum and Allan deviation analyses. In the video analysis, a minor consistent increase in PL is detected in both sources. It amounts to an increase in count rate by 0.001% after each frame; the laser video did not exhibit such an increase. This increase in PL rate is attributed to the charge state effects, where prolonged green excitation can lead to a transfer of NV^0 population to NV$^-$ [61].

To understand how laser fluctuation translates in an NMR measurement, the NMR signal from ^{13}C spins within the diamond sample was measured using the same widefield microscope. The pulse sequence utilised in the following experiment is the same XY8 protocol from the previous chapter, and the measured spectra are compared in figure 4.7. Because of the low coherence time of the sample used, the baseline of the NMR spectrum is not flat and exhibits a significant incoherent decay. Thus, a fitting procedure is used to characterise the SNR. A function that describes an exponential decay with a Lorentzian

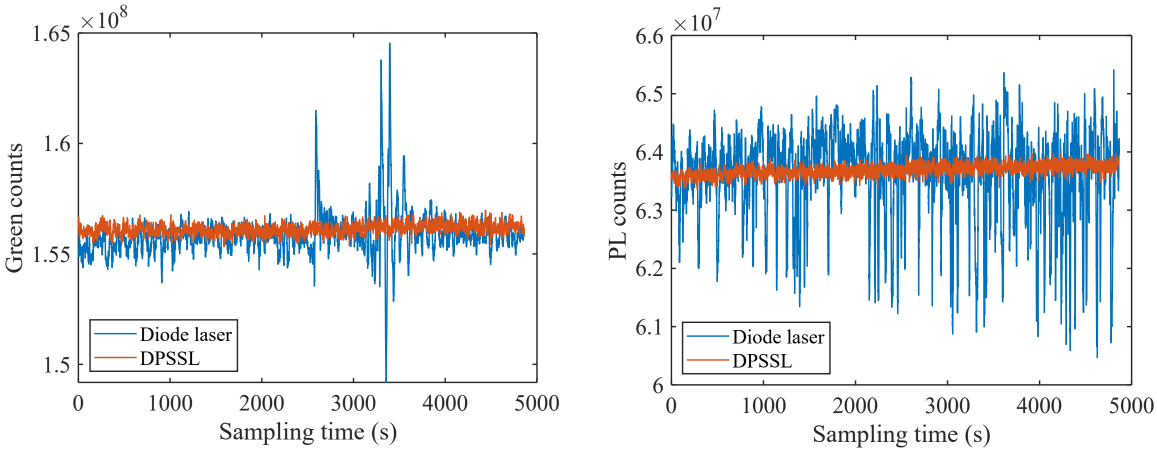

Figure 4.5: **Left** shows the total number of green photon counts captured by the camera integrated over the cropped field of view. It compares the reflected green counts using the diode laser (blue) and the DPSSL (orange). **Right** shows a similar comparison for the captured NV PL. When examining the green, the diode laser exhibits 0.7% of noise, and the DPSSL exhibits 0.14% and for the PL, 1.2% and 0.14%, respectively. The green and PL measurements were conducted under similar laboratory conditions.

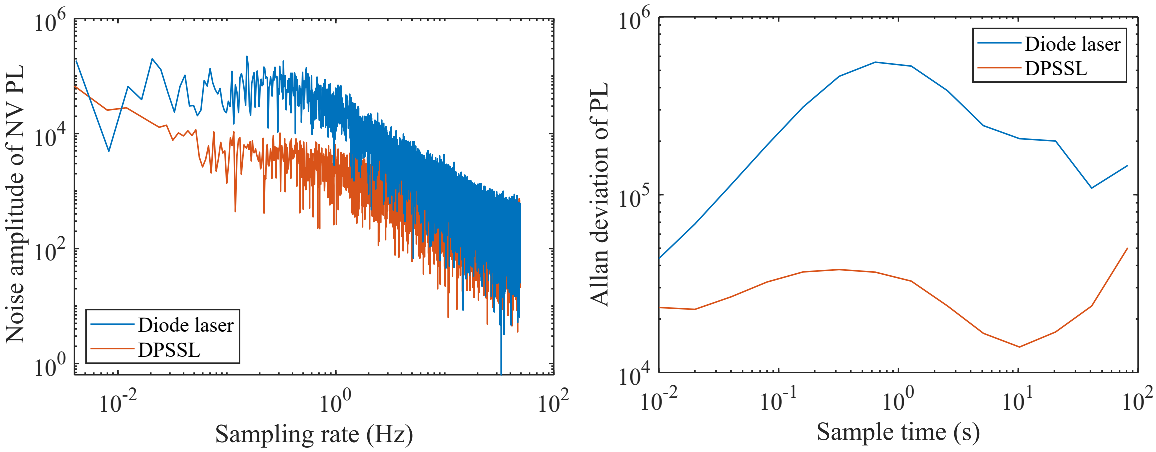

Figure 4.6: **Left** shows a comparison of spectral noise density between the PL generated under the two excitation sources. **Right** shows a similar Allan deviation comparison. Both analysis confirms that the DPSSL used has a better noise performance.

peak contribution is used, and by extracting the fitting residuals, the SNR of the NMR measurement is calculated. The SNR is defined by the inverse root mean square of such fitting residuals. The SNR behaviour of the NMR measurements using the DPSSL and laser diode excitation sources with respect to the number of experimental repetitions is investigated and shown in figure 4.7. The SNR increases in a square root manner characteristic of random noise, as the number of averages increases. But above 300 repeats, the SNR stopped improving. This is attributed to the long-term drifts of the system and agrees well with the PL Allan deviation results in figure 4.7, as 300 repeats for these pulsed NMR experiments equate to a total PL time of approximately 10 seconds, where the Allan deviation began to increase. There are many factors influencing this drift effect, but for this comparison study, both excitation sources' NMR SNR began to plateau at a very similar time and because both lasers are temperature controlled, thus it suggests that such drift is not significantly influenced by the optical elements, but by drifts introduced from other sources, such as thermal expansion/compression and vibrations along the optical path.

Comparing the two laser excitation sources, the NMR response measured using the cleaner DPSSL demonstrated a higher SNR performance, but only by 25%, not as significant as the preliminary studies of an order of magnitude. It is reasonable to assume that any gains from the laser source itself will be diluted in an NMR experiment due to contributions from other sources, such as spatial variations in the optical paths, vibrations caused by the microwave deliveries. In the next subsection, a simulation of NMR results influenced by only PL noises will be conducted, and thus, this dilution factor can be estimated.

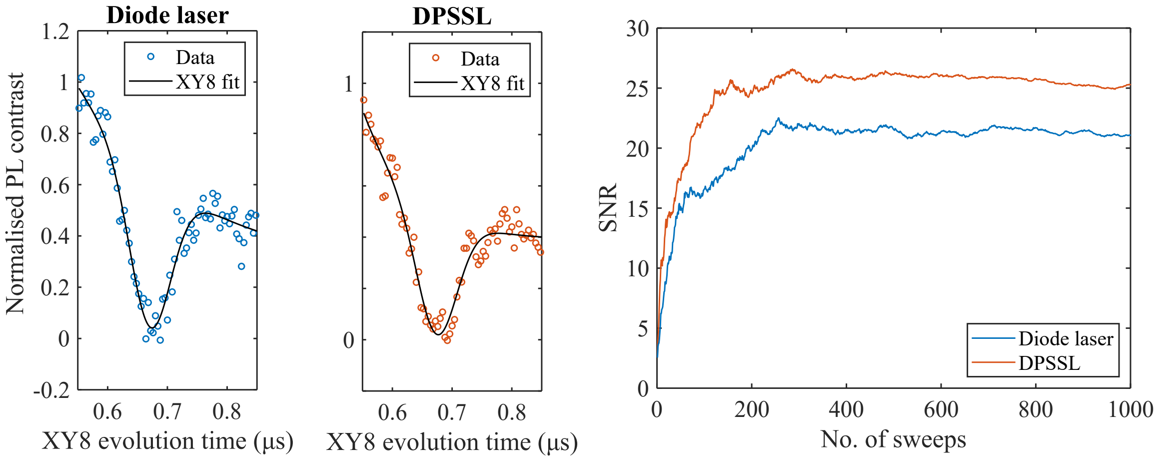

Figure 4.7: **Left** and **Centre** show measured NV NMR spectra of ^{13}C using the diode laser and DPSSL excitation sources, respectively and fits to the XY8 function. The background field for the experiment was 70 mT, and the number of π pulses in the pulse sequence is 32. The readout laser time is 9 µs, and the NMR spectra are taken after 50 repeats. Each measured point on the spectra contains approximately 400 cycles of the pulse sequence, which totals to 10 ms of camera exposure time per point. **Right** shows the SNR evolution for both lasers as the number of experimental repeats is increased, showing a 25% SNR improvement for the DPSSL compared to the diode laser.

4.3.2 Simulation of NMR performance under different laser noise levels

To perform the optical simulation of the widefield experiment, the structure of its pulse sequencing will be introduced first. Unlike the confocal microscope, which employs a SPAD to time tag PL photons at the ns scale, the camera used in the widefield is limited to 100 frames per second (fps). As a consequence, the manner of repetition is different. If one NMR measurement with X number of spectral points $(S(\tau_1), S(\tau_2), ..., S(\tau_X))$ requires Y number of readout cycles, the confocal pulse sequence performs the entire measurement and repeats the full sequence after. It follows the pattern of $(S(\tau_1), S(\tau_2), ..., S(\tau_X))^Y$. The photon counter will then be able to collect and distinguish the PL information at each individual τ and perform post-processing to obtain optical contrast as detailed in the previous chapter. For a camera, due to the lack of temporal resolution, each individual measurement is bundled together and repeated immediately within the bundle, and the next $S(\tau)$ measurement occurs when the repetitions are complete. It has the following pattern $S(\tau_1)^Y, S(\tau_2)^Y, ..., S(\tau_N)^Y$ as exampled in figure 4.8. Y is selected so each $S(\tau)^Y$ usually uses tens of ms of time, which is resolvable under a camera exposure. The camera collects all the photon counts within the exposure time, including the dark counts when the laser is not active, and the total counts are referenced to produce a contrast. For NMR measurements, the referencing is performed by subtracting the total number of counts from a particular MW sequence with τ evolution time against the same sequence with the same evolution time, but the final MW pulse is $3\pi/2$ instead of $\pi/2$. This pulse projects the NV spin vector towards the $m_s = \pm 1$ state instead of the $m_s = 0$, and the difference in photon counts between the two projections becomes the contrast.

This referencing is also known as phasing cycling.

The simulation is set up using the normalised PL response at the ns timescale from the SSM with an empirically determined spin state population distribution from the previous subsection. It is then coupled with a dark time, accounting for the duration of the MW sequence and shelving time. This is then repeated for Y cycles. Figure 4.8 illustrates an example of this step. The simulation then uses the data from figure 4.5 to calculate the expected number of photons at this timescale and its associated noise level, including dark noise, which is exemplified in figure 4.9. Three different noise profiles were considered for the comparison study: the diode laser with 1.3% RMS noise, DPSSL with 0.14% noise and a hypothesised excitation source (HES) with 0.01% noise. These percentages represent the noise level captured at 10 ms of camera exposure time, and the simulation converts it down to the ns timescale and uses a normal distribution noise profile. Any dark counts with noise were added as an offset.

The next step of the simulation sums the total number of counts and repeats the same simulation for the $m_s = -1$ spin projection. The normalised contrast is then determined for this particular τ, and the simulations proceed to the next point of the NMR spectrum. When all of the points on the NMR spectrum are computed, this constitutes one sweep of the experiment, and the SNR is calculated for this sweep in the same manner as the last subsection. Any subsequent sweeps included a minor increase in PL count rate, accounting for the drift ob-

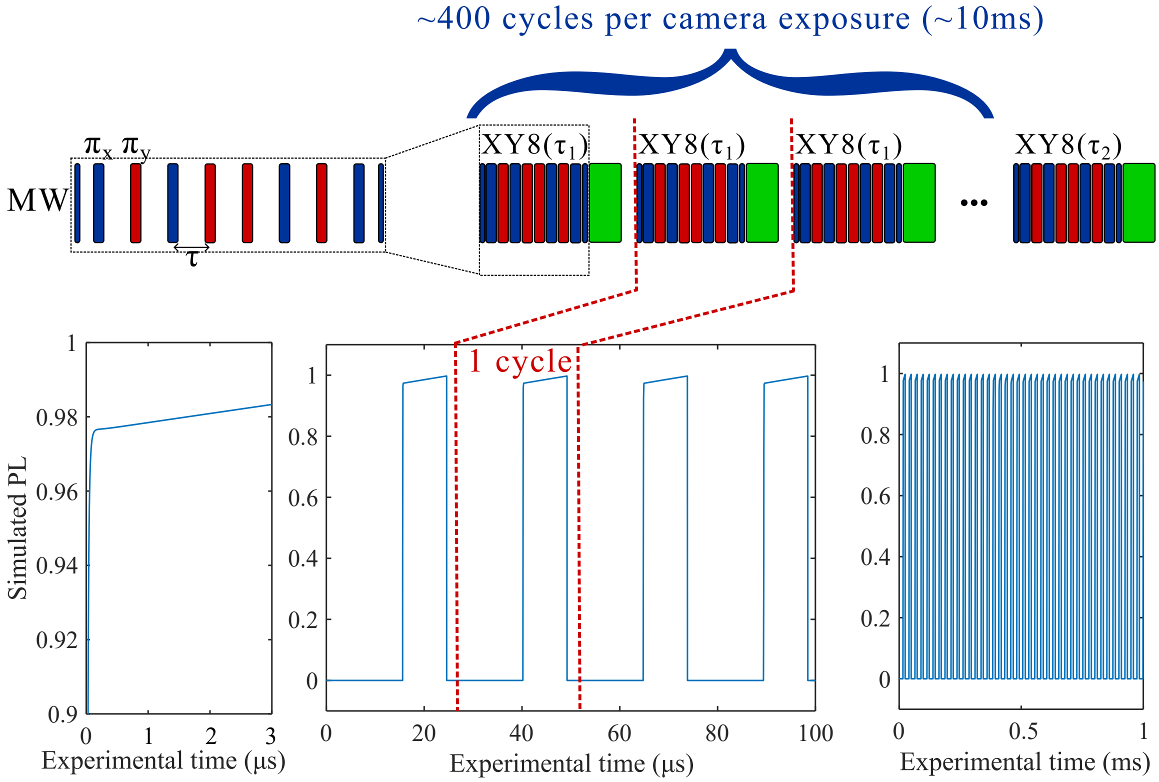

Figure 4.8: **Top** illustrates the measurement timing sequence in a wide-field experiment, where each XY8 sequence with a fixed interpulse spacing, τ are repeated sequentially for hundreds of cycles to fill the camera exposure time of tens of ms. For the simulations in this subsection, during one cycle, readout laser time is 9 μs. The dark time, which is the sum of the shelving time, microwave time and evolution time, is 15.6 μs. Each camera exposure contains 407 cycles, which amounts to an exposure time of 10 ms. Simulation parameters are based on experiments in the previous subsection. **Bottom** shows the simulated PL profile without noise for different timescales from a few μs within a laser pulse in **Bottom Left** to 100 μs, which consists of a few cycles in **Bottom Centre** to one tenth of a camera exposure in **Bottom Right**. Red dashed lines represent a correlation between the pulse sequence diagram and the simulation timeline.

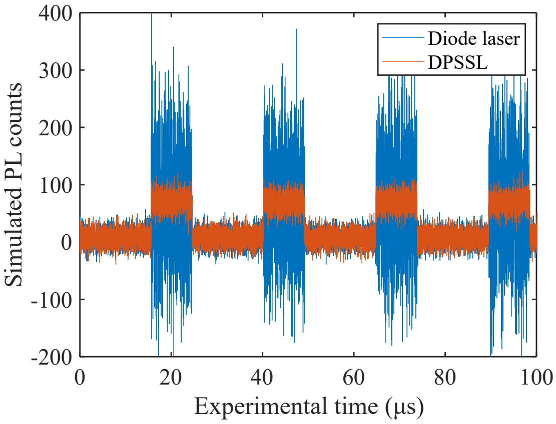

Figure 4.9: An example of simulated PL with noise profile added from the diode laser (blue) and the DPSSL (orange). The noise profiles are described in more detail in the main text. Note that the camera cannot capture the photons at this timescale and only reports the total number of counts during the exposure. The increase in the simulated PL occurs when the readout laser is turned on.

served in figure 4.5 and the SNR evolution as a function of number of sweeps is shown in figure 4.10.

The goal of the simulation is to construct an NMR experiment that is only affected by optical noise and understand how laser intensity noise affects the measurement, independent of other noise sources present. Comparing the SNR evolution against figure 4.7, the simulation results in figure 4.10 showed that the SNR increased in a square root fashion as expected for randomly distributed noise, but it did not exhibit any significant plateauing effects as previously observed in figure 4.7. Thus, it can be deduced that any long-term drifts in these wide-field measurements are not optical as the simulation included a similar level of PL drift, but did not show a similar level of the platuing effect. The drifts are tentatively attributed to mechanical effects, such as vibrations altering the optical paths or

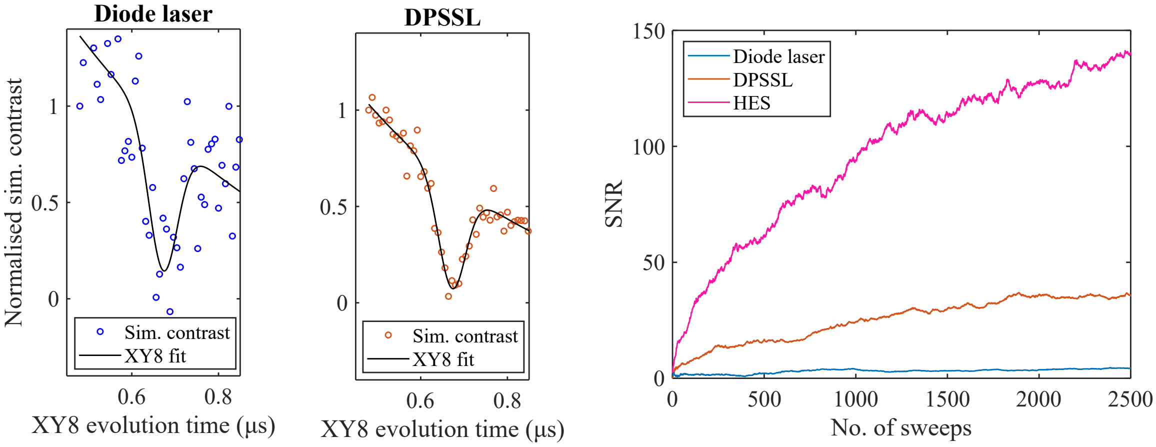

Figure 4.10: **Left** and **Centre** show the simulated NMR spectra obtained from the simulated PL profiles of the diode laser (blue) and DPSSL (orange), and illustrations of the XY8 fit for SNR quantification purposes. **Right** shows the SNR evolution for the two excitation sources and an additional hypothesised excitation source (HES, purple, see main text). The SNR at the steady state shows a gain by a factor of 7.5 from the diode laser to the DPSSL and a factor of 4 from the DPSSL to the HES at 2500 sweeps.

the PL focus or the magnetic alignment, which can all impact the NMR spectra on longer time scales.

By directly comparing the SNR performance between the diode laser and DPSSL, a gain by a factor of 7.5 using the cleaner source (another factor of 4 when comparing with the HES) can be achieved. Comparing the gains obtained from the optical simulation (a factor of 7.5) against the experiment in the previous subsection (a factor of 1.25), where the simulation parameters are from, there is a significant discrepancy. This suggests that optical noise contributions are not as significant as one would expect from the preliminary investigations.

The widefield imaging system used in this section is a typical design featuring optomechanical elements that are common in this field of study. Thus, there is a high-level of applicability of the findings from this section across the NV sensing field. It is advised that when considering the implications of individual NV NMR widefield imaging components, it is more appropriate (or sometimes more cost-effective) to explore other avenues before improving the noise level of the laser excitation source. For example, reducing lab temperature variations and minimising mechanical vibrations.

4.4 A DISCUSSION ON SPECTRAL LINEWIDTH

This thesis so far has mainly considered the SNR or sensitivity of an NV NMR measurement. This subsection will explore the NMR spectral linewidth, which serves as a motivation for the next part of the thesis.

All the NV-based NMR measurements so far in this thesis employed the XY8-N protocol that uses the decoherence rate of the NV to sense nuclear spins. Although the NV sensor boasts key advantages such as room temperature operation, biocompability and nanoscale sensitivity, there are certain challenges that limit the NMR performance, especially around the measured NMR spectral linewidth, which is critical in obtaining key chemical information [45].

The first challenge is the purity of the diamond host material. A number of undesired magnetic spin noise present within the diamond bulk and on the surface of the diamond, including substitutional Nitrogen spins and dangling bonds at the diamond surface interface, can decohere the long preserving coherence time of the NV sensor. This challenge inhibits the NV's intrinsic coherence time, which limits the NMR linewidth [33]. The linewidth obtained from the XY8-N or other dynamical decoupling protocol largely depends on the number of π pulses used, which narrows the filter function [40]. However, because the interpulse spacing has to be kept constant, increasing N means that the total evolution time, which is the time that the NV is exposed to the external spin noise bath, is lengthened. Thus, there exists an upper limit in N. If the NV coherence is diminished, decoherence-based sensing vanishes. Usually, the upper end of NV coherence time is around a few hundred µs for an ensemble (ms for a single), which can sustain approximately 512 π pulses when sensing nuclear spins corresponding to a linewidth of sub-MHz, similar to the spectrum shown in figure 4.11. To achieve resolution where chemical information can be resolved (sub-Hz), extreme measures such as superconducting magnets to resolve chemical shift lines (H_{CS} depends on B_0) and extending sensor coherence time via the exploita-

As discussed before, surface noise also forces the NV deeper into the lattice, reducing the sensitivity of external spins.

tion of parent Nitrogen nuclear spin memory can be used [7].

One can also consider the use of correlation spectroscopy, where the linewidth limit is improved from the T_2 time of sub-ms to the T_1 time of ms.

Although there are examples where the coherence time restrictions can be mitigated, there is a second and perhaps more challenging NV NMR linewidth hurdle. In nanoscale systems, the NMR targets undergo rapid tumbling, which averages out the spin coupling effects [142] (see motion averaging discussions in chapter 1). In induction-based NMR spectroscopy, this leads to an extension of the spin relaxation time that narrows the spectral linewidth (compare solution state NMR with ss-NMR). However, in nanoscale NV NMR, where the experimental time is much longer than the diffusion time of water, such effects impose a further relaxation mechanism that broadens the spectral linewidth [154]. Thus, demonstrations of nanoscale NMR experiments typically involve external samples with low levels of translational movement, such as immobilised or confined targets on the diamond surface and targets with inherently low diffusion constants [96, 106, 152] and increasing the sensing volume [7]. Single molecule high spectral resolution NMR has yet to be demonstrated and requires further diamond material, target immobilisation and microwave engineering. If realised, such achievements can have paramount impacts on the fields, such as medicine, biology, chemistry and material sciences.

So far in this thesis, methods of improving NV NMR performance have been introduced for single NV and NV ensembles experiments. However, due to the aforementioned hurdles, NMR linewidth remains a significant challenge for the scenarios discussed so far. In the next part of the thesis, NV NMR

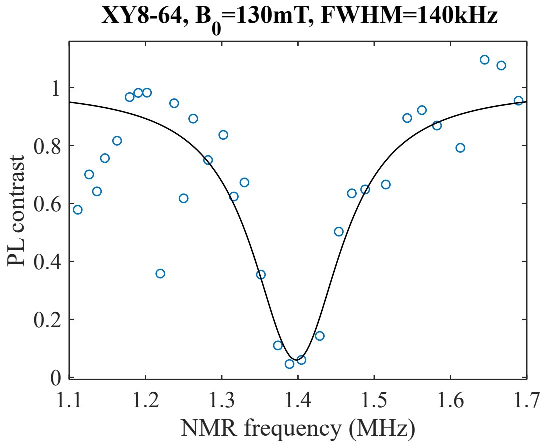

Figure 4.11: A NV NMR spectrum measured on the confocal microscope using XY8-64 (512 pi pulses) demonstrating 130 kHz of fitted full width half maximum (FWHM). The target nuclear spin is the internal ^{13}C at a background field of 130 mT. Due to the high number of pulses used, the inherent coherence of the NV at this stage is significantly diminished, and the measurement required 20 hours of averaging. The diamond sample used in this figure employed a CVD overgrowth layer with Nitrogen gas incorporation at 0.02 sccm and subject to Carbon implants at 100 keV with 10^{11} cm^{-2} dose then annealed at 1100°C under vacuum. The spin echo T_2 time is 120 µs.

with ppm spectral resolution will be explored using diamond samples with deep layers of NVs.

4.5 CONCLUSION ON ENSEMBLE EXPERIMENTS

In this chapter, two pathways towards improving NV ensemble experiments have been explored. The first pathway aimed to improve the readout performance through the use of the SSM. During the investigation, it was revealed that the SSM's potential to improve SNR in an ensemble context is more difficult to achieve compared to single NV experiments presented in the last chapter. This is predominantly caused by the difficulty of achieving PL saturation, which in turn reduces the features available in the measured PL, thus limiting the performance of the SSM fitting. However, with additional tools such as the use of laser cavities to boost effective excitation power and advanced spectroscopic techniques that enable a more accurate description of the NV photophysics, there exists a pathway to realise its full potential.

The second pathway showcases a technical investigation on the use of different lasers in a widefield experiment. Simulations and experiments have shown that there exists a potential for a cheaper diode laser alternative to the DPSSL in NV applications, especially in settings outside the laboratory, where SWaP considerations are more critical.

Part III

HIGH SPECTRAL RESOLUTION NV-NMR

Because of diffusion, it is challenging to combine high NMR spectral resolution at the nanoscale. In this part of the thesis, I'll explain and demonstrate the use of quantum heterodyne protocols that can reach sub-Hz linewidth. I present the journey I took to build this experiment and the technical discussions around the magnetic stability and uniformity, electronics and timing controls, material, and optics. I'll conclude with a plan to incorporate this apparatus with flow chemistry using microfluidics.

5

NV-NMR VIA QUANTUM HETRODYNE

NMR spectroscopy using the protocols introduced in the last part of the thesis can provide chemical information at the nanoscale, which may be of use in surface or interface chemistry and single protein biology applications. However, its linewidth is limited by the coherence time of the NV and sample diffusion, reducing the complexity of the chemical information provided, hence the elucidation of detailed molecular structures are of great challenge. This chapter will discuss an alternative sensing protocol — Quantum Heterodyne (Qdyne) — which can achieve high NMR spectral resolution without being bottlenecked by the NV coherence time, hence reducing the demand for investments towards diamond material engineering.

In recent years, publications have demonstrated the working principles of this protocol. Schmitt et al. and Boss et al. [21, 140] demonstrated this concept on a test signal in 2017 with sub-mHz spectral resolution. In 2018, Glenn et al. [60] were able to achieve proton NMR signal detection using Qdyne from pure ethyl formate. Their experiment resulted in a high-resolution NMR spectrum with a linewidth of 10 Hz, which is fine enough to detect key molecular information such as J-couplings. They have achieved a sensitivity of 25-75 $\mathrm{nT}/\sqrt{\mathrm{Hz}}$ under a static field of 88 mT and took 10 hours to measure a spectrum. Further developments, such as incorporation with hyperpolarisation techniques [6, 26] have boosted the concentration sensitivity and measurement time, and the sensitivity record at the time of thesis submission is $20\,\mathrm{pT}/\sqrt{\mathrm{Hz}}$ [3].

In this chapter, the goal is to capitalise on the recent advances in high-resolution NV-NMR spectroscopy and fabricate an NMR lab-on-a-chip device to monitor chemical reactions in real time and in situ. Such devices have the potential to offer dynamic information on reaction rates and intermediates, which are not available in conventional bulky NMR spectrometers, offering new insights in fields such as drug design. The working principles of Qdyne, design and implementation of the experimental setup, sensitivity and stability of the experiment, and the lab-on-a-chip design will be discussed.

5.1 CLASSICAL SIGNAL MIXING: HETERODYNE AND HOMODYNE

The heterodyne process is a signal manipulation tool used to alter the signal frequency from one band to another. In the classical sense, heterodyning is commonly used to mix the frequency of an incoming signal (f_1) with a local carrier frequency (f_2), resulting in two frequencies, $f_1 + f_2$ and $f_1 - f_2$. The high-frequency component is usually removed using a low-pass filter. This technique is commonly used in radio frequency receivers to downconvert the frequency of an incoming signal. However, this can also be used for optical signals in applications such as interferometry [22] and Qdyne.

It is worth noting that when $f_1 = f_2$, the process is transformed into a homodyne detection, where the signal after mixing and filtering is at DC. This is used to isolate information such as phase and intensity at f_1 from a noisy source and con-

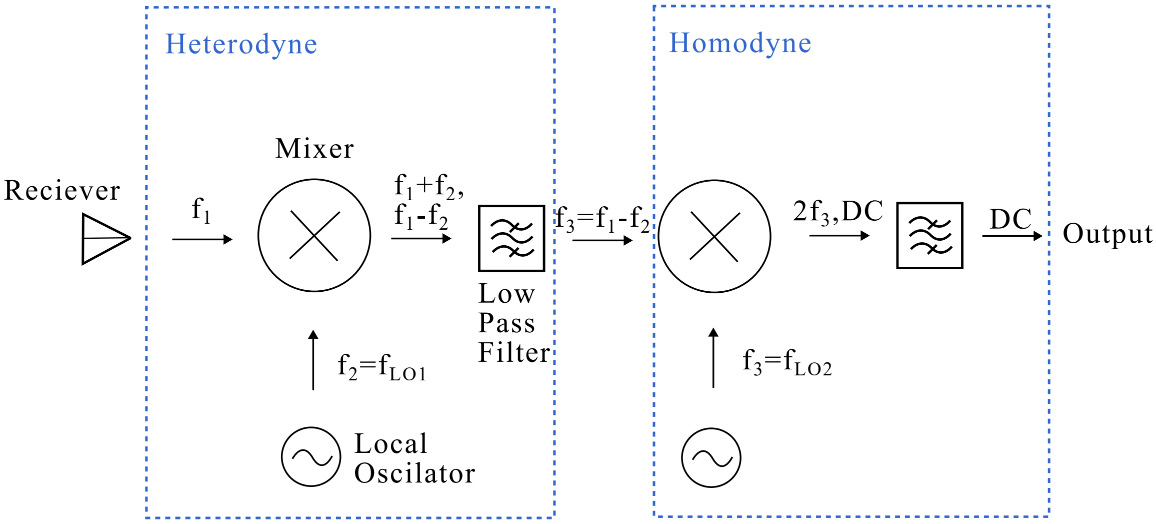

Figure 5.1: An illustration of the superheterodyne technique, which is a combination of heterodyne and homodyne manipulations. In heterodyne, a signal of interest at f_1 is received and mixed with a generated signal from a local oscillator at f_2, which produces two responses at $f_1 + f_2$ and $f_1 - f_2$. After filtering, the lower frequency is kept. In homodyne, the signal of interest is mixed with a signal with the same frequency and after low-pass filtering, a DC response is kept.

vert them to a static reading. This is also part of the working principle for a lock-in detector, where information at a certain frequency can be amplified as signals in other frequencies, or when out of phase after mixing and filtering, will become zero over a sufficient sampling time. The process of applying homodyne to a heterodyne signal is called superheterodyne, which is illustrated in figure 5.1.

5.2 WORKING PRINCIPLES OF QDYNE FOR NMR

In quantum metrology, the desired information is usually encoded in the phase of the qubit, which has an inherent dephasing time (~µs for room temperature NVs) that limits the spectral resolution of the information obtained. In quantum heterodyne, such encoding is performed to a source controlled by a classical oscillator (stability time of tens of seconds for standard oven-controlled crystal oscillators), thus improving the spectral resolution [140]. Compared to dynamical decoupling-based spectroscopic techniques discussed in previous chapters, the Qdyne protocol can achieve a significant gain in spectral linewidth by 6 to 9 orders of magnitude, as shown in figure 5.2. In this section, the details of Qdyne will be discussed.

For Qdyne NMR, the encoding of the signal of interest to a classical oscillator is a two-part process via an intermediate sensor, which is the NV centre. First, the clock needs to interact with the sensor. This is achieved by repeating a measurement at a fixed sampling rate and synchronising this repetition to the clock. This implies that the readout laser pulse is at a fixed duty cycle and the information-containing PL contrast is collected at the sampling rate. The second part involves the sensor detecting the signal of interest. The measurement protocol that is sensitive to the NMR band (~MHz) is the XY8-N sequence, where N=no. of π pulses/8. However, in order to maintain synchronicity with the local oscillator and achieve maximum sensitivity, the XY8-N sequence is performed with a fixed inter-pulse duration where the corresponding filtering frequency is at the NMR Larmor frequency.

In dynamical-decoupling sensing, the NV responds to an external signal by encoding information to its phase, limited by the dephasing time. In Qdyne, the NV responses are similar, but the information is treated differently. They are stored at each readout to computer memory with an associated error rate originating from the clock. However, unlike in deocher-

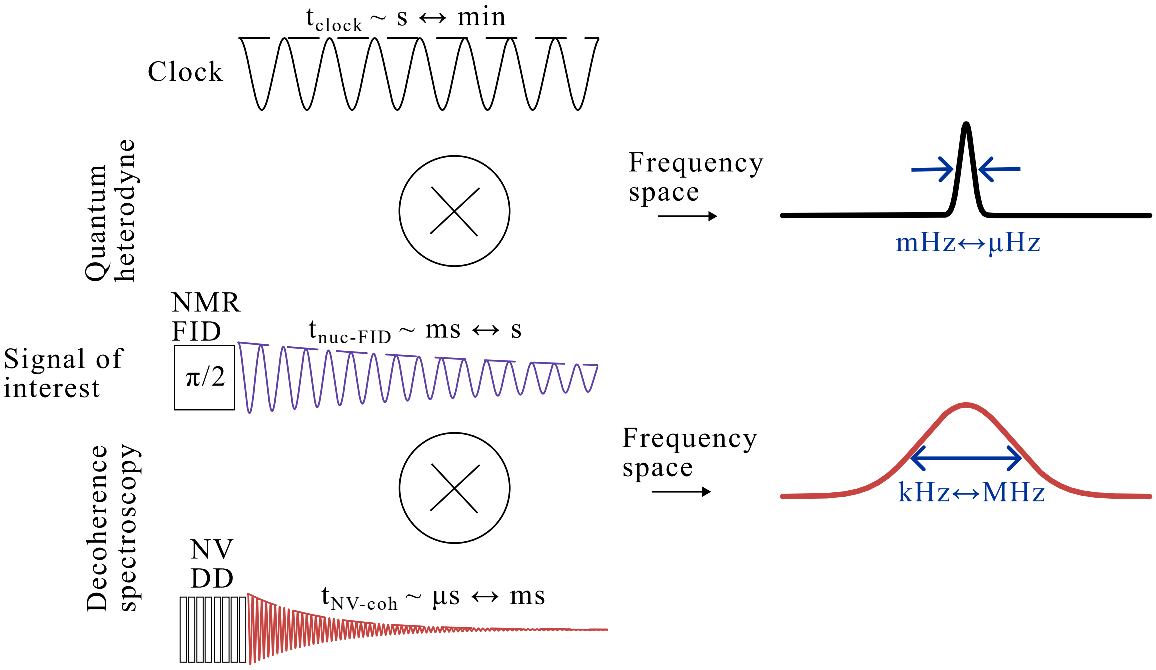

Figure 5.2: A comparison between the information encoding methods. The Qdyne linewidth improvement comes from the mixing of the signal of interest with an oscillator with much longer stability time in the form of a classical clock (seconds to minutes) instead of a quantum coherence time (μs - ms).

ence sensing, where the individual phase accumulations are compared against each other at different filter frequencies, in Qdyne, the phase information is stored and correlated at each readout pulse, making full use of the clock stability time.

From the NV perspective, consider an external NMR signal in the form of

$$B_{NMR}(t) = B_{NMR_0} \sin(\omega t + \phi), \tag{31}$$

where B_{NMR_0} is the amplitude of the oscillating magnetic field, $\omega = B_0 \gamma_{nuc}$ is the Larmor frequency and ϕ is the phase of the signal. If an XY8-N sequence is performed, the NV's accumulated phase is given by

$$\Phi = \gamma_{NV} \int_0^{\tau_{tot}} B_{NMR}(t)\mathcal{F}\{g(f_{XY8})\}\, dt, \tag{32}$$

where $\mathcal{F}\{g(f_{XY8})\}$ is the Fourier transform of the filter function for the protocol at the frequency of f_{XY8}, which for maximum sensitivity equates to ω. $f_{XY8} = 1/2\tau$ can be controlled by adjusting the interpulse space time τ. For N=1, τ=250 nm (total evolution time is 2 µs), f_{XY8}=2 MHz.

If a XY8-N sweep can be completed with infinitesimal time ($\tau_{tot} << 1/\omega$), then the resulting full spectrum will oscillate with respect to $B_{NMR}(t)$.

Due to the oscillatory nature of the external signal, if the XY8-N sequence is performed at a fixed frequency (f_{meas}), the accumulated coherence should also be oscillatory. Also, f_{meas} is usually at a few kSamples/s due to the overheads needed from the laser and microwaves (details see next section), and $\omega/2\pi$ is usually on the order of MHz. Due to this frequency mismatch, according to the Nyquist–Shannon sampling theorem, the undersampled signal in the form of accumulated phase would exhibit an aliased frequency of $f_{aliased} = |\omega - kf_{meas}|$, where k is an integer, shown in figure 5.3. A frequency spectrum can be obtained by performing a Fourier transform on Φ.

In Fourier space, the frequency resolution per bin is given by $f_{meas}/2N_{reps}$, where N_{reps} is the length of the measurements. For NMR spectroscopy, in order to extract chemical information, the Fourier bin width needs to be ~ sub-Hz. As a consequence, N_{reps}~10^3, which implies in order to reach meaningful spectral resolution, the measurement needs to be at least a few seconds, otherwise the frequency bin will not be small enough to fully capture the spectral information, reducing spectral accuracy. This is also the speed limit of an NMR measurement unless a fast sampling rate can be achieved.

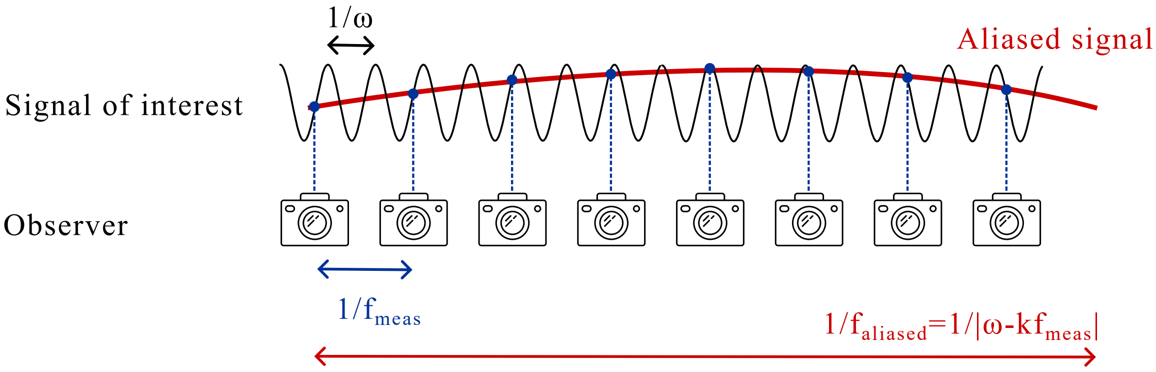

Figure 5.3: A demonstration of the Shannon-Nyquist sampling theorem. When sampling an oscillatory signal of frequency ω at a fixed rate (f_{meas}), the output signal will also be oscillatory. When undersampling occurs ($2f_{meas} < \omega$), an aliased frequency ($f_{aliased}$) is measured and the true frequency ω cannot be uniquely obtained.

Due to the undersampling of $B_{NMR}(t)$, the exact value of ω cannot be obtained uniquely, as a singular aliased frequency can originate from different incoming signals. However, for NMR applications, where information is in the form of a relative frequency shift to a standard, the exact value of k is not important. If the exact value of ω is deemed necessary for applications such as AC magnetometry, other broadband quantum sensing protocol such as ODMR, can be used in conjunction to estimate k or consider the use of multidimensional sampling methods.

5.3 IMPLEMENTING QDYNE FOR NV-NMR

The key technical challenge for Qdyne NMR experiments compared to the NV NMR protocols detailed in previous chapters is timing. As outlined in the previous section, Qdyne measurements need to satisfy the following:

- perform NMR sensitive measurement at a fixed sampling rate,
- readout, transfer, and store PL information after each measurement,
- synchronise all electronic timing elements.

This section will consider the key technical details needed in order to fulfill the above-listed requirements.

In conventional NV experiments, the setup is usually built at two extremes. On one end, a widefield sCMOS camera setup that has a large active area (~cm^2) with high saturation limit (~10^9 photons per ms) is used, but its refresh rate is usually limited to 100 frames per s. The other extreme uses a confocal scanning system, usually equipped with a single-photon avalanche diode and a time correlated single photon counter that can measure fast information (~GHz), but it comes with a small active area (~μm^2) and low saturation limit (~10^3 photons per ms). For Qdyne measurements, the optimal configuration requires the features from both extremes. A fast detector (~ MHz) is needed to satisfy the timing requirement. Also, due to the fact that every laser pulse is collected and considered, collecting as many photons as possible per shot is desired, hence requiring a high saturation and large active area detector.

Due to the fact that the coherence time no longer sets the linewidth limit of the spectrometer, the strategy for NV diamond material is now focused on increasing the NV density for improved PL emission rate instead of minimising inherent local spin bath noise from the substitutional nitrogen defects. Hence, a single crystal quantum-grade diamond substrate (Thorlabs DNVB14) with a reported NV density of 4.5 ppm throughout the substrate is used for the NV-Qdyne-NMR spectrometer. However, due to the fact that a higher number of NVs require enormous laser and MW power and the deep NVs do not contribute to the NMR sensing near the surface of the diamond (for details, see next section), the purchased substrate is then sliced and polished to a 50 µm membrane by Applied Diamond. Although the Qdyne-NMR linewidth is not limited by the NV coherence time, the sample still needs to process a minimum level of room temperature coherence of a few µs in order to detect NMR active species.

The diamond membrane (20×20×0.05 mm) is placed onto a glass cover-slip (0.1 mm thickness), which is in turn glued onto a printable circuit board (PCB). The PCB is attached to a set of translational stages that allow fine movement adjustments for the NVs during optical alignment. A 532 nm laser (Laser Quantum opus 532) is used for optical excitation of the NVs. It is operating at maximum power of 2 W and water-cooled using a chiller for stability. The laser is passed through an AOM (G&H Photonics I-M110-2C10B6-3-GH26) that allows a controlled redirection of the laser beam path on and off the diamond by gating the 110 MHz RF signal originating from the AOM driver (G&H Photonics 110-AFP-AD-5.0). The modulated beam is focused onto the diamond surface (20 µm diameter) using an aspheric lens (Thorlabs ACL25416U, f=16 mm, NA=0.79) and the laser power is 200 mW at the diamond. The same lens is then used to collect the PL and filtered through a dichroic (Thorlabs DMSP567R, shortpass cutoff=567 nm) and a longpass filter (FELH0650, cutoff=650 nm) and focused onto the photodetector using an achromatic lens (Thorlabs AC254-035-B, f=35./mm).

The NV-Qdyne-NMR spectrometer uses a silicon amplified detector (Thorlabs PDA36A2, 30 dB gain, 260 kHz bandwidth) to collect the photo-response of the NV. Due to the high refractive index ($n_{\text{diamond}} = 2.41$) of the diamond, efficient collection of the PL, especially for an NV ensemble, is challenging. Hence, the choice of this particular detector is to help with this issue as it has a large active area of 13 mm^2. The PL is then digitised using an analogue-to-digital (ADC) converter (National Instruments PCIe-6321, 2 MSamples/s). At this bandwidth, this photodetector/ADC combination can collect PL data points every 500 ns, which is sufficient to collect a few data points per laser pulse without significant distortions. However, this sampling rate and bandwidth can be improved for a more detailed examination of the PL response. This usually comes with a cost of lower detector gain, smaller active area, and a higher sampling rate ADC. For the present setup, the detection bandwidth is sacrificed for SNR. This is also justified by the fact that the PL response is already slower than single NV experiments from previous chapters due to the high-density NV diamond sample (low excitation rate) used and slow charge state cycling dynamics.

High NV density is also a cause for the charge state instability.

Microwaves (MW) are used to manipulate the NV spin states and generated using a vector signal generator (Rohde & Schwarz SMBV100A) and amplified using a high power amplifier (Mini-Circuits HPA-50W-63+). The MW generated can exhibit a phase difference of 90 degrees needed for the X and Y pulses in the XY8-N sequence, using the onboard I/Q modulators. They are delivered using an custom fabricated omega-shaped gold antenna (shown in figure 5.11) deposited onto a microscope coverslip that is in direct contact with the diamond. Radio frequency waves (RF) are also used to manipulate the target nuclear spin states using a dual-channel waveform generator (RIGOL DG4162).

The RF is combined with the MW using a diplexer. To protect the electronics, an attenuator (Mini-Circuits VAT-30W2+, 30 dB attenuation) and terminator (50 Ω) are placed after the antenna to remove excess energy, and a circulator is used after the amplifiers to prevent reflection damage. In order to manipulate and trigger the instruments (AOM driver, ADC, MW/RF generators), Transistor-Transistor-Logic (TTL) signals are generated using a programmable pulse generator (SpinCore PBESR-PRO-500-PCIe PulseBlaster).

To synchronise all the electronic timing controls under one clock source, the internal 10 MHz reference output of the vector generator is used as the master clock (frequency error rate 100 ppb). This clock signal is then phase-locked to the ADC and the waveform generator. The sync output second channel of the now synchronised waveform generator is then used to produce a 50 MHz square wave (from 0 to 3.3 V), which is connected to the PulseBlaster as it does not support the 10 MHz signal as the reference source. The synchronisation of the PulseBlaster requires the removal of its own onboard oven-controlled oscillator and soldering the 50 MHz square signal into the pin inputs as shown in figure 5.11. The overall setup, including optical and electrical diagrams are shown in figure 5.4, and photos are shown in figure 5.11.

It is worth noting that the PulseBlaster output may be used as the master clock as the generators and DAQ support 10 MHz TTL signals as the external reference. However, the pulse blaster does not allow the programming of independent channels. The instructions for the output of all the channels (including the triggers for the MW and RF) need to be defined as a whole. This complicates the programming process, because the duty

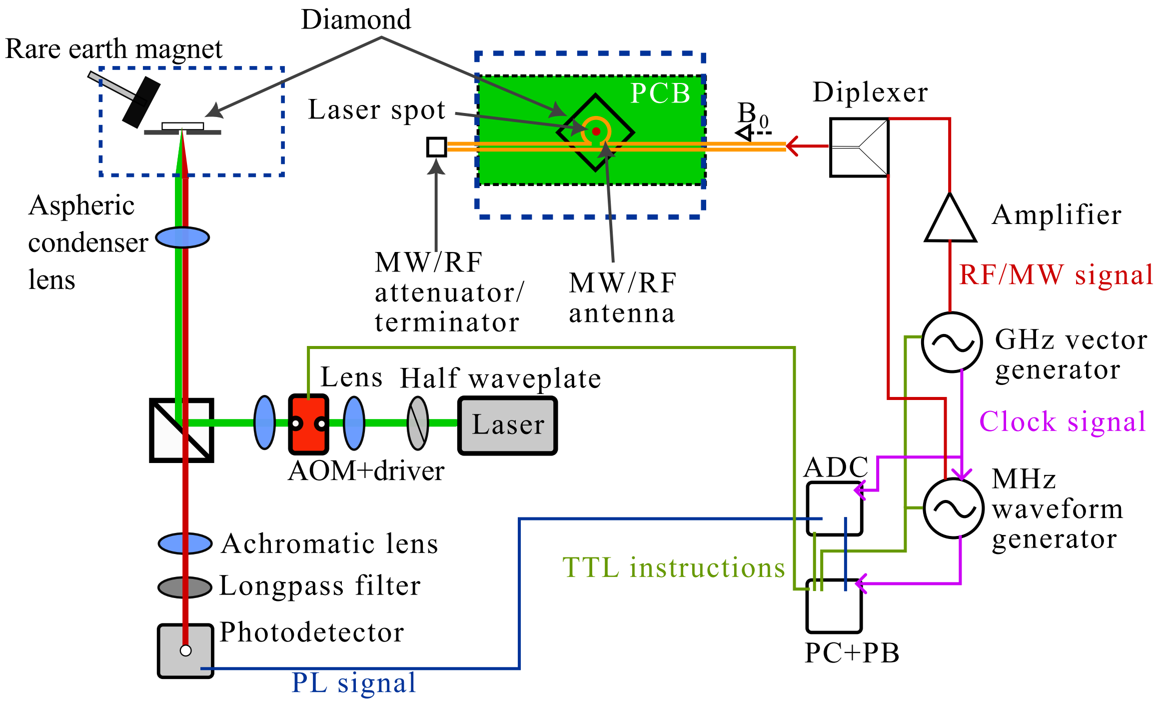

Figure 5.4: A schematic of the experimental implementation of the Qdyne protocol. The laser's polarisation is manipulated using a half-wave plate for efficient coupling to the NVs aligned with the magnetic field. Then it is pulsed using an AOM and focused on the diamond surface using a condenser lens. The laser spot is 20 μm in diameter. The subsequent PL is collected using the condenser lens, focused on a photoreceptor using an achromatic lens, and filtered through a dichroic mirror and a long-pass filter. The electrical control instructions originate from a programmed PulserBlaster (PB) and are sent to the AOM driver, signal generators, and the ADC. The clocking signals ensure timing synchronicity between the ADC, PulseBlaster, and the generator. The master clock signal is generated by the vector generator. The amplified MW and RF pulses are combined using a diplexer and delivered on the PCB with an antenna that is placed directly under the diamond. The excess RF/MW is attenuated and terminated using a 50 Ω terminator. The magnetic field is aligned at 54.7 ° to the diamond normal.

cycle rate of the Qdyne measurement needs to be an exact integer divisible by 10 MHz. If not, the subsequent instruction set as a whole will be different from the previous; the repeat feature cannot be utilised. This factor, along with the use of nested loops, complicates the programming step and introduces additional on-board memory use, which is limited to 4096 instructions. As a consequence, additional dead time needs to be introduced, but this limits the control flexibility, hence this approach is not adopted. However, the use of highly customisable TTL sources such as the Red Pitaya STEMlab series may overcome this issue.

Instead of hardware clock synchroisation, one may consider manually adjusting the individual onboard clocks, so all of them tick at the same rate. However, not all instruments support clock dividers/multipliers, and they need to be recalibrated because most clocks are sensitive to temperature effects. Therefore, the most convenient method is to use one master clock.

Equipped with an understanding of the hardware components of the spectrometer, the software controls will be discussed next. The system uses the LabVIEW software as a centralised controller, which communicates via the virtual instrument software architecture resources to the vector generator and ADC to set predefined tasks, including MW frequency and power, ADC clock source, input and trigger channel, sampling rate, and length. The software also predefines timing-sensitive tasks using the PulseBlaster's application programming interface. These instructions, in turn acts as triggers and gating instructions for the generators, AOM driver, and ADC. The settings on the RF waveform generator are defined manually, and the RF output is set to gated mode, which enables control via TTL.

Prior to performing NMR spectroscopy, ODMR and Rabi experiments are required to measure the NV resonance frequency and MW π pulse duration. For Qdyne-NMR, the PulseBlaster's timing train is defined in the following order and illustrated in figure 5.5:

1. wait time (1 s) to allow for the loading of other predefined instructions,
2. polarisation laser (5 s) to initialise all the NV spins prior to MW manipulation,
3. RF $\pi/2$ pulse (~µs) to begin the nuclear FID process,
4. ADC trigger to begin acquisition,
5. MW XY8-N sequence (including X and Y pulses with empty instructions for NV spin evolution; the duration of evolution defines f_{XY8}~ MHz and the usual NV π time is around 60 ns),
6. readout laser pulse (500 µs)
7. a wait time (1.5 µs) to allow for the NVs to relax back to the ground state
8. an additional wait time to account for the finite acquisition rate of the ADC, so the total duration of this and the previous three steps is equal to an integer multiple of 500 ns (or the inverse of the ADC sampling rate), and
9. repeat the previous four steps for N_{reps} times.

The PL information is then processed by dividing the signal part of the pulse (defined to be the sum of the photodetector voltage at from 1 to 51 µs), by a reference part of the pulse (from 401 to 451 µs). The information is then Fourier transformed to form a spectrum. The sampling rate used was the inverse of the

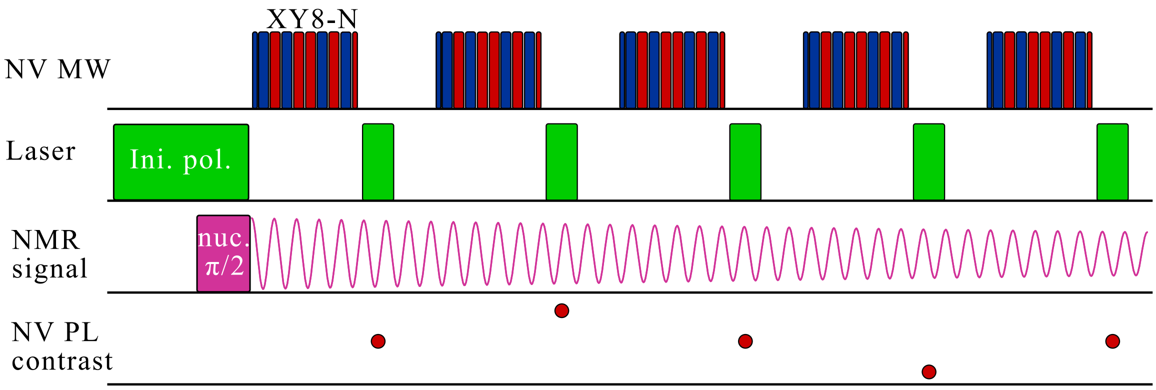

Figure 5.5: Pulse sequence of the Qdyne protocol. A polarisation laser pulse (5 s) is used to initialise the NV spins. Towards the end of the pulse, the nuclear $\pi/2$ pulse (~ ms) is used to begin the free induction decay process of the target spins. The NVs are then used to measure the Lamor frequency by repeating the MHz sensitive XY8-N MW protocol (blue for X and red for Y), which are in turn read out using 500 µs laser pulses, and the PL contrast should exhibit a frequency response at $f_{aliased}$.

total time used in step 5 to 8. An example Qdyne spectrum is shown in figure 5.6.

Due to the long rearming or dead time (~1-100 ms, depending on the software) of the NI DAQ used, it was not feasible to trigger acquisition at each readout laser pulse, so only one trigger at the very start of the experiment is applied. During post-processing, a procedure needs to be developed to account for information when the laser is on and off, so only relevant PL information can be extracted. An additional wait time (step 8) is used to ensure that the acquisition window is at the same part of the laser pulse for all N_{reps} and it is not drifting away.

If clock synchronisation is not in place and due to the fact that retriggering of the laser pulse is unavailable, any errors from clock mismatch will be accumulated, and this is shown in figure 5.7 as a drift, because the collection windows are moving.

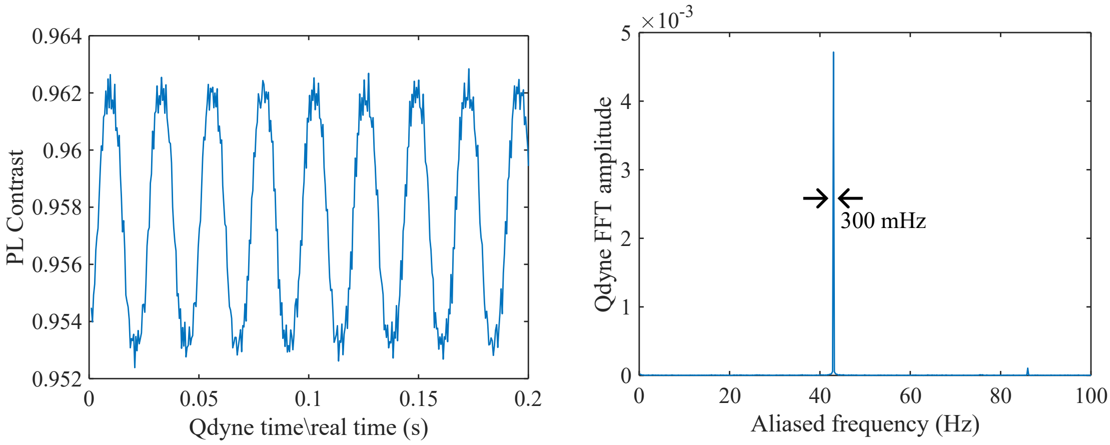

Figure 5.6: A typical Qdyne measurement on an external AC signal at 1.000043 MHz. f_{XY8} =1 MHz, N=1 (8 π pulses), f_{meas}=1.96 KHz, $f_{aliased}$=43 Hz and N_{reps} = 10000. **Left** shows a portion of the PL contrast change during this Qdyne measurement. It exhibits an oscillatory behavior at $f_{aliased}$. **Right** shows a Fourier transform of the total measurement confirming $f_{aliased}$ and demonstrating the high spectral resolution of Qdyne at 300 mHz.

Hence, demonstrating the importance of clock synchronisation for Qdyne.

The use of this particular ADC for direct Qdyne measurements is investigated in a later section.

To investigate the optimal readout laser pulse duration and integration window, a higher sampling rate ADC (Gage RazorMax 16-Bit PCIe Digitizer, 1 GSamples/s) was used to investigate the dynamics below 500 ns. The PL response under a laser pulse was measured and shown in figure 5.8. It was clear for this setup, there is spin-dependent PL information after 50 µs of illumination, and it can take up to 500 µs to repolarise the NV spins. In addition, a longer feature at 300 ms was detected; this is tentatively attributed to the charge cycling of the NV. This investigation shows that the readout protocol requires a long laser pulse (up to 500 µs) and significant spin-dependent PL change can be observed at up to 50 µs, which defines the signal integration window. There is also an electrical artefact near

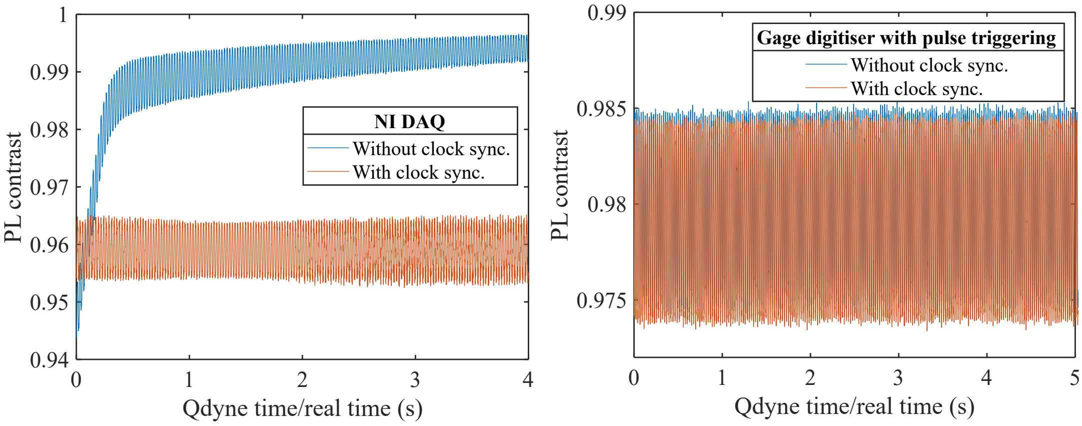

Figure 5.7: Qdyne responses using different ADCs and with and without clock synchronisation. **Left** shows that using the slower NI DAQ, without clock synchronisation, the PL contrast will drift as a consequence of the sampling window drifting out of the laser pulse, which in turn can broaden the frequency linewidth. Hence, demonstrating the importance of clock synchrosation. **Right** shows that using the faster digitiser, which supports fast triggering, this issue no longer exists as synchronisation can be achieved with fast triggering.

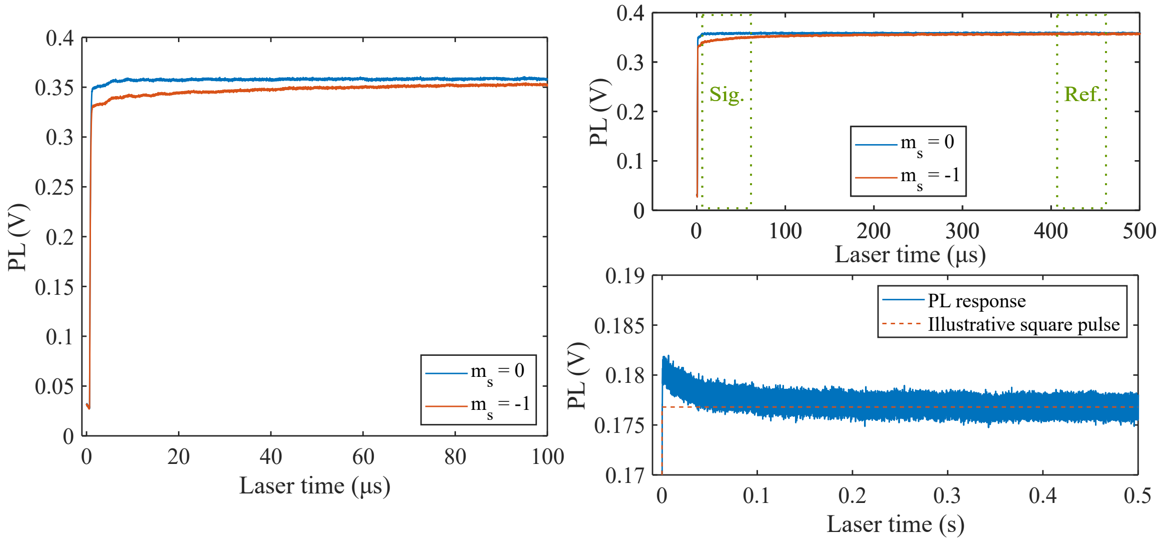

Figure 5.8: Transient PL measurements of the NV diamond sample used in this chapter. **Left** shows the spin state dependent PL transients below 100 µs and **Top Right** shows the same information up to 500 µs. These two panels suggest that the PL response is significantly slower compared to previous chapters due to the use of a high-density NV diamond. Hence, at this laser power density, the integration window should be extended to at least 50 µs, and the laser pulse needs to be at 500 µs for repolarisation. **Bottom Right** also shows that this dense NV sample exhibits slower charge cycling dynamics up to 300 ms.

1 µs. This is attributed to the use of the digitiser, but to be safe, while using the NI DAQ, PL information below 1 µs is also not processed.

Any slow (longer than 1 ms) effects that change the PL response can be mitigated by self-referencing the integration window of the signal to a similar window at the end of the readout pulse, where there is no spin information. To investigate these, the self-referencing is turned off. Figure 5.9 shows the Qdyne PL contrast drifting with different lengths of initial laser time. The nature of this drift is systematic, which suggests that the more random laser intensity drift is not a dominant effect. This

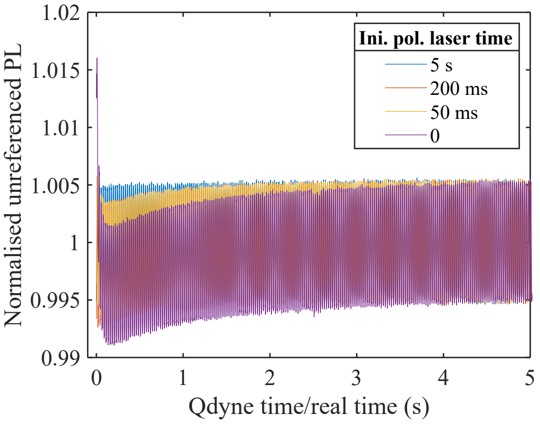

Figure 5.9: Qdyne measurements without self-referencing under different initial polarisation laser pulses. When the laser pulse is short, a drift can be observed, suggesting that the NVs are not completely initialised at the start of the Qdyne sequence and are slowly stabilising during the protocol through the readout lasers. To avoid this effect, the initial polarisation pulse should be at least 5 s long for this laser power density and sample.

drift is attributed to insufficient initial polarisation, because this unwanted drift becomes less significant as laser time increases. A similar effect can also be measured due to charge state cycling. To confirm the charge state dynamics, the use of orange and red illumination sources should be implemented.

Although the drift and the drift related broadening are not observed when self referencing is employed; from this investigation, the fact that a short initial pulse can result in improper initialisation suggests that without a long laser pulse, the measurement in the first few seconds can be less sensitive as not all of the NVs are maximum contributing to PL that relates to its spin state. Hence, the need for a long initial polarisation pulse (5 s) is important for a high-density sample.

The electronic artefacts, such as bandwidth distortions, can also contribute.

Another important parameter relating to Qdyne is the number of π pulses during one XY8-N sequence, and it is explored in figure 5.10. Using external signals at a fixed power, the Qdyne responses are measured using different N. Using 2.000043 MHz (f_{XY8}=2 MHz), it was found that as N increase the Qdyne amplitude also increases up to N=5, this is consistent with the fact that the change in NV contrast due to an external effect increases as N increases up to a point where the overall contrast drops due to additional decoherence during the extra MW and dephasing times. This contrast drop is more prominent when sensing at lower frequencies, as the NV requires a longer evolution time to reach the lower f_{XY8}, which exposes to more decoherence sources. This is also shown in figure 5.10, where the f_{XY8} at 1 MHz was used to measure an external signal of 1.000043 MHz, showing only the reduction trend due to increased decoherence as a result of the longer τ times. This investigation demonstrates that N can affect Qdyne sensitivity as it alters the PL contrast and the extent of such effect changes at different frequencies, hence it shows the need to calibrate for N to maximise SNR when operating at a different f_{XY8}, either from a change in B_0 or a change in element in NMR spectroscopy. Compared to decoherence-based NMR measurements showcased in chapter 3, where increasing N improves the spectral linewidth at a cost of SNR (explained in section 4.4), in Qdyne, the spectral linewidth is not affected by N, only the SNR.

It was also observed that $f_{aliased}$ changes with N. This is caused by the slight change of the sampling time as more π pulses and evolution time are added, hence affecting f_{meas} and f_{alised}. Also, the finite pulse duration of the PulseBlaster (resolution at 2 ns) can also contribute. There are special cases when this change does not occur, because the total pulse duration per N_{rep} is already at integer multiples of 500 ns in order to synchronize the DAQ.

5.4 STATISTICAL AND THERMAL POLARISATION OF NUCLEAR SPINS

The previous section detailed the technical specifications with respect to the control electronics and justified some of the instrumentation decisions. This section will explore the external factors that affect the spectrometer, especially around the thickness of the NV layer in the diamond.

The sensing volume of the detector is dictated by the depth of the NV. Spins closer to the surface will mostly interact with targets in its vicinity, while deeper spins experiences wider field of view. To maximise one of the NV-NMR advantages of reduced stand-off distance, one may initially consider creating a shallow layer of NVs nanometres away from the target. However, at this scale, the nuclei exhibit statistical polarisation behaviour that inhibits the Qdyne advantage [144].

Statistical polarisation occurs when the sensing volume reduces to the nanometre scale, and the spin noise dominates the mean thermal polarisations. In this regime, due to the low total number of spins, the total magnetic moment is not averaged effectively due to the fluctuations, and the Boltzmann description of the spin distribution is not observed. As a consequence, the statically polarised signals exhibit a fluctuating phase, and it cannot be easily incorporated into the Qdyne protocol, which relies on the signal to exhibit a stable phase during measurement. This is illustrated in figure 5.12. Also, in this regime, the spins no longer need a $\pi/2$ pulse to begin precession.

Diffusion is also a major challenge, which was discussed in the last chapter.

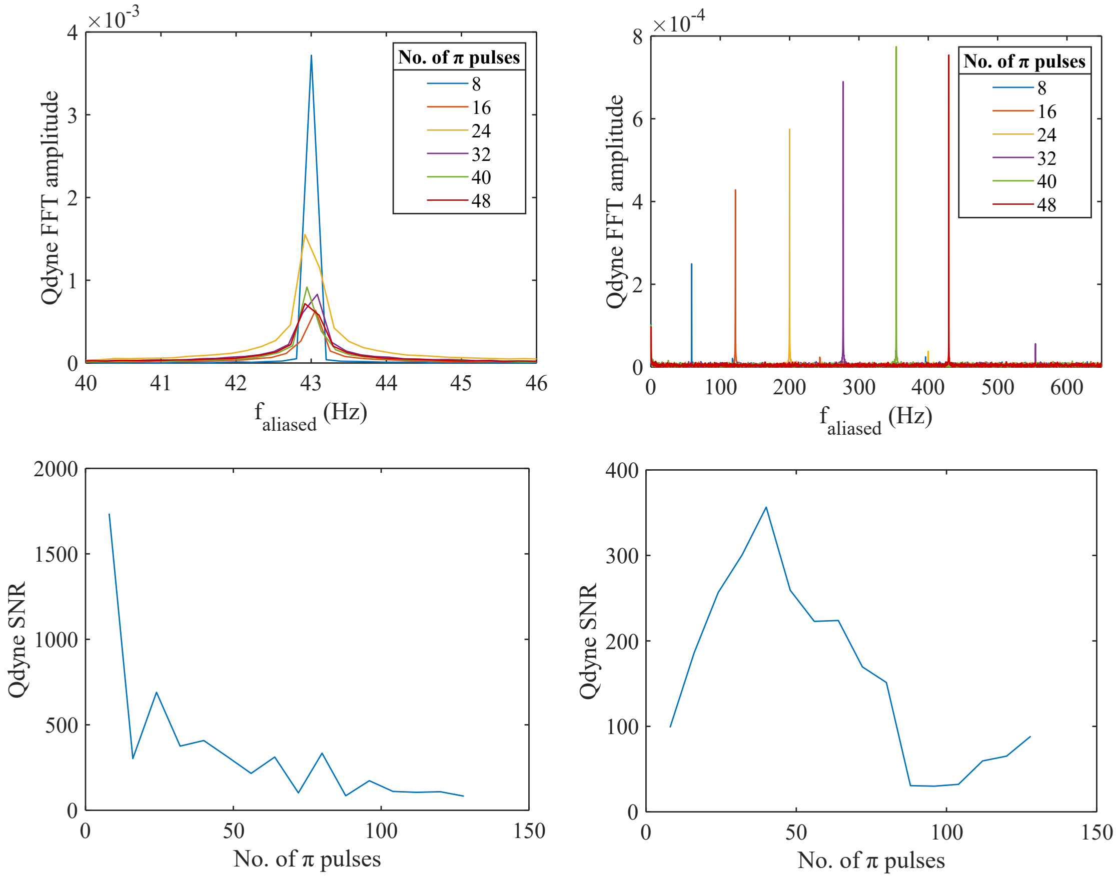

Figure 5.10: An investigation of Qdyne contrast at different N using an external signal with fixed power at f_{XY8}=1 MHz for **Top Left** and 2 MHz for **Top Right**. **Bottom Left** and **Bottom Right** show the overall trend for f_{XY8}=1 MHz and 2 MHz, respectively. The observations show that there is an upward trend where SNR increases with N due to increased PL contrast change from an external signal, and a downward trend where the extra evolution time introduced from high N causes extra decoherence and loss in overall contrast. Both trends are observed in **Right**, but only the downward trend is observed in **Left** due to the low f_{XY8}, and it already has a long evolution time at N=1. **Right** also exhibits a change in f_{alised} due to the finite pulse length changing the f_{meas} at different N. The lower SNR from the 2 MHz Qdyne results compared to 1 MHz is attributed to the RF coils, which were not engineered to deliver uniform power across different frequencies.

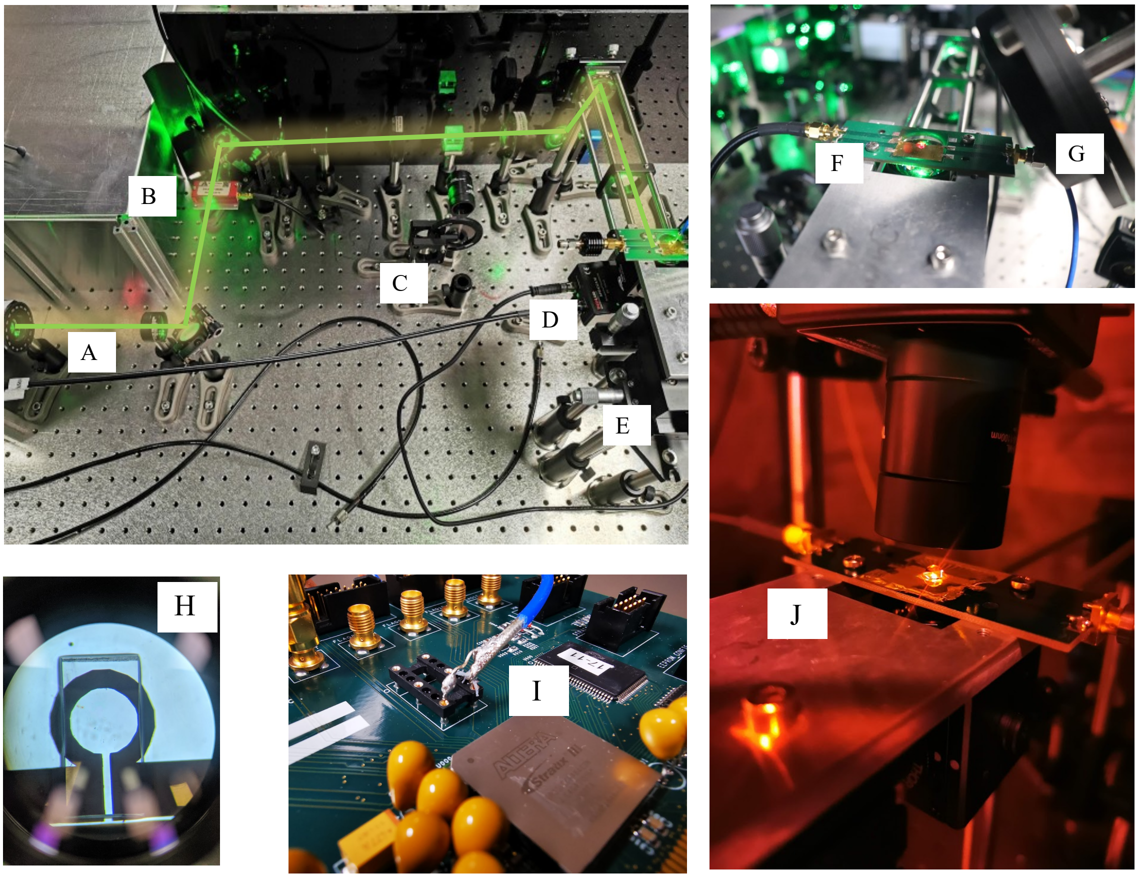

Figure 5.11: A collection of photos of the apparatus. **Top Left** shows an overview of the system. **A** represents the laser path. **B** is an example of an AOM. **C** is reserved for a balanced detection to reduce laser noise. **D** is the photo detector that is placed under the diamond. **E** is the set of translational stages for position adjustments. **Top Right** shows a close-up photo. **F** is the PCB and **G** is the permanent magnet used. **H** shows a photo of the omega-shaped antenna placed below a diamond sample (4×0.5 mm). Note that this sample is only for illustrative purposes, as it is transparent, unlike the high-density samples used for Qdyne. **I** shows the clock port of the Pulse-Blaster and the external clock connection. **J** is an alternative collection setup from above the diamond using a half-ball lens on the diamond.

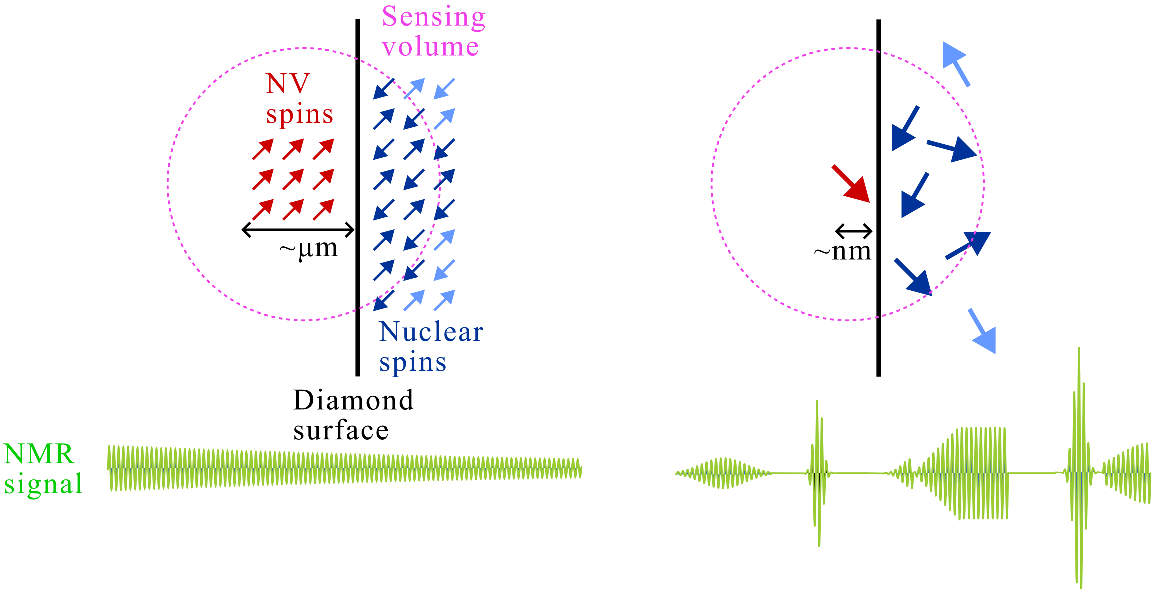

Figure 5.12: A comparison between sensing thermally polarised spins using NVs (red) micrometre away and statistically polarised spins nanometre away. **Left** shows that within the μm scale sensing volume, the detected spins (dark blue) are either aligned or anti-aligned according to Boltzmann's distribution. Hence, the resulting NMR signal has a steady phase, but a lower amplitude due to increased standoff distance. **Right** shows that the nm scale contributing targets are dominated by spin noise. Although the signal strength is stronger, it has a stochastic phase and amplitude, which Qdyne finds difficult to measure.

The advantage is that at this scale, the statistical polarisation can reach a few percent, which requires a significant magnetic field to reach in a Boltzmann distributed sample. This is due to the fact that the measurement detects the variance of the magnetisation instead of the mean, which is zero. For an ensemble of N nuclear spins with I quantum number, the magnetisation in the direction of the static magnetic field (B_0) and its standard deviation are given by

$$M = N\frac{I(I+1)}{3}\hbar\gamma_{nuc}(\frac{\hbar\gamma_{nuc}B_0}{k_B T}) \text{ and} \tag{33}$$

$$\sigma_{M_z} = \sqrt{N\frac{I(I+1)}{3}}\hbar\gamma_{nuc}, \tag{34}$$

which are derived by Xue et al. [172] using statistical mechanics. The thermal and statistical polarisations are then given by

$$P_{thermal} = \frac{M_z}{M_{100\%}} = \frac{I+1}{3}\frac{\hbar\gamma_{nuc}B_0}{k_B T} \text{ and} \tag{35}$$

$$P_{statistical} = \frac{\sigma_{M_z}}{M_{100\%}} = \sqrt{\frac{I+1}{3IN}}, \tag{36}$$

where $M_{100\%} = N\hbar\gamma_{nuc}I$ correspond to full spin polarisation. Because the magnetisation scales with N and the variance scales with $\sqrt{N}$, there exists a critical number where the crossover between the two effects occurs, which is given by

$$N_c = \frac{3}{I(I+1)}(\frac{k_B T}{\hbar\gamma_{nuc}B_0})^2 \tag{37}$$

and for protons in water at 300 K and 20 mT, $N_c = 8.5 \times 10^{15}$, which corresponds to a critical volume of 1.3×10^5 µm^3, and if it is for a hemisphere, the radius is 40 μm. The behaviour of proton magnetisation and polarisation are exampled in figure 5.13. Due to the fact that N_c also depends on B_0, an increase in the static field can have a two-fold effect on the Qdyne protocol. First, it boosts the magnetisation of the sample. Second, it reduces N_c, which can be leveraged to reduce the sensing volume and increase sensitivity (scales $1/r^3$, see next section) at the cost of reduced M. However, as a caveat, at high B_0, the NV is more negatively affected by B_0 misalignment, and the absolute field uniformity also suffers.

The variance of the magnetisation no longer depends on T and B_0, hence suggesting that at the nanoscale, the NMR signal can be comparable to the thermally polarised spins under a high B_0. However, due to the stochastic nature of the signal phase, despite its advantage in signal amplitude, high-resolution NMR using Qdyne is not trivial, and future work towards this direction is discussed in the next chapter. Consequently, the sensing volume needs to be above the critical number, which suggests a tens of microns thick NV layer and laser spot size. However, the sensing volume should not exceed the crossover point significantly, as this will introduce more NVs, which require higher laser powers; and spatial variations in MW and magnetic fields, which cause errors in the NV control and variations in the target Larmor frequency. These complications will be discussed in the following sections.

5.5 SENSITIVITY OF DETECTION

Due to the complication with statistical polarisation and nanometre-scale microfluidics systems being hard to fabricate, the spec-

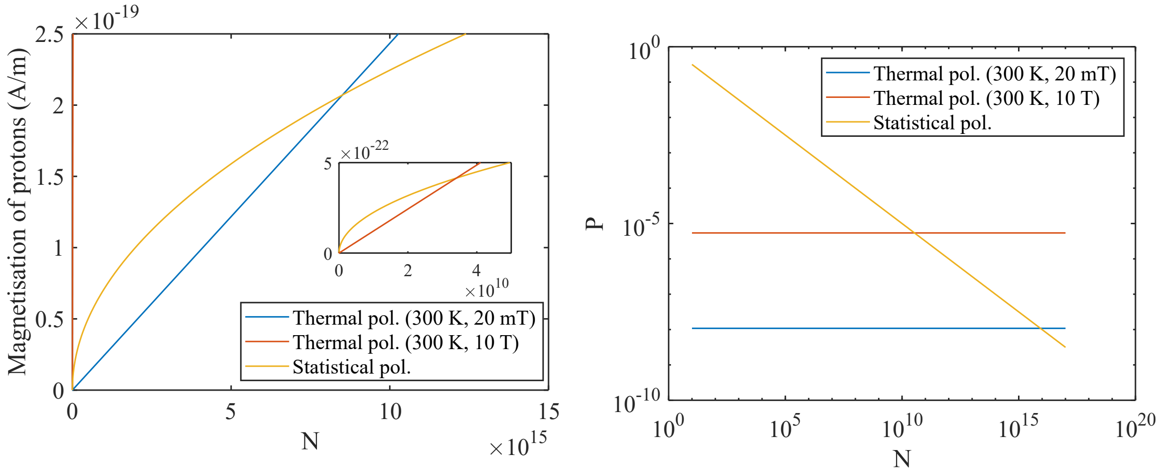

Figure 5.13: **Left** shows the magnetisation of protons at different N and B_0. N_c occurs when the statistical magnetisation (scales $\sqrt{N}$) intercepts with thermal polarisation (scales N). **Left Inset** shows a rescaled comparison for a thermally polarised sample at 10 T. **Right** shows the scaling of polarisation for thermal (20 mT and 10 T) and statistical samples. For $N < N_c$, statistical polarisation dominates and can reach a relatively high percentage. For the thermally polarised samples, this high percentage can only be accessed by a very significant B_0. In the context of Qdyne, thermal samples are needed, suggesting the use of either higher volume or higher B_0, which decreases N_c.

trometer will now work at µm standoff distance, which is relatively less sensitive to surface targets compared to nanoscale NMR experiments, for example. This section will explore the sensitivity requirement for the spectrometer in order to detect real spins.

First, the magnetic field caused by the external spins is calculated. For a single precessing spin, the magnet field at **r** is given by

$$\mathbf{B}(\mathbf{r}) = \frac{\mu_0}{4\pi}\frac{3\hat{r}(\hat{r}\cdot\mathbf{m}) - \mathbf{m}}{r^3}, \tag{38}$$

where μ_0 is the magnetic permeability and **m** is the magnetic moment of the precession, which is oscillatory in time at the Larmor frequency and perpendicular to the magnetic field direction. For Qdyne NMR, only the components in the direction of the background field ($\hat{\mu}_{NV}$) are sensitive to the NV centre, the total magnetic signal in a sensing volume of V, experienced by an NV at **r** is given by

$$\mathbf{B}\cdot\hat{\mu}_{NV} = \frac{\mu_0\rho}{4\pi}\int_V \frac{3(\hat{r}\cdot\mathbf{m})(\hat{r}\cdot\hat{\mu}_{NV}) - (\mathbf{m}\cdot\hat{\mu}_{NV})}{r^3}dV, \tag{39}$$

where ρ is the density of protons contributing to the Larmor precession in the sensing volume, for thermally polarised protons, it is given by

$$\rho = \gamma_{nuc}\rho_{tot}(1 - \exp(\frac{-2\gamma_{nuc}B_0}{k_B T})), \tag{40}$$

where ρ_{tot} is the total number density of the target.

This integral can be split into a dimensionless integral (G) that depends on the geometry of the sensing volume, given by

$$G = \int_V \frac{3(\hat{r}\cdot\hat{m})(\hat{r}\cdot\hat{\mu}_{NV}) - (\hat{m}\cdot\hat{\mu}_{NV})}{r^3} dV \tag{41}$$

and a prefactor (K) in units of magnetic fields, given by

$$K = \frac{\mu_0 \gamma \rho}{4\pi}. \tag{42}$$

In order to evaluate G, the z-axis is defined to be perpendicular to the diamond surface. If the magnetic field is aligned with NV and it is in the <100> crystallographic orientation, then $\hat{\mu}_{NV} = (\sqrt{\frac{2}{3}}, 0, \frac{1}{\sqrt{3}})$, $\hat{m} = \cos(\omega t)(\frac{1}{\sqrt{3}}, 0, -\sqrt{\frac{2}{3}}) + \sin(\omega t)(0, 1, 0)$ and $\hat{m}\cdot\hat{\mu}_{NV} = 0$ due to them being orthogonal. If the NV centre is at d_{NV} beneath the surface, then $\mathbf{r} = (x, y, z + d_{NV})$. For a hemispherical sensing volume with radius r_{hemi} and $d_{NV} = 50\ \mu\text{m}$, $G_{peak} = 0.7$. As $r_{hemi}/d_{NV} \to \infty$, it seems that $G_{peak} \to 2\pi \sin(\alpha)\cos(\alpha)$ as shown in figure 5.14, where $\alpha = 54.74°$ is the angle between the NV and the diamond surface. G_{peak} is also computed for the rectangular cuboid geometry, which can represent a microfluidic channel with depth h_{cuboid} fabricated above the diamond surface. The results, as shown in figure 5.14, suggest that G is larger for tall structures with high aspect ratios (high in z and low in x and y), which is insightful for microfluidic channel design.

Solution for G in a hemisphere volume have been confirmed analytically in reference [24].

When computing for other NV orientations (<111> and <110>), it was found that G = 0. This is caused by the quadrupolar symmetry in G's spatial distribution for dipolar couplings as shown in figure 5.15. Any symmetrical sensing volume in these configurations will not yield any NMR signals; only <100> samples are used for this chapter.

NVs 45° to the surface yield the highest G, but this cut angle is difficult to achieve.

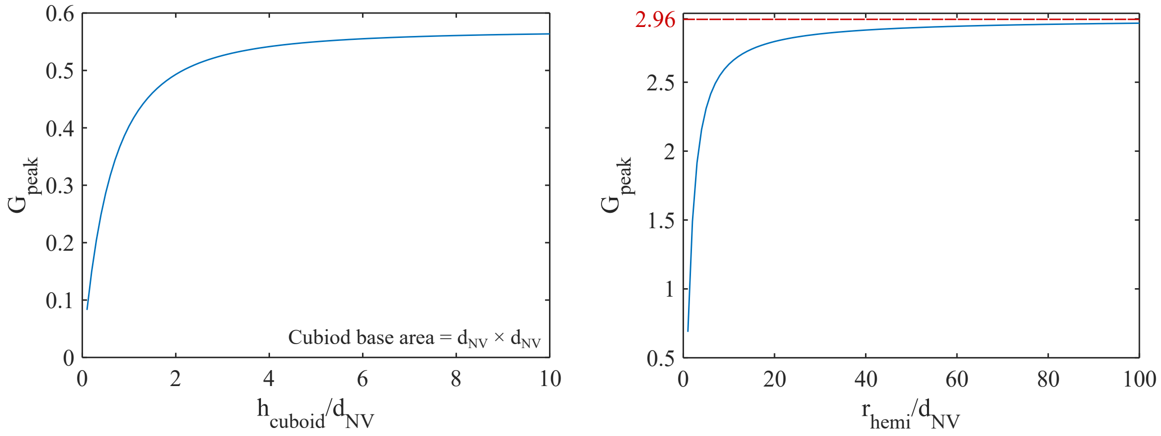

Figure 5.14: **Left** shows the calculation of G_{peak} for a rectangular cuboid volume with varying heights h_{cuboid} and the base length of d_{NV}. The results show that if constructing a microfluidic channel, the depth should be 5 times longer than the width. **Right** shows a similar calculation for a hemisphere with radius r_{hemi}. The calculation suggests that G_{peak} approaches 2.96 as $r_{hemi} \to \infty$. Because of the dimensionless nature of the integral, distances are represented in relative units of d_{NV}.

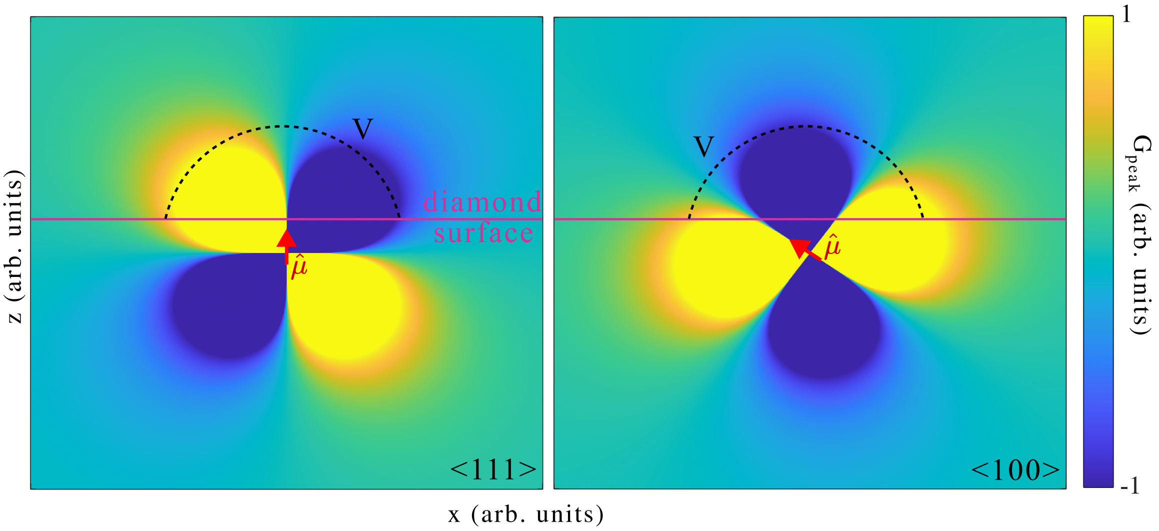

Figure 5.15: The spatial distribution of G_{peak} relative to the NV orientation $\hat{\mu}$. **Left** shows for a <111> sample, over a symmetric volume V above the diamond, G_{peak} averages to zero. Hence, requiring a <100> diamond for Qdyne as shown in **Right**.

At $B_0 = 20\,\mathrm{mT}$ and $T = 300\,\mathrm{K}$, for a sample of pure water under thermal polarisation in the shape of a large droplet, $K = 10\,\mathrm{nT}$. For a <100> NV with $d_{NV} = 50\ \mu\mathrm{m}$, $G_{peak} = 2.97$. Therefore, at this configuration, the NV experiences an oscillating field with $B_{peak-to-peak} = 60\,\mathrm{nT}$, assuming a perfect $\pi/2$ pulse during free induction decay. Hence, the spectrometer needs to have comparable sensitivity.

Similar calculations can be computed for the back action of the NV on the targets. According to Glenn et al. [60], the back-action is on the order of tens of nT, which is a slight modulation to the static field of tens of mT.

To calibrate the sensitivity of the spectrometer, we apply a test signal and compare the spectral response with respect to the signal's output power. Then, a calibration factor is to be determined to convert the output voltage to a magnetic field. We attribute the standard deviation of the spectral noise floor in magnetic field units multiplied by the square root of the measurement time to be the sensitivity of the spectrometer.

The test signal was gated using the wavefunction generator to achieve a consistent phase at the start of each measurement, as the Qdyne response is sensitive to external phase change. Using the same antenna and delivery hardware, the RF signal power is swept from 0 to 10 V on the generator, and the Qdyne responses are shown in figure 5.16. Initially, the spectral amplitude increased with signal power as expected, but a saturation point is observed at 4 V. This is caused by the RF power being too strong that the external field has caused NV phase to evolve beyond π. This has caused the phase to wrap back, and a smaller XY8 response is observed. This behaviour can be modelled, and the theoretical saturation point is used for the voltage to magnetic field conversion factor.

From Barson et al. [13], the Qdyne time response is given by

$$F = F_0[1 + \sin(4B_1\gamma_{NV}\tau_{tot}\cos(f_{aliased}t + \phi_{qdyne}))], \tag{43}$$

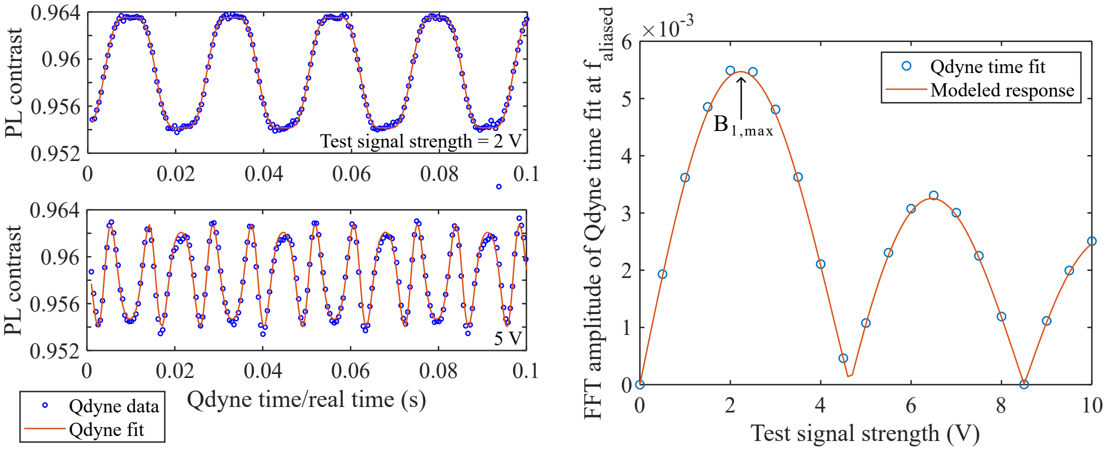

Figure 5.16: **Top Left** shows the measured Qdyne time response to an external signal at 2 V and its fit to equation 43. **Bottom Left** shows a similar measurement at 5 V and its fit. At this higher power, the response is showing higher frequency oscillations, which are the result of phase wrapping, hence reducing the spectral response at the expected f_{alised}. **Right** shows the overall trend of Qdyne amplitude vs signal strength, demonstrating a maximum point where the spectral response is the highest ($B_{1,max}$), which can be used to convert voltage setting to a magnetic field unit [151].

where F_0 is the Qdyne amplitude constant, B_1 is the magnetic field strength of the RF test field, τ_{tot} is the total evolution time of the NV spin during an XY8-N protocol, and ϕ_{qdyne} is the phase of Qdyne response. Therefore, the maximum Qdyne response occurs at $B_{1,max} = \pi/8\gamma_{NV}\tau_{tot}$. To find the theoretical maximum response point, a numerical Fourier transform is applied, and the spectral amplitude as a function of B_1 is determined. This is then used to fit the measured Qdyne spectral amplitude as a function of signal voltage, and the maximum response point is found to be 2 V, which corresponds to a magnetic field of 20 nT. Equipped with the conversion factor, the noise floor of the Qdyne spectrum is sampled, and the sensitivity is 100 pT/$\sqrt{\text{Hz}}$.

The Fourier transform has been solved analytically in reference [13].

Other Qdyne setups have been investigated in order to improve sensitivity. An alternative digitiser (Gage RazorMax 16-Bit PCIe Digitizer, 1 GSamples/s) was acquired to study the fast time dynamics during a Qdyne laser pulse in the previous section. It is now examined for sensitivity. During calibration, the digitiser was found to have a high electrical noise floor as shown in figure 5.17, which corresponded to a sensitivity of 190 pT/$\sqrt{\text{Hz}}$. Despite having a higher noise floor, this digitiser offers a fast sampling rate, which provides additional insights that the slower DAQ cannot offer. This enabled a more detailed examination of the PL response during a laser pulse at every 1 ns, which enabled a more efficient readout. The contrast was improved by optimising the position of the reference window and signal window. Other readout techniques, such as fitting the PL response to a photo-physics model, were also used, which is detailed in the previous chapter. Equipped with an understanding of which part of the PL is more responsive to

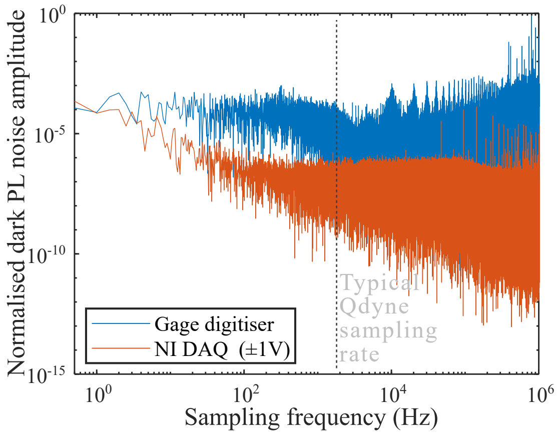

Figure 5.17: Fourier transform of noise measurement at 2 MSamples/s using the NI DAQ and Gage digitiser over 10 s. The inputs are terminated using 50 Ω terminators. This shows that the NI DAQ exhibits a lower electric noise floor at the typical Qdyne sampling rate and would result in a higher Qdyne sensitivity for the same signal.

NV spin states using the faster digitiser, these parameters are then applied back in the DAQ configuration, where the electric noise floor is lower.

Additionally, the digitiser's trigger dead time is only a few µs, which allows for acquisition triggering at each laser pulse. This provided the convenience of not needing to synchronise the clocks for the digitiser and also reduced memory use as the ADC no longer needs to acquire when the laser is off. Although the digitiser does not provide the best sensitivity, it does provide benefits in terms of understanding PL dynamics during a laser pulse, and in turn to be used for readout optimisation and is also a critical troubleshooting instrument.

Other optical configurations are explored. The current setup collects the PL using the same side of the diamond as the laser beam, which requires a dichroic filter. This introduces additional travel distance and diverges from the PL. Two additional collection methods have been explored using the other face of the diamond as shown in figure 5.18. The first method uses a compound parabolic concentrator (CPC) as a collection lens and focuses on the detector using an achromatic lens. The second method uses a half-ball lens with the flat side facing the diamond and a asphereic condenser lens to collect the PL, which is in turn focused using an achromatic lens. A photo of the second method is shown in figure 5.11. Both methods used a 650 nm longpass filter to remove laser contributions. And both methods demonstrated an improvement in PL collection by a factor of 1.4 and 2.3, respectively. The square root of this improvement is the sensitivity enhancement factor if it is at the shot noise limit.

If the PL is boosted, then the dynamic range of the DAQ may need to be increased, which also slightly elevates the electrical noise. Alternatively, the gain on the detector can also be changed.

Placing the detector directly on the diamond with a small lens was also attempted. Although this provided an extra collection. The close vicinity of the trans-impedance amplifier within the detector to the MW antenna created electrical interference; it was not feasible to perform Qdyne in this configuration.

However, ultimately, these optical improvements are not implemented as the second face of the diamond is needed for chemical delivery (see section 5.8). If Qdyne is used for other applications, such as magnetometry, these collection strategies may be of use.

Potential future improvements in sensitivity are explored in Section 5.9. At the thesis submission time, the current sensitivity is at $100\,\mathrm{pT}/\sqrt{\mathrm{Hz}}$, which is close to reference [60], who were able to detect proton signals from pure water in 10 hours. For a long measurement, additional considerations, especially the magnet stability, are required to detect this spectrum.

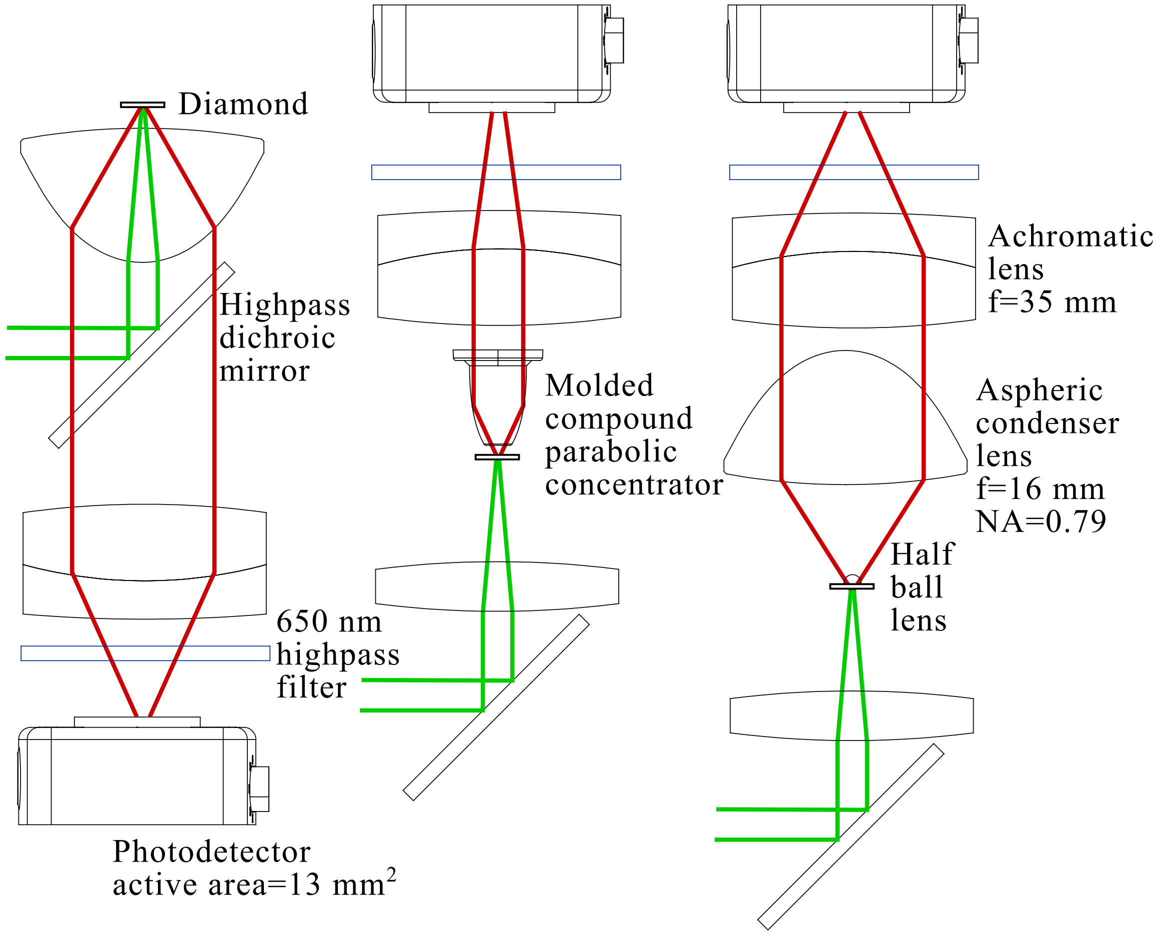

Figure 5.18: Schematics of PL collection strategies. **Left** shows the currently used one-sided collection method. The PL is filtered using a longpass dichroic mirror and focused using an achromatic lens. **Middle** method uses the second side of the diamond and collects the PL via a parabolic concentrator. **Right** method uses a half ball lens and a bigger aspheric condenser lens to collect the PL on the second side of the diamond. Both two-sided approaches using a longpass filter to remove laser contributions in the detector, and the PL is focused using an achromatic lens.

5.6 STABILITY OF DETECTION

In addition to the sensitivity requirement of the spectrometer, there exist other technical hurdles to overcome in order to detect NMR signals. This section will discuss the importance of a stable magnetic field for NMR operations.

Due to the high spectral resolution of the spectrometer, the target of interest shall also have a stable frequency resonance, so that any deviations in frequency do not significantly exceed higher than the spectra resolution during the acquisition time. This implies that the NMR frequency shall remain stable within a few Hz during the measurement. For a 20 mT magnet, this implies that the magnetic field should remain stable within 20-200 nT. For a solution with molar concentrations of thermally polarised target nuclear spins, a measurement may require hours.

In the present setup, rare earth magnets (Nd and SmCo) are used, which are prone to temperature drift; any drifts should be contained below 0.02 °C for SmCo and 0.001 °C for Nd. Although these magnets are cheaper and easier to manipulate, extremely precise temperature control is needed for the working space. Using ODMR, the magnet performance and using a temperature logger, the local magnetic field and temperature are monitored overnight, as shown in figure 5.19. These results suggest that the drifts are too significant for NMR applications, and feedback mechanisms should be considered to stabilise the field. One may consider attaching a thermal electric cooler to the magnet with a feedback mechanism from a platinum resistance thermometer to maintain temperature stability.

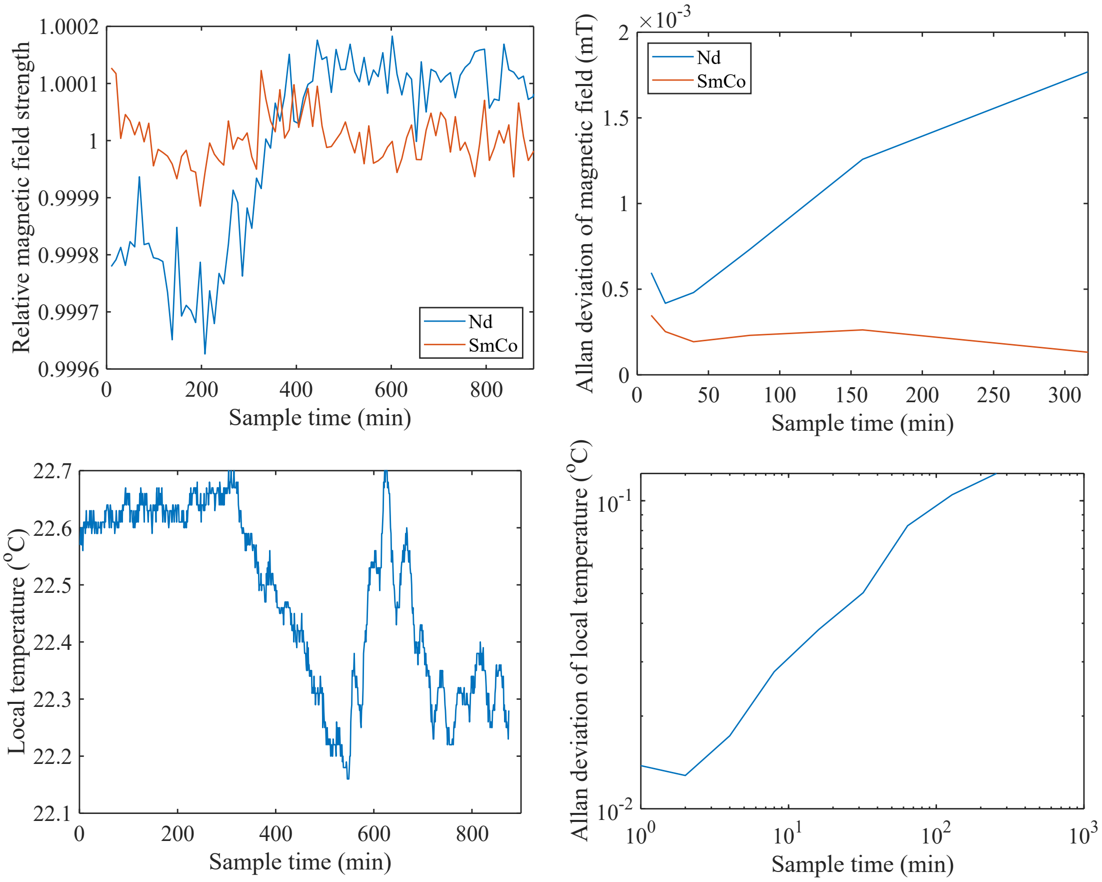

Figure 5.19: A collection of temperature and magnetic field measurements in the lab. **Top Left** shows the relative magnetic field drifts using Nd and SmCo magnets. **Bottom Left** shows the local temperature measurements at the magnet. **Right** shows the Allan deviation analysis of these measurements. Although best efforts have been made to ensure fair comparisons, the measurements were not performed simultaneously as there was only one Qdyne setup available. So, the measurements were performed on consecutive days during the same time period from 4/,pm to 4/,am with the assumption that similar lab conditions, such as air conditioning settings, people movements, and vibration levels, are maintained. At least, a reasonable order of magnitude estimation that temperature and magnetic fields are only stable up to a few minutes/tens of minutes can be deduced from these measurements. This implies that the environment without any temperature compensation is not suitable to maintain ppm level stability during a typical Qdyne NMR operation.

Instead of high-precision temperature control, alternative magnetic strategies such as electromagnets should be considered. These drifts are usually related to the change of resistivity due to the heating of the coils, which is more systematic in nature than random and can be calibrated and adjusted. A parallel-pole gap electromagnet is commonly used in conventional EPR spectrometers and superconducting magnets for NMR spectrometers. These magnets can provide extremely high fields, which boost the thermal NMR signals, but it sacrifices uniformity (in NMR spectrometers, additional shimming coils are used to compensate any spatial variations) and the NV spin mixing becomes more significant at higher fields. So Helmholtz coils with a low noise current source can be a reasonable alternative to rare-earth magnets.

However, the disadvantage of using electromagnets is that it requires a magnetic feedback loop (instead of a temperature one) with a collocated magnetometer, which can be the solvent's NMR signal if it is detectable in a reasonable time, and then adjust for the drift accordingly. This is the working principle of the NMR locking mechanism for conventional spectrometers. When the solvent is not easily detectable, alternative high-sensitivity magnetometers such as vapour cells can be used, but the distance away from the target spins will introduce errors.

Maintaining ppm stability in magnetic fields is critical for NMR applications, and electromagnets can offer a more controllable stability. However, it does come at a higher SWaP requirements, such as energy, space, and cost compared to permanent magnets compared to temperature-controlled rare earth magnets. The choice should be carefully considered depending on the application needed. Also, magnetic shielding such as μ-

Conventional table top NMR spectrometers often use permanent magnets and compensate for any temperature drift. However, their stability performance is usually sacrificed for a lower SWaP requirement. Sometimes they are operating under a fumehood, which makes temperature control harder.

metal or degaussing units can be used to mitigate any sudden external influences, such as trains.

In addition to magnetic field drifts, phase noise from signal generators can also occur from variations in temperature. These noises usually arise from μK drifts in the onboard oven-controlled oscillator source and can also affect Qdyne NMR performance [17], but not as significantly as magnet field drifts.

5.7 SPATIAL UNIFORMITY

Besides variations in time, variation in space should also be considered across the sensing volume, because any inhomogeneities in the magnetic field will cause NMR line broadening, which should be kept below the ppm level. This section will discuss the uniformity of rare-earth magnet and electromagnet configurations for Qdyne NMR purposes.

Due to the NMR signals vanishing for <111> and <110> orientations, the external magnetic field applied needs to be at an angle to the NV surface, which is usually 54.7° for <100> diamonds. This implies that angle control is important. Secondly, the now tilted magnetic field relative to the lab frame needs to be centred on the sensing volume, hence spatial control is also of importance. These all apply to any compensating fields if used.

To measure the magnetic field angle relative to the NV surface, quantum sensing techniques can be used. The NV PL has a magnet field angle dependence near 50 mT due to spin mixing [48], also in XY8-N or CPMG measurements, additional resonances can be observed from a misaligned parent nitrogen nuclear spin [98]. By maximising the PL count rate and minimising parent nitrogen spin resonance, fine-tuning of the magnetic field angle can be achieved.

To measure the spatial uniformity of the magnetic field, magnetic resonance techniques can be used. ODMR of the NVs across the laser spot can provide a rough indication of the magnetic strength distribution, but high-sensitivity NV magnetometry is challenging. The better method of uniformity measurement is to perform the actual Qdyne-NMR on nuclear spins in the sensing volume and examine the NMR linewidth with respect to magnet position. In conventional NMR spectrometers, this technique is as known as shimming, but instead of repositioning the magnet, spatial compensation coils are used to keep the sensing volume uniform. For Qdyne NMR, the use of shimming coils can be challenging as the sensing volume is much smaller.

The repositioning and re-angling of the permanent magnet relative to the sensing volume can be achieved by using physical (motorised) translational and rotational controls. For electromagnets, this can be achieved using multi-axis Helmholtz coils. The current used on individual coils relative to others can be adjusted to manipulate the position and angle of the magnetic field.

In addition to angle and position demands, the magnet configuration also needs to accommodate the equipment overheads in the immediate diamond surroundings, including PCB with MW/RF cables, optical components under the diamond, chemical delivery systems, and position control of the diamond. The magnet setup needs to be able to spatially fit into this environment, and any magnetic interference from the overheads should be compensated.

The design of the magnets needs to conform to the spatial constraints and angle/position requirements. For permanent magnets, a dual disk setup can provide a high level of uniformity between the gaps due to the geometric symmetry compared to a single disk design. However, due to the spatial overheads and the angle requirement, the advantage in uniformity is diminished. Similar arguments apply to Halbach arrays and pole gap magnetic circuits, unless a large working gap can be achieved, which can be expensive. Hence, for a permanent magnet setup, a large single disk design is considered. For non-NMR qdyne applications that require a high B_0 field uniformity, where <111> diamonds can be used, Halbach arrays or dual disk magnets can be used as they can be placed along the perpendicular axis to the diamond surface, providing a symmetrical setup and ease of access.

The spatial variation for rare-earth permanent magnets and electromagnets is compared. Finite element simulations for the field distribution across the sensing volume of an angled hemisphere are performed and shown in figure 5.20 and 5.21. The results suggest that across the micron-scale sensing volume, the electromagnet is more uniform than the disk magnet at the <100> orientation. And, the disk magnet is more prone to mispositioning, as the uniformity reduces more when off-centred compared to the electromagnets, and due to manufacturing defects, as any surface bumps may alter the field lines. Because of the necessity of using <100> samples, any spatial symmetric advantages of rare earth magnets are reduced, so electromagnets are the more appropriate choice at the cost of SWaP.

The MW field can also vary in space under the omega-shaped antenna design. This may cause errors in NV control and lead

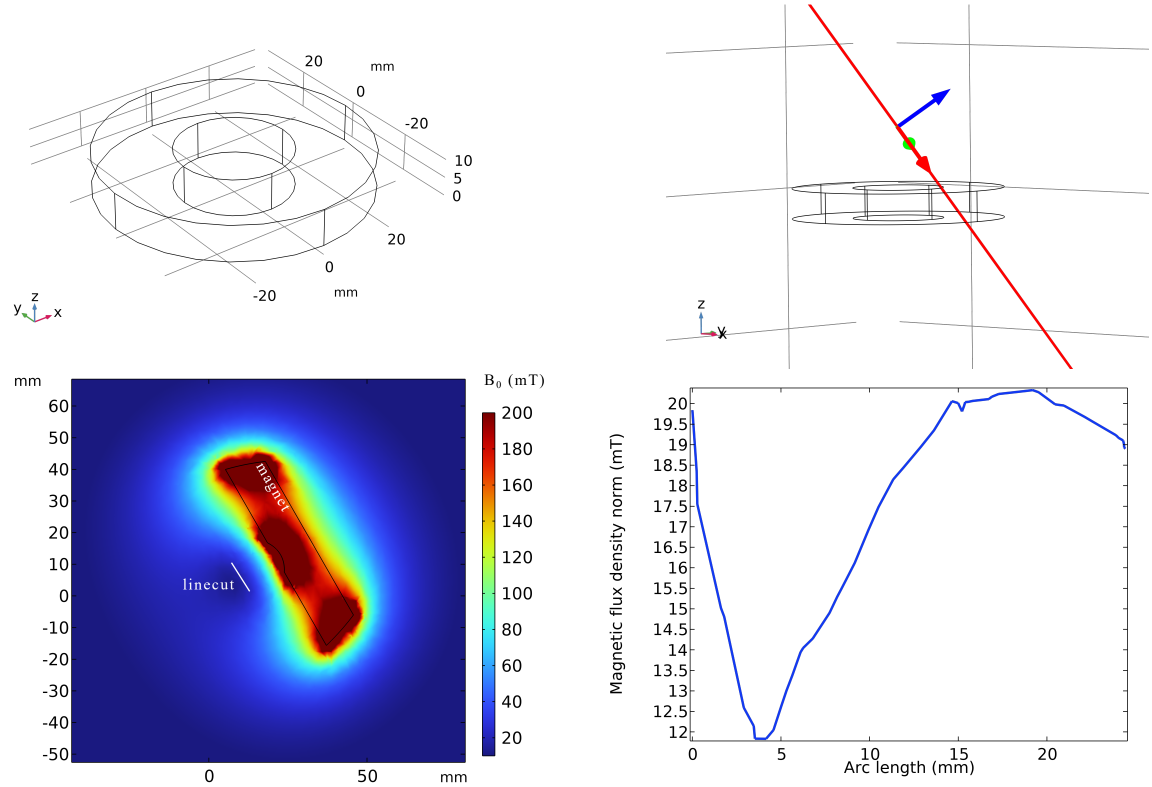

Figure 5.20: Finite element simulation of a disk-shaped permanent magnet using COMSOL. **Top Left** shows the shape of the magnet. **Top Right** defines the volume of interest, in which the magnetic field distribution is calculated. The plane perpendicular to the blue arrow will be simulated (in the direction of the <100> crystallographic axis). **Bottom Left** shows the overall magnetic field distribution across the red line. The black box is an outline of the magnet. The white line represents a 1D line cut of the magnetic field in the region of interest, representing the surface of the diamond, as shown in **Bottom Right**.

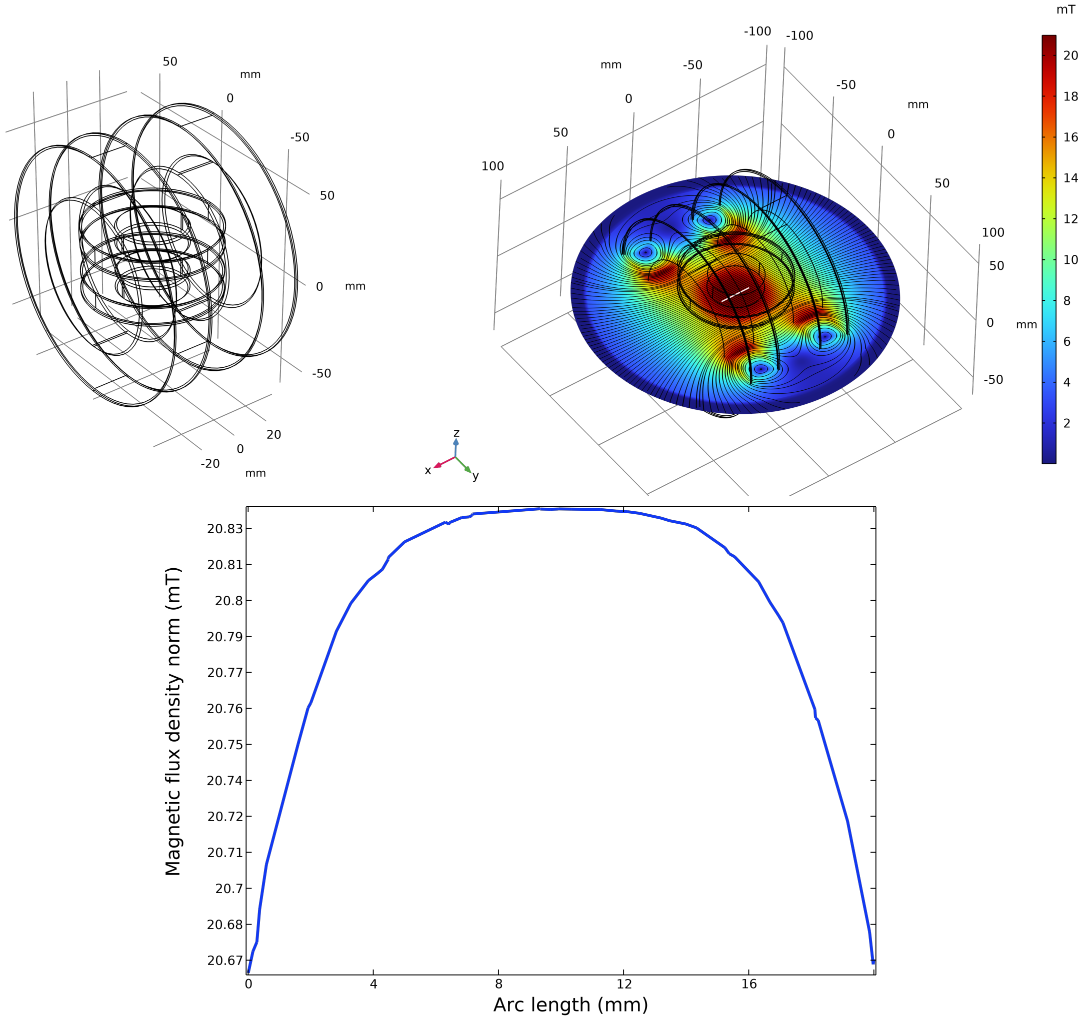

Figure 5.21: Finite element simulation of sets of Helmholtz coils using COMSOL. **Top Left** shows the geometry of the coils. Two sets of coils were used to create a bias field direction that is in the direction of the <100> crystallographic axis at the centre. This design also ensures that there is space to place the PCB with the diamond at the centre of the coils. **Top Right** demonstrates a 3D magnetic heat map of the simulation. The white line represents a 1D line cut at the region of interest, where the surface of the diamond is expected to be. **Bottom** is the magnetic field distribution across the line cut. The magnetic field strength and the length of the line cut length are selected to be comparable with figure 5.20.

to NMR line broadening, but this is less significant compared to broadening due to incorrect positioning of the magnet, although this poses a potential issue, it is not the most critical one. Potential solutions include the use of shaped MW pulses (hyperbolic shapes) and improved antenna design.

5.8 INCORPORATION OF NV-NMR WITH FLOW CHEMISTRY

In recent decades, reaction under a microfluidic chip has become a popular area of research with a significant industrial outlook due to advances in fabrication techniques such as soft lithography. It offers advantages in scalability, reduction in human errors and labour costs; combining these benefits can improve reaction control in an industrial setting and provide higher chemical yields and refined controls in a biological context. In research, flow chemistry can be used to monitor and visualise reaction progress. Consider a colour-changing reaction in a flow cell, where the flow distance represents the reaction progress. One may observe a slight colour change near the input of the cell and a greater change near the output. This allows for a closer examination of reaction intermediates and kinetics as the flow cell can spatially separate the temporal response during a reaction. Because the NV centre in diamond offers microscale sensitivity with an inert interface, the combination of diamond sensors with microfluidics has great potential in scientific and industrial settings [47]. In this section, the design and fabrication of microfluidics are discussed, and an in situ reaction monitoring mechanism via NV-Qdyne-NMR is proposed.

The material of the microfluidic chip has a few requirements for NMR operation. It needs to have

- high structural rigidity under laser and microwave,
- minimal background NMR signals,
- low paramagnetic noise,
- high solvent compatibility and
- high strength to withstand pressure.

Although polymer materials such as polydimethylsiloxane (PDMS) are commonly used in microfluidics due to their malleable nature, their chemical structure has Hydrogen and Carbon contributions, hence giving a background NMR signal, which adds unwanted complexity in the spectrum [47]. Other concerns, such as degradation under laser is also undesirable. Glassy polymers can be less problematic candidates due to their high rigidity and low NMR contributions. Gassy polymers such as polymethyl methacrylate (PMMA) usually contain protons, but they exhibit short-lived NMR relaxation times. However, it can degrade with certain organic solvents. Hence, high-quality glass is an ideal candidate for microfluidics chip design due to its robustness. However, fabricating channels on such materials can be challenging and costly. An external commercial femtosecond laser micro-machining company (Quoba Systems) generated trench-like features on the surface of the glass.

If using water as a solvent, PMMA can be a cost-effective option.

The microfluidic chip design is split into two glass pieces. The first piece was cut through in the middle with a square opening, which is where the diamond sits. The second piece has straight trenches running across the surface of the glass at 100 μm depth. There are three different channels with varied widths for testing purposes. The cleaned glass pieces are glued together by brushing a minimal amount of PDMS on the plain surfaces. Other gluing methods, such as the application of vacuum grease, can be used if the pressure of the microfluidics pump is minimised. After gluing (Gorilla Glue) the glasses together, the diamond membrane is glued on top of its designed opening. The ports of the microfluidics (PDMS) are commercially acquired the delivery tubes coming from the pumps are also glued down.

The two-piece design shown in figure 5.22 enables direct contact of the chemicals to the diamond surface, reducing standoff distance. However, this introduces additional complexity in assembly and design, such as difficulties in gluing and ensuring the opening matches the diamond dimension, so no leakages occur. One may also consider fabricating trenches directly on the diamond surface as shown in 5.23, if fabrication challenges can be solved [82].

Due to the use of lasers and MWs, the solution may evaporate under the Qdyne pulse sequence. Although the use of enclosed channels can mitigate evaporation, the use of additional radiation sources can be potentially invasive to the sample of interest. To reduce laser radiation, anti-reflection layers may be considered at the cost of additional standoff distance, or total internal reflection fluorescence (TIRF) methods, as shown in 5.23, can be used at the cost of additional overheads around the diamond for an angled laser delivery. To combat MW radiation, efficient resonators (with high uniformity across the laser spot) can be designed or MW protocols with low power requirement, such as the CPDD protocol [99], may be employed.

Equipped with microfluidic channels and NV-NMR detection, this apparatus can enable NMR measurements at different stages of a dynamical reaction by adjusting the pump pressure, which will deliver different chemical environments to the sensing volume, such as reactions at an early stage to a later stage.

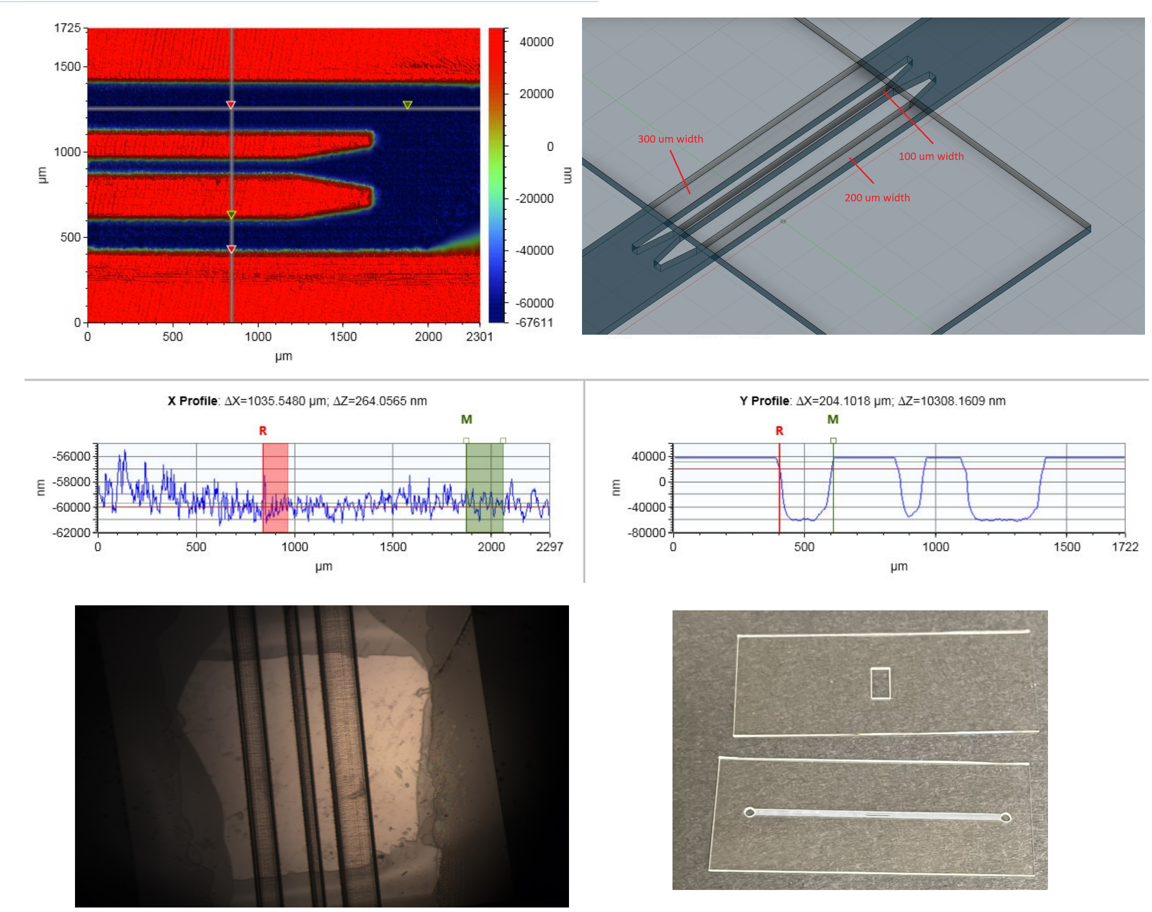

Figure 5.22: **Top Right** shows the design of the microfluidic channels. Channels with varying widths were used for testing purposes. **Top left** is a dimension measurement of the fabricated chip by the manufacturer, with linecuts shown in **Middle**. **Bottom Right** shows a picture of the completed chips. **Bottle Left** is a microscope picture of the assembled chip with the diamond glued on.

Common microfluidic elements such as fluidic diodes, gates, and valves can also be implemented into the workflow. These can allow for in situ chemical monitoring under a reaction, investigating reaction intermediates and mechanism, providing insights into synthesis-based chemistry with new dynamical NMR information, which was difficult to access before.

One can also move the laser spot to different parts of the channel to investigate different stages of reaction, but this may require additional recalibration of magnetic fields.

However, there are certain constraints to this proposed technique in addition to conventional NMR sample requirements. The chemical environment should not be altered under green light and MWs, and emit red. These additional constraints may limit its applications in optically sensitive samples, but there is still a significant part of the chemistry where it may provide benefit.

The importance of this NV-NMR microfluidic system depends on the temporal resolution of the NMR investigation, which in turn depends on the sensitivity of the setup and the signal strength of the external target, which are discussed in the next section.

5.9 FUTURE PATHWAYS TO SENSITIVITY AND SNR GAIN

There are two directions to improve the sensitivity of the spectrometer. First is the reduction of noise in electronics, optics, and magnets; second is the elevation of the signal during measurement.

For noise sources, there is the electrical noise from the ADC and the amplifiers within the detector. Improving in this direction requires efforts in electrical engineering, such as a reduction in phase noise and improvement in clock accuracy. The second source is the laser technical noise. This can be suppressed by using an auto-balancing mechanism to reach the shot noise limit. This requires a second detector to sample the laser noise, and any PL noise that correlates to the measured laser noise can be reduced in the electronics or postprocessing [32]. The laser itself may also be treated with a high-quality power supply and temperature regulator.

To boost the spectrometer signal, one can collect more PL photons or improve spin contrast. Due to the high refractive index of the diamond, there exists a significant portion of the PL not reaching the active area of the photodetector. To mitigate this issue, fabricating a tailored-made condenser lens on the surface of the diamond or the use of integrating spheres can be used. One way to avoid the total internal reflection of the PL is to create a medium for the PL to travel to without a change of refractive index. This can be achieved by fabricating diamond lens structures or waveguides on the surface and bringing the detector closer, provided that electromagnetic interference can be avoided. Micro-fabrications of diamond structure are achievable, but require significant effort and suffer from poor scalability. The other direction is to increase the active area of the detector, but there is usually a trade-off between size and bandwidth, which needs to be at ~MHz to detect contrast change in the PL. Prototyping a custom-made photodetector with a balancing functionality and a larger active area size compared to commercially available detectors can be of interest. One can also consider improving the NV charge state stability in the diamond or developing new readout procedures to boost readout SNR in the spin contrast, similar to works in the previous chapter.

NV electrical readout can also be of use for Qdyne NMR. This eliminates the need for collection optics, but requires the fabrication of electrical contacts. Also, electrical readouts require stronger laser power and can be slower than optical methods, which can lower sensitivity.

Although the sensitivity of the spectrometer itself is critical, one can also manipulate the chemical target to provide additional signal strength. The use of microfluidics can enable well-controlled delivery of the sample. This can be taken advantage of by creating a solution with a stronger NMR signature elsewhere before delivering to the sensing volume. To boost NMR signals, one can use stronger magnets (or cooler temperatures) to improve the Boltzmann distribution. Alternatively, hyperpolarisation techniques can be used, such as the transfer of MW manipulatable electronic spin polarisation to nuclear spins using certain radicals or the near-surface NVs or other optical polarised agents. Some of these techniques can be performed without interfering with NMR operation, which can be incorporated at the sensing volume. If not, the delivery speed of the solution needs to be optimised to balance the thermal relaxation time when out of the polarisation region and polarisation transfer rates inside the region. Despite the potential for being invasive, hyperpolarisation of NMR signals is an active area of research, and the NV-NMR microfluidics system can be a flexible platform to capitalise on any gains in this direction [135].

5.10 CONCLUSION

In summary, this chapter has demonstrated an NV-NMR protocol that can measure high-resolution NMR spectra. A proof-of-

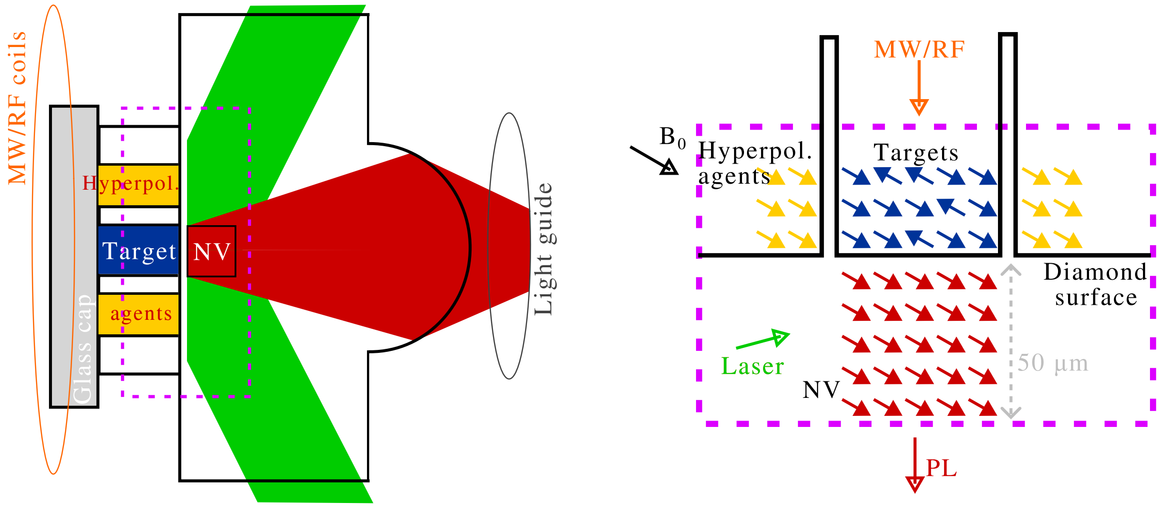

Figure 5.23: A proposed Qdyne-NMR system. The laser path comes at an angle for TIRF delivery to minimise green exposure to the sample. The collection side of the diamond is fabricated in the shape of a lens to guide the PL more effectively to an adjacent light guide by avoiding the total internal reflection of the PL at the diamond surface. The sample side of the diamond has trenches fabricated on the surface for microfluidics delivery with three channels. The middle one is for the NMR targets, and the two channels on the side are reserved for any hyperpolarisation agents to boost the NMR signal. The gap between the target and hyperpolarisation agents should be minimised. The channels are capped to avoid evaporation. MW and RF are delivered at the cap to increase efficiency. The NV layer is 50 µm.

principle experiment showed a spectral linewidth of 300 mHz using a test signal. However, the drawback of this protocol is that the NV-target standoff distance is reduced to μm due to statistical polarisation at the nanoscale. This requires the spectrometer to process high sensitivity for NMR detection. A sensitivity of $100\,\mathrm{pT}/\sqrt{\mathrm{Hz}}$ has been calibrated using the apparatus described in this chapter, which is comparable to the existing literature that took hours to measure a spectrum. Due to the sharp linewidth, this suggests the need for stability controls over the hours of measurement time. This was difficult to achieve using the current magnet setup, and it is believed to be the main cause for the non-detection of the signals. Alternative electromagnet setups were discussed to relieve this issue. Also, other pathways are discussed to boost the NMR signal strength or spectrometer sensitivity in order to reduce the measurement time.

Despite the current constraints, the potential is within reach, and the future improvement works are already in progress. Once the magnet stability issue has been tackled, incorporating this protocol in a lab-on-a-chip device will be achieved, and a proof-of-principle demonstration of in situ time-dependent high-resolution NMR spectroscopy can be performed. The promising aspect of this system is that it can become a platform to develop further sensitivity boosts and hyperpolarisation techniques.

Part IV

HIGH SPECTRAL AND SPATIAL RESOLUTION NMR AND OTHER FUTURE DIRECTIONS

6

OUTLOOK AND CONCLUSION

The final chapter of this thesis will introduce some future pathways for NV-based NMR spectroscopy. The first section explores an emerging field of ZULF NMR spectroscopy, which provides unique molecular information that cannot be obtained at higher fields. The second section combines high spatial and spectral NV NMR performance by discussing the feasibility of Qdyne protocols at the nanoscale.

6.1 ZERO TO ULTRA LOW FIELD NMR USING NVS

In chapter 1, the NMR interaction Hamiltonian, such as J-coupling were introduce,d and secular approximations were applied. Such treatment truncates certain terms in the interaction tensor when they do not commute with the stronger Zeeman interactions. The main consequence of ZULF NMR is that when $B_0 \approx 0$, the Zeeman interactions are no longer dominant and the previously truncated terms surface.

In addition, at ZULF, the SWaP requirements reduce as the need for uniform magnetic environments (such as susceptibility plugs or shimming coils) can be neglected. Also, metallic components can be introduced in ZULF settings, where the skin depth of ZULF frequencies (less than kHz) is significantly larger than MHz, allowing for NMR studies in metallic enclosures such as batteries or monitoring the spoiling process of tomatoes in metal containers [19, 29, 128].

When the J-coupling interactions becomes dominate, and chemical shifts are negligible at ZULF, detailed J-coupling information can be probed [95]. This is known as J-spectroscopy. This can be used to study the dynamics of prepolarised heteronuclear energy transfer, because at ZULF, their resonance frequencies overlap, thus the polarisation can begin to oscillate between the spins. By probing the polarisation transfers, bond-forming or breaking processes can be monitored as J-coupling is mediated through bonds. Barskiy et al. [12] have modelled ZULF J-spectra of ammonium ion solutions. By varying pH, thus ammonium ion and water proton bond breaking and forming rates vary over orders of magnitude and can be probed in ZULF NMR. Other potential applications, such as antisymmetric J-coupling spectroscopy used to study chiral molecules [55, 85], the search for dark matter [56] and hyperpolarisation techniques at ZULF [155] are also emerging in this field.

The advancement of ZULF NMR has been coupled with developments in two areas, hyperpolarisation in nuclear spins and sensitive magnetometry. Because at ZULF, the Boltzmann distribution in equation 11 dictates that the number of spins contributing to NMR signals is extremely small, thus requiring techniques to boost the NMR signal. On the detection side, technologies that outperform induction techniques at ZULF frequencies have emerged, such as NV centres in diamond, optically pumped magnetometers (OPM) and superconducting quantum interference device (SQUID) [28, 117, 130].

Because the NV is capable of detecting statistically polarised spins, which can exhibit high NMR signals at ZULF due to the fact that statistical polarisation depends on $\sqrt{N}$ and not on B_0. By integrating NV NMR with ZULF NMR, the need for sample pre-(hyper)polarisation can be removed, thus preserving its natural state. By fabricating shallower NVs, the reduction of N or the boosts in NMR signal also mitigate the need for better magnetic field sensitivity. At ZULF, to avoid spin mixing between the $m_s = +1$ and -1 states, circularly polarised MW need to be engineered to drive distinctive transitions [114]. Also, the diffusion broadening issue is still present, thus limiting the target to be either immobilised or in a solid state. In the next section, the performance of the high spectral resolution Qdyne protocol in a diffusion-limited setting will be explored.

6.2 NV QUANTUM HETERODYNE AT NANOSCALE

Due to the nature of statistical polarised spins, nanoscale NMR signals exhibit random fluctuating phase and amplitude, hence the heterodyne approach, which typically requires a stable oscillatory signal,s is difficult and requires significantly longer acquisition time compared to decoherence-based spectroscopy [144]. In diffusion-limited experiments, these correlation times in Qdyne were assumed to decay exponentially; information is lost at longer integration durations. However, Staudenmaier et al. [153] have demonstrated that the scaling relation is a power law instead of an exponential dependence, thus lingering information is still available at longer time scales and nanoscale Qdyne NMR is possible. Experimentally, the same Qdyne protocol can be applied without the need for a $\pi/2$ pulse for the thermal nuclear spins, and experimental overheads such as uniformity can be reduced. Schmitt [139] has demonstrated that nanoscale (5 nm deep NV) Qdyne NMR on oil-based targets and achieved spectral resolution of 2 kHz at 23 mT. Thus, showing a proof of principle demonstration that Qdyne can be performed on statically polarised targets. However, this spectral linewidth cannot resolve chemical shifts, and compared to decoherence-based spectroscopy, it needs a significantly longer measurement time.

It is thus fair to assume that these experiments are still limited in linewidth by the diffusion issue. However, there are certain remedies that can lower this limitation, either by reducing diffusion or boosting measurement speed. One strategy to tackle the diffusion problem is to constrain the targets of interest within a nanoscale volume. Chemical tethering, such as the creation of amine functionalised surfaces, can enable the localisation of nuclear targets within a nanoscale sensing volume [79]. In addition, the creation of nanoslits or nanofludic channels through the use of etching techniques such as focused ion beams can be considered too [82]. However, chemical modification or nanoscale physical landscaping of the diamond surface can erode the stability of near-surface NV centres, which effectively increases interaction distance. Significant challenges still exist in either revitalising the near-surface NVs after these modifications or reducing these side effects. Other less invasive (to the diamond) target immobilisation techniques can involve the use of gel media [41] or capping layers [125], such as hexagonal boron nitride to confine targets between itself and the diamond surface. These techniques significantly suppress translational diffusion, but also rotational diffusion, which creates dipolar broadening, diminishing the spectral resolution. A more promising alternative is the use of nanoscale encapsulation chambers, which are prominent in nanoscience applications such as drug delivery and energy storage [54, 74]. These can constrain translational diffusion, while allowing for rotational diffusion. An example is the application of metal-organic frameworks, which showed entrapment of molecules in a volume of 10 nm^3 and demonstrated ^{31}P NV NMR with kHz spectral resolution [97]. However, experimental demonstrations on the use of encapsulation chambers in NV NMR — particularly in combination with Qdyne — still remain limited, and a significant knowledge gap still exists.

The NVs can also be used to quantify diffusion. Bruckmaier et al. have demonstrated the use of NV-based MRI measurements at the micron scale [23]. Their experiment employed spatial gradient RF coils for the gradient spin-echo pulse sequences and achieved optical imaging of water (from the NV PL) with diffusion information. Due to the reliance on gradient coils, this technique faces the same roadblock to conventional MRI — the engineering of gradient fields at the nanoscale. Alternatively, the use of correlation spectroscopy has revealed that nanoscale confined water at the diamond surface exhibits much slower diffusion rates compared to bulk water [125]; a similar experiment that uses a scanning probe microscopy tip to stimulate water on a hydrophilic diamond surface has been reported too [179]. The recent advances in nanoscale NV NMR spectroscopy suggest a growing need to understand the solvent–diamond interface, presenting an opportunity for research towards this direction.

In addition to localising NMR targets, boosting measurement speed can be achieved by improving SNR in the spectrometers through, for example, readout improvements or increasing signal strength via hyperpolarisation [62]. Despite the challenges outlined in this section, nanoscale high spectral resolution NMR is a highly lucrative goal to pursuit and there is still room for improvement.

6.3 CONCLUSION

NMR spectroscopy is a proven and popular tool in various fields of science due to its high chemical selectivity and low invasiveness, but its hallmark disadvantage is the poor sensitivity. This thesis has introduced an atomic-scale quantum sensor, the NV centre in diamond, that is capable of detecting NMR signals at the nanoscale. However, the NV-based NMR is not without its own challenges. Part II of the thesis has demonstrated that improvements in readout protocols can mitigate the low throughput challenge and how optical noise can affect NV NMR performance. At the nanoscale, due to diffusion, the spectral resolution, which dictates the amount of chemical information available, is limited. In part III, the quantum heterodyne protocol, which offers improvements in resolution, is investigated, and potential applications are envisioned. In the final part, the future of NV NMR is explored, and new directions such as zero- to ultra-low field NMR are discussed.

To encapsulate, the present challenge with NV NMR is the dilemma between spatial sensitivity and spectral resolution. Thus, future works of tackling sample diffusion broadening are called upon. Nonetheless, the progress so far is capable of offering new applicable insights. As detailed in this thesis, areas such as flow chemistry can be improved by integrating NV NMR in microscale flow reaction systems, which enables in situ monitoring of chemical reactions.

BIBLIOGRAPHY

[1] S. Ahmadi, H. A. R. El-Ella, J. O. B. Hansen, A. Huck, and U. L. Andersen. "Pump-Enhanced Continuous-Wave Magnetometry Using Nitrogen-Vacancy Ensembles." In: *Phys. Rev. Appl.* 8 (3 2017), p. 034001. DOI: `10.1103/PhysRevApplied.8.034001`.

[2] F. Aiello and S. Masi. "The Contribution of NMR Spectroscopy in Understanding Perovskite Stabilization Phenomena." In: *Nanomaterials* 11.8 (2021). DOI: `10.3390/nano11082024`.

[3] R. D. Allert, K. D. Briegel, and D. B. Bucher. "Advances in nano- and microscale NMR spectroscopy using diamond quantum sensors." In: *Chem. Commun.* 58 (59 2022), pp. 8165–8181. DOI: `10.1039/D2CC01546C`.

[4] J. Anders, F. Dreyer, D. Krüger, I. Schwartz, M. B. Plenio, and F. Jelezko. "Progress in miniaturization and low-field nuclear magnetic resonance." In: *Journal of Magnetic Resonance* 322 (2021), p. 106860. DOI: `10.1016/j.jmr.2020.106860`.

[5] J.-H. Ardenkjaer-Larsen et al. "Facing and Overcoming Sensitivity Challenges in Biomolecular NMR Spectroscopy." In: *Angew. Chem., Int. Ed.* 54 (32 2015), pp. 9162–9185. DOI: `10.1002/anie.201410653`.

[6] N. Arunkumar et al. "Micron-Scale NV-NMR Spectroscopy with Signal Amplification by Reversible Exchange." In:

PRX Quantum 2 (1 2021), p. 010305. DOI: 10.1103/PRXQuantum.2.010305.

[7] N. Aslam et al. "Nanoscale nuclear magnetic resonance with chemical resolution." In: *Science* 357.6346 (2017), pp. 67–71. DOI: 10.1126/science.aam8697.

[8] Atta-ur-Rahman and M. I. Chaudhary. *Applications of NMR Spectroscopy*. Bentham Science Publishers, 2015.

[9] Atta-ur-Rahman, M. I. Choudhary, and W. J. Thomsen. *Bioassay Techniques for Drug Development*. Harwood Academic Publishers, 2001.

[10] J. F. Barry, J. M. Schloss, E. Bauch, M. J. Turner, C. A. Hart, L. M. Pham, and R. L. Walsworth. "Sensitivity optimization for NV-diamond magnetometry." In: *Rev. Mod. Phys.* 92 (1 2020), p. 015004. DOI: 10.1103/RevModPhys.92.015004.

[11] D. A. Barskiy, J. W. Blanchard, D. Budker, J. Eills, S. Pustelny, K. F. Sheberstov, M. C. D. Tayler, and A. H. Trabesinger. *Zero- to Ultralow-field Nuclear Magnetic Resonance*. 2025. DOI: 10.48550/arXiv.2409.09048.

[12] D. A. Barskiy et al. "Zero-field nuclear magnetic resonance of chemically exchanging systems." In: *Nature Communications* 10.1 (2019), p. 3002. DOI: 10.1038/s41467-019-10787-9.

[13] M. S. J. Barson, L. M. Oberg, L. P. McGuinness, A. Denisenko, N. B. Manson, J. Wrachtrup, and M. W. Doherty. "Nanoscale Vector Electric Field Imaging Using a Single Electron Spin." In: *Nano Letters* 21.7 (2021). PMID: 33739842, pp. 2962–2967. DOI: 10.1021/acs.nanolett.1c00082.

[14] M. Bastawrous et al. "From hemolymph to in-vivo: The potential of a 1 mm microlitre flow probe with separate lock chamber for NMR metabolomics in mass limited environmental samples." In: *Journal of Magnetic Resonance Open* 12-13 (2022), p. 100079. DOI: `10.1016/j.jmro.2022.100079`.

[15] E. Bauch et al. "Decoherence of ensembles of nitrogen-vacancy centers in diamond." In: *Phys. Rev. B* 102 (13 2020), p. 134210. DOI: `10.1103/PhysRevB.102.134210`.

[16] L. Benini. "Quantum sensing at the megabar frontier." In: *Nature Physics* 20.4 (2024), pp. 543–543. DOI: `10.1038/s41567-024-02485-1`.

[17] A. Berzins et al. *The impact of microwave phase noise on diamond quantum sensing*. 2024.

[18] C. A. Bettenhausen. "Bruker installs world's strongest NMR." In: *C&EN Global Enterprise* 98.19 (2020), pp. 12–12. DOI: `10.1021/cen-09819-buscon10`.

[19] J. W. Blanchard, D. Budker, and A. Trabesinger. "Lower than low: Perspectives on zero- to ultralow-field nuclear magnetic resonance." In: *Journal of Magnetic Resonance* 323 (2021), p. 106886. DOI: `10.1016/j.jmr.2020.106886`.

[20] F. Bloch, W. W. Hansen, and M. Packard. "The Nuclear Induction Experiment." In: *Phys. Rev.* 70 (7-8 1946), pp. 474–485. DOI: `10.1103/PhysRev.70.474`.

[21] J. M. Boss, K. S. Cujia, J. Zopes, and C. L. Degen. "Quantum sensing with arbitrary frequency resolution." In: *Science* 356.6340 (2017), pp. 837–840. DOI: `10.1126/science.aam7009`.

[22] G. Bourdarot. "Heterodyne interferometry: review and prospects." In: *Optical and Infrared Interferometry and Imaging VIII*. Ed. by A. Mérand, S. Sallum, and J. Sanchez-Bermudez. Vol. 12183. International Society for Optics and Photonics. SPIE, 2022, p. 1218312. DOI: 10.1117/12.2635601.

[23] F. Bruckmaier, R. D. Allert, N. R. Neuling, P. Amrein, S. Littin, K. D. Briegel, P. Schätzle, P. Knittel, M. Zaitsev, and D. B. Bucher. "Imaging local diffusion in microstructures using NV-based pulsed field gradient NMR." In: *Science Advances* 9.33 (2023), eadh3484. DOI: 10.1126/sciadv.adh3484.

[24] F. Bruckmaier, K. D. Briegel, and D. B. Bucher. "Geometry dependence of micron-scale NMR signals on NV-diamond chips." In: *Journal of Magnetic Resonance Open* 8-9 (2021), p. 100023. DOI: 10.1016/j.jmro.2021.100023.

[25] D. B. Bucher, D. P. L. Aude Craik, M. P. Backlund, M. J. Turner, O. Ben Dor, D. R. Glenn, and R. L. Walsworth. "Quantum diamond spectrometer for nanoscale NMR and ESR spectroscopy." In: *Nature Protocols* 14.9 (2019), pp. 2707–2747. DOI: 10.1038/s41596-019-0201-3.

[26] D. B. Bucher, D. R. Glenn, H. Park, M. D. Lukin, and R. L. Walsworth. "Hyperpolarization-Enhanced NMR Spectroscopy with Femtomole Sensitivity Using Quantum Defects in Diamond." In: *Phys. Rev. X* 10 (2 2020), p. 021053. DOI: 10.1103/PhysRevX.10.021053.

[27] J. Budimir and J. L. Skinner. "On the relationship betweenT1 andT2 for stochastic relaxation models." In: *Jour-*

nal of Statistical Physics 49.5 (1987), pp. 1029–1042. DOI: 10.1007/BF01017558.

[28] D. Budker. "Extreme nuclear magnetic resonance: Zero field, single spins, dark matter. . . " In: *Journal of Magnetic Resonance* 306 (2019), pp. 66–68. DOI: 10.1016/j.jmr.2019.07.009.

[29] D. B. Burueva, J. Eills, J. W. Blanchard, A. Garcon, R. Picazo-Frutos, K. V. Kovtunov, I. V. Koptyug, and D. Budker. "Chemical Reaction Monitoring using Zero-Field Nuclear Magnetic Resonance Enables Study of Heterogeneous Samples in Metal Containers." In: *Angewandte Chemie International Edition* 59.39 (2020), pp. 17026–17032. DOI: 10.1002/anie.202006266.

[30] L. Busaite, R. Lazda, A. Berzins, M. Auzinsh, R. Ferber, and F. Gahbauer. "Dynamic ^{14}N nuclear spin polarization in nitrogen-vacancy centers in diamond." In: *Phys. Rev. B* 102 (22 2020), p. 224101. DOI: 10.1103/PhysRevB.102.224101.

[31] T. Castaing-Cordier, D. Bouillaud, J. Farjon, and P. Giraudeau. "Chapter Four - Recent advances in benchtop NMR spectroscopy and its applications." In: ed. by G. A. Webb. Vol. 103. Annual Reports on NMR Spectroscopy. Academic Press, 2021, pp. 191–258. DOI: 10.1016/bs.arnmr.2021.02.003.

[32] A. Chanuntranont et al. "Real-Time Nuclear Magnetic Resonance Detection Using Maximum Likelihood Estimation with Single-Shallow-Nitrogen-Vacancy Centers in Quantum Heterodyne Measurements." In: *physica status solidi (a)* (), p. 2400307. DOI: 10.1002/pssa.202400307.

[33] P. Chrostoski, B. Barrios, and D. Santamore. “Magnetic field noise analyses generated by the interactions between a nitrogen vacancy center diamond and surface and bulk impurities.” In: *Physica B: Condensed Matter* 605 (2021), p. 412767. DOI: 10.1016/j.physb.2020.412767.

[34] T. L. Cocker, D. Peller, P. Yu, J. Repp, and R. Huber. “Tracking the ultrafast motion of a single molecule by femtosecond orbital imaging.” In: *Nature* 539 (2016), 263–267. DOI: 10.1038/nature19816.

[35] D. Cohen, R. Nigmatullin, M. Eldar, and A. Retzker. “Confined Nano-NMR Spectroscopy Using NV Centers.” In: *Advanced Quantum Technologies* 3.11 (2020), p. 2000019. DOI: 10.1002/qute.202000019.

[36] J. Croese et al. “High-accuracy liquid-sample -NMR setup at ISOLDE.” In: *Nuclear Instruments and Methods in Physics Research Section A: Accelerators, Spectrometers, Detectors and Associated Equipment* 1020 (2021), p. 165862. DOI: 10.1016/j.nima.2021.165862.

[37] L. Cywinski, R. M. Lutchyn, C. P. Nave, and S. Das Sarma. “How to enhance dephasing time in superconducting qubits.” In: *Phys. Rev. B* 77 (17 2008), p. 174509. DOI: 10.1103/PhysRevB.77.174509.

[38] G. Davies, M. F. Hamer, and W. C. Price. “Optical studies of the 1.945 eV vibronic band in diamond.” In: *Proceedings of the Royal Society of London. A. Mathematical and Physical Sciences* 348.1653 (1976), pp. 285–298. DOI: 10.1098/rspa.1976.0039.

[39] N. De Zanche, C. Barmet, J. A. Nordmeyer-Massner, and K. P. Pruessmann. “NMR probes for measuring mag-

netic fields and field dynamics in MR systems." In: *Magnetic Resonance in Medicine* 60.1 (2008), pp. 176–186. DOI: 10.1002/mrm.21624.

[40] S. J. DeVience et al. "Nanoscale NMR spectroscopy and imaging of multiple nuclear species." In: *Nature Nanotech.* 10 (2015), pp. 129–134. DOI: 10.1038/nnano.2014.313.

[41] R. M. Dickson, D. J. Norris, Y.-L. Tzeng, and W. E. Moerner. "Three-Dimensional Imaging of Single Molecules Solvated in Pores of Poly(acrylamide) Gels." In: *Science* 274.5289 (1996), pp. 966–968. DOI: 10.1126/science.274.5289.966.

[42] M. W. Doherty, N. B. Manson, P. Delaney, F. Jelezko, J. Wrachtrup, and L. C. Hollenberg. "The nitrogen-vacancy colour centre in diamond." In: *Physics Reports* 528.1 (2013), pp. 1–45. DOI: 10.1016/j.physrep.2013.02.001.

[43] Y. Doi et al. "Deterministic Electrical Charge-State Initialization of Single Nitrogen-Vacancy Center in Diamond." In: *Phys. Rev. X* 4 (1 2014), p. 011057. DOI: 10.1103/PhysRevX.4.011057.

[44] A. Dréau, P. Jamonneau, O. Gazzano, S. Kosen, J.-F. Roch, J. R. Maze, and V. Jacques. "Probing the Dynamics of a Nuclear Spin Bath in Diamond through Time-Resolved Central Spin Magnetometry." In: *Phys. Rev. Lett.* 113.13 (2014), p. 137601. DOI: 10.1103/PhysRevLett.113.137601.

[45] J. Du, F. Shi, X. Kong, F. Jelezko, and J. Wrachtrup. "Single-molecule scale magnetic resonance spectroscopy using quantum diamond sensors." In: *Rev. Mod. Phys.* 96 (2 2024), p. 025001. DOI: 10.1103/RevModPhys.96.025001.

[46] M. J. Duer. *ISolid State NMR Spectroscopy: Principles and Applications*. Wiley-Blackwell, 2008.

[47] J. Eills, W. Hale, and M. Utz. "Synergies between Hyperpolarized NMR and Microfluidics: A Review." In: *Progress in Nuclear Magnetic Resonance Spectroscopy* 128 (2022), pp. 44–69. DOI: 10.1016/j.pnmrs.2021.09.001.

[48] R. J. Epstein, F. M. Mendoza, Y. K. Kato, and D. D. Awschalom. "Anisotropic interactions of a single spin and dark-spin spectroscopy in diamond." In: *Nature Physics* 1.2 (2005), pp. 94–98. DOI: 10.1038/nphys141.

[49] R. R. Ernst, G. Bodenhausen, and A. Wokaun. *Principles of Nuclear Magnetic Resonance in One and Two Dimensions*. Oxford University Press, 1990.

[50] N. Eshuis, N. Hermkens, B. J. A. van Weerdenburg, M. C. Feiters, F. P. J. T. Rutjes, S. S. Wijmenga, and M. Tessari. "Toward Nanomolar Detection by NMR Through SABRE Hyperpolarization." In: *Journal of the American Chemical Society* 136.7 (2014), pp. 2695–2698. DOI: 10.1021/ja412994k.

[51] D. Farfurnik, A. Jarmola, L. M. Pham, Z. H. Wang, V. V. Dobrovitski, R. L. Walsworth, D. Budker, and N. Bar-Gill. "Optimizing a dynamical decoupling protocol for solid-state electronic spin ensembles in diamond." In: *Phys. Rev. B* 92 (6 2015), p. 060301. DOI: 10.1103/PhysRevB.92.060301.

[52] R. M. Fratila, M. V. Gomez, S. Sýkora, and A. H. Velders. "Multinuclear nanoliter one-dimensional and two-dimensional NMR spectroscopy with a single non-resonant micro-

coil.” In: *Nature Communications* 5.1 (2014), p. 3025. DOI: 10.1038/ncomms4025.

[53] R. Frisch and O. Stern. “Über die magnetische Ablenkung von Wasserstoffmolekülen und das magnetische Moment des Protons. I.” In: *Zeitschrift für Physik* 85.1 (1933), pp. 4–16. DOI: 10.1007/BF01330773.

[54] M. Gai, J. Frueh, T. Tao, A. V. Petrov, V. V. Petrov, E. V. Shesterikov, S. I. Tverdokhlebov, and G. B. Sukhorukov. “Polylactic acid nano- and microchamber arrays for encapsulation of small hydrophilic molecules featuring drug release via high intensity focused ultrasound.” In: *Nanoscale* 9 (21 2017), pp. 7063–7070. DOI: 10.1039/C7NR01841J.

[55] P. Garbacz. “Computations of the chirality-sensitive effect induced by an antisymmetric indirect spin–spin coupling.” In: *Molecular Physics* 116.10 (2018), pp. 1397–1408. DOI: 10.1080/00268976.2018.1432904.

[56] A. Garcon et al. “Constraints on bosonic dark matter from ultralow-field nuclear magnetic resonance.” In: *Science Advances* 5.10 (2019), eaax4539. DOI: 10.1126/sciadv.aax4539.

[57] W. Gerlach and O. Stern. “Der experimentelle Nachweis der Richtungsquantelung im Magnetfeld.” In: *Zeitschrift für Physik* 9.1 (1922), pp. 349–352. DOI: 10.1007/BF01326983.

[58] S. Ghimire, S.-J. Lee, S. Oh, and J. H. Shim. “Frequency Limits of Sequential Readout for Sensing AC Magnetic Fields Using Nitrogen-Vacancy Centers in Diamond.” In: *Sensors* 23.17 (7566 2023). DOI: 10.3390/s23177566.

[59] A. K. Ghosh and S. Gemma. *Structure-Based Design of Drugs and Other Bioactive Molecules: Tools and Strategies*. Wiley-VCH, 2014.

[60] D. R. Glenn, D. B. Bucher, J. Lee, M. D. Lukin, H. Park, and R. L. Walsworth. "High-resolution magnetic resonance spectroscopy using a solid-state spin sensor." In: *Nature* 555.7696 (2018), pp. 351–354. DOI: `10.1038/nature25781`.

[61] F. Gorrini and A. Bifone. "Advances in Stabilization and Enrichment of Shallow Nitrogen-Vacancy Centers in Diamond for Biosensing and Spin-Polarization Transfer." In: *Biosensors* 13.7 (2023). DOI: `10.3390/bios13070691`.

[62] N. R. von Grafenstein, K. D. Briegel, J. Casanova, and D. B. Bucher. *Coherent signal detection in the statistical polarization regime enables high-resolution nanoscale NMR spectroscopy*. 2025. DOI: `10.48550/arXiv.2501.02093`.

[63] R. A. Green, R. W. Adams, S. B. Duckett, R. E. Mewis, D. C. Williamson, and G. G. Green. "The theory and practice of hyperpolarization in magnetic resonance using parahydrogen." In: *Progress in Nuclear Magnetic Resonance Spectroscopy* 67 (2012), pp. 1–48. DOI: `10.1016/j.pnmrs.2012.03.001`.

[64] M. Grisi, G. M. Conley, K. J. Rodriguez, E. Riva, L. Egli, W. Moritz, J. Lichtenberg, J. Brugger, and G. Boero. "NMR microsystem for label-free characterization of 3D nanoliter microtissues." In: *Scientific Reports* 10.1 (2020), p. 18306. DOI: `10.1038/s41598-020-75480-0`.

[65] K. Groot-Berning, G. Jacob, C. Osterkamp, F. Jelezko, and F. Schmidt-Kaler. "Fabrication of 15NV centers in diamond using a deterministic single ion implanter." In:

New Journal of Physics 23.6 (2021), p. 063067. DOI: 10.1088/1367-2630/ac0753.

[66] B. Gruber, M. Froeling, T. Leiner, and D. W. Klomp. “RF coils: A practical guide for nonphysicists.” In: *Journal of Magnetic Resonance Imaging* 48.3 (2018), pp. 590–604. DOI: /10.1002/jmri.26187.

[67] M. Gulka, D. Wirtitsch, V. Ivády, J. Vodnik, J. Hruby, G. Magchiels, E. Bourgeois, A. Gali, M. Trupke, and M. Nesladek. “Room-temperature control and electrical readout of individual nitrogen-vacancy nuclear spins.” In: *Nat Commun.* 12 (2021), p. 4421. DOI: 10.1038/s41467-021-24494-x.

[68] H. Gunther. *NMR Spectroscopy: Basic Principles, Concepts and Applications in Chemistry*. Wiley-VCH, 2013.

[69] A. Gupta, L. Hacquebard, and L. Childress. “Efficient signal processing for time-resolved fluorescence detection of nitrogen-vacancy spins in diamond.” In: *J. Opt. Soc. Am. B* 33 (3 2016), B28–B34. DOI: 10.1364/JOSAB.33.000B28.

[70] E. L. Hahn. “Spin Echoes.” In: *Phys. Rev.* 80 (4 1950), pp. 580–594. DOI: 10.1103/PhysRev.80.580.

[71] L. T. Hall, P. Kehayias, D. A. Simpson, A. Jarmola, A. Stacey, D. Budker, and L. C. L. Hollenberg. “Detection of nanoscale electron spin resonance spectra demonstrated using nitrogen-vacancy centre probes in diamond.” In: *Nat. Commun.* 7 (2016), p. 10211. DOI: 10.1038/ncomms10211.

[72] P. Hemnani, G. Joshi, A. Rajarajan, and S. Ravindranath. “14N NQR spectrometer for explosive detection: A review.” In: *2016 International Conference on Automatic Con-*

trol and Dynamic Optimization Techniques (ICACDOT). 2016, pp. 1120–1125. DOI: 10.1109/ICACDOT.2016.7877761.

[73] E. Herbschleb et al. “Ultra-long coherence times amongst room-temperature solid-state spins.” In: *Nat Commun* 10.3766 (2019). DOI: 10.1038/s41467-019-11776-8.

[74] K. Herouz, H. Laidoudi, A. Aissa, A. Mourad, K. Guedri, M. Oreijah, and O. Younis. “Analysis of nano-encapsulated phase change material confined in a double lid-driven hexagonal porous chamber with an obstacle under magnetic field.” In: *Journal of Energy Storage* 61 (2023), p. 106736. DOI: 10.1016/j.est.2023.106736.

[75] H. D. W. Hill and R. E. Richards. “Limits of measurement in magnetic resonance.” In: *Journal of Physics E: Scientific Instruments* 1.10 (1968), p. 977. DOI: 10.1088/0022-3735/1/10/202.

[76] L. Horsthemke, J. Pogorzelski, D. Stiegekötter, F. Hoffmann, L. Langguth, R. Staacke, C. Laube, W. Knolle, M. Gregor, and P. Glösekötter. “Excited-State Lifetime of NV Centers for All-Optical Magnetic Field Sensing.” In: *Sensors* 24.7 (2024). DOI: 10.3390/s24072093.

[77] D. Hoult and R. Richards. “The signal-to-noise ratio of the nuclear magnetic resonance experiment.” In: *Journal of Magnetic Resonance* 213.2 (2011), pp. 329–343. DOI: 10.1016/j.jmr.2011.09.018.

[78] K. Iakoubovskii, I. Kiflawi, K. Johnston, A. Collins, G. Davies, and A. Stesmans. “Annealing of vacancies and interstitials in diamond.” In: *Physica B: Condensed Matter* 340-342 (2003). Proceedings of the 22nd International

Conference on Defects in Semiconductors, pp. 67–75. DOI: 10.1016/j.physb.2003.09.005.

[79] E. Janitz, K. Herb, L. A. Völker, W. S. Huxter, C. L. Degen, and J. M. Abendroth. "Diamond surface engineering for molecular sensing with nitrogen—vacancy centers." In: *J. Mater. Chem. C* 10 (37 2022), pp. 13533–13569. DOI: 10.1039/D2TC01258H.

[80] F. Jelezko, T. Gaebel, I. Popa, M. Domhan, A. Gruber, and J. Wrachtrup. "Observation of Coherent Oscillation of a Single Nuclear Spin and Realization of a Two-Qubit Conditional Quantum Gate." In: *Phys. Rev. Lett.* 93 (13 2004), p. 130501. DOI: 10.1103/PhysRevLett.93.130501.

[81] H.-S. Jung and K. C. Neuman. "Surface Modification of Fluorescent Nanodiamonds for Biological Applications." In: *Nanomaterials* 11.1 (2021). DOI: 10.3390/nano11010153.

[82] P. Kehayias et al. "Solution nuclear magnetic resonance spectroscopy on a nanostructured diamond chip." In: *Nature Communications* 8.1 (2017), p. 188. DOI: 10.1038/s41467-017-00266-4.

[83] A. S. Khan et al. "Enabling Clinical Technologies for Hyperpolarized 129Xenon Magnetic Resonance Imaging and Spectroscopy." In: *Angewandte Chemie International Edition* 60.41 (2021), pp. 22126–22147. DOI: 10.1002/anie.202015200.

[84] M. Kim, H. J. Mamin, M. H. Sherwood, K. Ohno, D. D. Awschalom, and D. Rugar. "Decoherence of Near-Surface Nitrogen-Vacancy Centers Due to Electric Field Noise." In: *Phys. Rev. Lett.* 115 (8 2015), p. 087602. DOI: 10.1103/PhysRevLett.115.087602.

[85] J. P. King, T. F. Sjolander, and J. W. Blanchard. “Antisymmetric Couplings Enable Direct Observation of Chirality in Nuclear Magnetic Resonance Spectroscopy.” In: *The Journal of Physical Chemistry Letters* 8.4 (2017), pp. 710–714. DOI: 10.1021/acs.jpclett.6b02653.

[86] H. Kisch. “Semiconductor Photocatalysis—Mechanistic and Synthetic Aspects.” In: *Angew. Chem.* 52 (3 2013), pp. 812–847. DOI: 10.1002/anie.201201200.

[87] G. Kucsko, P. C. Maurer, N. Y. Yao, M. Kubo, H. J. Noh, P. K. Lo, H. Park, and M. D. Lukin. “Nanometre-scale thermometry in a living cell.” In: *Nature* 500 (2013), pp. 54–58. DOI: 10.1038/nature12373.

[88] A. Kumar, D. Welti, and R. R. Ernst. “NMR Fourier zeugmatography.” In: *Journal of Magnetic Resonance (1969)* 18.1 (1975), pp. 69–83. DOI: 10.1016/0022-2364(75)90224-3.

[89] R. Kumar et al. “Stability of Near-Surface Nitrogen Vacancy Centers Using Dielectric Surface Passivation.” In: *ACS Photonics* 11.3 (2024), pp. 1244–1251. DOI: 10.1021/acsphotonics.3c01773.

[90] P. C. LAUTERBUR. “Image Formation by Induced Local Interactions: Examples Employing Nuclear Magnetic Resonance.” In: *Nature* 242.5394 (1973), pp. 190–191. DOI: 10.1038/242190a0.

[91] G. de Lange, Z. H. Wang, D. Ristè, V. V. Dobrovitski, and R. Hanson. “Universal Dynamical Decoupling of a Single Solid-State Spin from a Spin Bath.” In: *Science* 330.6000 (2010), pp. 60–63. DOI: 10.1126/science.1192739.

[92] R. Langer and D. A. Tirrell. "Designing materials for biology and medicine." In: *Nature* 428 (2004), pp. 487–492. DOI: `10.1038/nature02388`.

[93] J. H. Lee, Y. Okuno, and S. Cavagnero. "Sensitivity enhancement in solution NMR: Emerging ideas and new frontiers." In: *Journal of Magnetic Resonance* 241 (2014). A special "JMR Perspectives" issue: Foresights in Biomolecular Solution-State NMR Spectroscopy – From Spin Gymnastics to Structure and Dynamics, pp. 18–31. DOI: `10.1016/j.jmr.2014.01.005`.

[94] M. H. Levitt. *Spin Dynamics: Basics of Nuclear Magnetic Resonance*. Wiley, 2008.

[95] Y. Lin, Q. Zeng, L. Lin, Z. Chen, and P. B. Barker. "High-resolution methods for the measurement of scalar coupling constants." In: *Progress in Nuclear Magnetic Resonance Spectroscopy* 109 (2018), pp. 135–159. DOI: `10.1016/j.pnmrs.2018.08.003`.

[96] K. S. Liu, A. Henning, M. W. Heindl, R. D. Allert, J. D. Bartl, I. D. Sharp, R. Rizzato, and D. B. Bucher. "Surface NMR using quantum sensors in diamond." In: *PNAS* 119 (5 2021), e2111607119. DOI: `10.1073/pnas.2111607119`.

[97] K. S. Liu, X. Ma, R. Rizzato, A. L. Semrau, A. Henning, I. D. Sharp, R. A. Fischer, and D. B. Bucher. "Using Metal–Organic Frameworks to Confine Liquid Samples for Nanoscale NV-NMR." In: *Nano Letters* 22.24 (2022), pp. 9876–9882. DOI: `10.1021/acs.nanolett.2c03069`.

[98] Y.-X. Liu, A. Ajoy, and P. Cappellaro. "Nanoscale Vector dc Magnetometry via Ancilla-Assisted Frequency Up-

Conversion." In: *Phys. Rev. Lett.* 122 (10 2019), p. 100501. DOI: 10.1103/PhysRevLett.122.100501.

[99] D. Louzon, G. T. Genov, N. Staudenmaier, F. Frank, J. Lang, M. L. Markham, A. Retzker, and F. Jelezko. *Robust Noise Suppression and Quantum Sensing by Continuous Phased Dynamical Decoupling*. 2024.

[100] I. Lovchinsky et al. "Nuclear magnetic resonance detection and spectroscopy of single proteins using quantum logic." In: *Science* 351.6275 (2016), pp. 836–841. DOI: 10.1126/science.aad8022.

[101] A. Lozovoi, H. Jayakumar, D. Daw, G. Vizkelethy, E. Bielejec, M. W. Doherty, J. Flick, and C. A. Meriles. "Optical activation and detection of charge transport between individual colour centres in diamond." In: *Nature Electronics* 4.10 (2021), pp. 717–724. DOI: 10.1038/s41928-021-00656-z.

[102] T Luo et al. "Creation of nitrogen-vacancy centers in chemical vapor deposition diamond for sensing applications." In: *New Journal of Physics* 24.3 (2022), p. 033030. DOI: 10.1088/1367-2630/ac58b6.

[103] D. E. MacLaughlin. "Magnetic Resonance in the Superconducting State." In: vol. 31. Solid State Physics. Academic Press, 1976, pp. 1–69. DOI: 10.1016/S0081-1947(08)60541-X.

[104] R. S. Macomber. *A Complete Introduction to Modern NMR Spectroscopy*. Wiley-Interscience, 1997.

[105] P. Maletinsky, S. Hong, M. S. Grinolds, B. Hausmann, M. D. Lukin, R. L. Walsworth, M. Loncar, and A. Yacoby. "A robust scanning diamond sensor for nanoscale

imaging with single nitrogen-vacancy centres." In: *Nature Nanotechnology* 7.5 (2012), pp. 320–324. DOI: 10.1038/nnano.2012.50.

[106] H. J. Mamin, M. Kim, M. H. Sherwood, C. T. Rettner, K. Ohno, D. D. Awschalom, and D. Rugar. "Nanoscale Nuclear Magnetic Resonance with a Nitrogen-Vacancy Spin Sensor." In: *Science* 339.6119 (2013), pp. 557–560. DOI: 10.1126/science.1231540.

[107] P Mansfield and A. A. Maudsley. "Planar spin imaging by NMR." In: *Journal of Physics C: Solid State Physics* 9.15 (1976), p. L409. DOI: 10.1088/0022-3719/9/15/004.

[108] N. B. Manson, J. P. Harrison, and M. J. Sellars. "Nitrogen-vacancy center in diamond: Model of the electronic structure and associated dynamics." In: *Phys. Rev. B* 74 (10 2006), p. 104303. DOI: 10.1103/PhysRevB.74.104303.

[109] N. Manson and J. Harrison. "Photo-ionization of the nitrogen-vacancy center in diamond." In: *Diamond and Related Materials* 14.10 (2005), pp. 1705–1710. DOI: 10.1016/j.diamond.2005.06.027.

[110] J. M. McCoey, M. Matsuoka, R. W. de Gille, L. T. Hall, J. A. Shaw, J.-P. Tetienne, D. Kisailus, L. C. L. Hollenberg, and D. A. Simpson. "Quantum Magnetic Imaging of Iron Biomineralization in Teeth of the Chiton Acanthopleura hirtosa." In: *Small Methods* 4.3 (2020), p. 1900754. DOI: 10.1002/smtd.201900754.

[111] D. Merker, D. Bertinetti, R. Merz, M. Kopnarski, F. W. Herberg, and C. Popov. "Enhanced protein immobilization efficacy by nanostructuring of ultrananocrystalline

diamond surface." In: *Diamond and Related Materials* 136 (2023), p. 109898. DOI: 10.1016/j.diamond.2023.109898.

[112] V. K. Michaelis, R. G. Griffin, B. Corzilius, and S. Vega. *Handbook of High Field Dynamic Nuclear Polarization*. Wiley, 2020.

[113] V. K. Michaelis, R. G. Griffin, B. Corzilius, and S. Vega. *Handbook of High Field Dynamic Nuclear Polarization*. Wiley, 2020.

[114] M. Mrozek, J. Mlynarczyk, D. S. Rudnicki, and W. Gawlik. "Circularly polarized microwaves for magnetic resonance study in the GHz range: Application to nitrogen-vacancy in diamonds." In: *Applied Physics Letters* 107.1 (July 2015), p. 013505. DOI: 10.1063/1.4923252.

[115] C. Muller et al. "Nuclear magnetic resonance spectroscopy with single spin sensitivity." In: *Nature Commun.* 5 (2014), p. 4703. DOI: 10.1038/ncomms5703.

[116] B. A. Myers, A. Das, M. C. Dartiailh, K. Ohno, D. D. Awschalom, and A. C. Bleszynski Jayich. "Probing Surface Noise with Depth-Calibrated Spins in Diamond." In: *Phys. Rev. Lett.* 113 (2 2014), p. 027602. DOI: 10.1103/PhysRevLett.113.027602.

[117] J. Z. Myers et al. "Zero to ultralow magnetic field NMR of [$1-^{13}$C]pyruvate and [$2-^{13}$C]pyruvate enabled by SQUID sensors and hyperpolarization." In: *Phys. Rev. B* 109 (18 2024), p. 184443. DOI: 10.1103/PhysRevB.109.184443.

[118] Y. Nakamura, H. Watanabe, H. Sumiya, K. M. Itoh, K. Sasaki, J. Ishi-Hayase, and K. Kobayashi. "Optimization of optical spin readout of the nitrogen-vacancy center

in diamond based on spin relaxation model." In: *AIP Advances* 12.5 (2022), p. 055215. DOI: `10.1063/5.0090450`.

[119] B. Naydenov, F. Reinhard, A. Lämmle, V. Richter, R. Kalish, U. F. S. D'Haenens-Johansson, M. Newton, F. Jelezko, and J. Wrachtrup. "Increasing the coherence time of single electron spins in diamond by high temperature annealing." In: *Applied Physics Letters* 97.24 (Dec. 2010), p. 242511. DOI: `10.1063/1.3527975`.

[120] N. R. Neuling, R. D. Allert, and D. B. Bucher. "Prospects of single-cell nuclear magnetic resonance spectroscopy with quantum sensors." In: *Current Opinion in Biotechnology* 83 (2023), p. 102975. DOI: `10.1016/j.copbio.2023.102975`.

[121] P Neumann et al. "Excited-state spectroscopy of single NV defects in diamond using optically detected magnetic resonance." In: *New Journal of Physics* 11.1 (2009), p. 013017. DOI: `10.1088/1367-2630/11/1/013017`.

[122] K. Ohno, F. Joseph Heremans, L. C. Bassett, B. A. Myers, D. M. Toyli, A. C. Bleszynski Jayich, C. J. Palmstrøm, and D. D. Awschalom. "Engineering shallow spins in diamond with nitrogen delta-doping." In: *Applied Physics Letters* 101.8 (2012), p. 082413. DOI: `10.1063/1.4748280`.

[123] D. L. Olson, T. L. Peck, A. G. Webb, R. L. Magin, and J. V. Sweedler. "High-Resolution Microcoil ^{1}H-NMR for Mass-Limited, Nanoliter-Volume Samples." In: *Science* 270 (5244 1995), pp. 1967–1970. DOI: `10.1126/science.270.5244.1967`.

[124] E van Oort, N. B. Manson, and M Glasbeek. "Optically detected spin coherence of the diamond N-V centre in

its triplet ground state." In: *Journal of Physics C: Solid State Physics* 21.23 (1988), p. 4385. DOI: `10.1088/0022-3719/21/23/020`.

[125] D. Pagliero, R. Khan, K. Elkaduwe, A. Bhardwaj, K. Xu, A. Wolcott, G. E. López, B. Radha, N. Giovambattista, and C. A. Meriles. "Slow Water in Engineered Nanochannels Revealed by Color-Center-Enabled Sensing." In: *Nano Letters* 25.25 (2025), pp. 9960–9966. DOI: `10.1021/acs.nanolett.5c01344`.

[126] S. Pal. *Fundamentals of Molecular Structural Biology*. Academic Press, 2019.

[127] V. S. Perunicic, L. T. Hall, D. A. Simpson, C. D. Hill, and L. C. L. Hollenberg. "Towards single-molecule NMR detection and spectroscopy using single spins in diamond." In: *Phys. Rev. B* 89 (5 2014), p. 054432. DOI: `10.1103/PhysRevB.89.054432`.

[128] M. D. Pinter, T. Harter, M. J. McCarthy, and M. P. Augustine. "Towards Using NMR to Screen for Spoiled Tomatoes Stored in 1,000 L, Aseptically Sealed, Metal-Lined Totes." In: *Sensors* 14.3 (2014), pp. 4167–4176. DOI: `10.3390/s140304167`.

[129] E. M. Purcell, H. C. Torrey, and R. V. Pound. "Resonance Absorption by Nuclear Magnetic Moments in a Solid." In: *Phys. Rev.* 69 (1-2 1946), pp. 37–38. DOI: `10.1103/PhysRev.69.37`.

[130] P. Put, S. Pustelny, D. Budker, E. Druga, T. F. Sjolander, A. Pines, and D. A. Barskiy. "Zero- to Ultralow-Field NMR Spectroscopy of Small Biomolecules." In: *Analyti-*

cal Chemistry 93.6 (2021). PMID: 33448215, pp. 3226–3232. DOI: 10.1021/acs.analchem.0c04738.

[131] P. Qian, X. Lin, F. Zhou, R. Ye, Y. Ji, B. Chen, G. Xie, and N. Xu. “Machine-learning-assisted electron-spin readout of nitrogen-vacancy center in diamond.” In: *Applied Physics Letters* 118.8 (2021), p. 084001. DOI: 10.1063/5.0038590.

[132] J. R. Rabeau, P. Reichart, G. Tamanyan, D. N. Jamieson, S. Prawer, F. Jelezko, T. Gaebel, I. Popa, M. Domhan, and J. Wrachtrup. “Implantation of labelled single nitrogen vacancy centers in diamond using N15.” In: *Applied Physics Letters* 88.2 (Jan. 2006), p. 023113. DOI: 10.1063/1.2158700.

[133] I. I. Rabi, J. R. Zacharias, S. Millman, and P. Kusch. “A New Method of Measuring Nuclear Magnetic Moment.” In: *Phys. Rev.* 53 (4 1938), pp. 318–318. DOI: 10.1103/PhysRev.53.318.

[134] L. Razinkovas, M. Maciaszek, F. Reinhard, M. W. Doherty, and A. Alkauskas. “Photoionization of negatively charged NV centers in diamond: Theory and ab initio calculations.” In: *Phys. Rev. B* 104 (23 2021), p. 235301. DOI: 10.1103/PhysRevB.104.235301.

[135] R. Rizzato, N. R. von Grafenstein, and D. B. Bucher. “Quantum sensors in diamonds for magnetic resonance spectroscopy: Current applications and future prospects.” In: *Applied Physics Letters* 123.26 (Dec. 2023), p. 260502. DOI: 10.1063/5.0169027.

[136] L. Robledo, H. Bernien, I. van Weperen, and R. Hanson. “Control and Coherence of the Optical Transition of Single Nitrogen Vacancy Centers in Diamond.” In:

Phys. Rev. Lett. 105 (17 2010), p. 177403. DOI: `10.1103/PhysRevLett.105.177403`.

[137] S. Sangtawesin et al. "Origins of Diamond Surface Noise Probed by Correlating Single-Spin Measurements with Surface Spectroscopy." In: *Phys. Rev. X* 9 (3 2019), p. 031052. DOI: `10.1103/PhysRevX.9.031052`.

[138] I. Savukov, H.-Y. Chen, T. Karaulanov, and C. Hilty. "Method for accurate measurements of nuclear-spin optical rotation for applications in correlated optical-NMR spectroscopy." In: *Journal of Magnetic Resonance* 232 (2013), pp. 31–38. DOI: `10.1016/j.jmr.2013.04.008`.

[139] S. C. Schmitt. "Nanoscale magnetic spectroscopy with colour centres in diamond." PhD thesis. Uni Ulm, Aug. 2021. DOI: `10.18725/OPARU-38599`.

[140] S. Schmitt et al. "Submillihertz magnetic spectroscopy performed with a nanoscale quantum sensor." In: *Science* 356.6340 (2017), pp. 832–837. DOI: `10.1126/science.aam5532`.

[141] H. Schneckenburger and V. Richter. "Laser Scanning versus Wide-Field—Choosing the Appropriate Microscope in Life Sciences." In: *Applied Sciences* 11.2 (2021). DOI: `10.3390/app11020733`.

[142] I. Schnell and H. W. Spiess. "High-Resolution 1H NMR Spectroscopy in the Solid State: Very Fast Sample Rotation and Multiple-Quantum Coherences." In: *Journal of Magnetic Resonance* 151.2 (2001), pp. 153–227. DOI: `10.1006/jmre.2001.2336`.

[143] S. C. Scholten, A. J. Healey, I. O. Robertson, G. J. Abrahams, D. A. Broadway, and J.-P. Tetienne. "Widefield quantum microscopy with nitrogen-vacancy centers in diamond: Strengths, limitations, and prospects." In: *Journal of Applied Physics* 130.15 (Oct. 2021), p. 150902. DOI: `10.1063/5.0066733`.

[144] I. Schwartz, J. Rosskopf, S. Schmitt, B. Tratzmiller, Q. Chen, L. P. McGuinness, F. Jelezko, and M. B. Plenio. "Blueprint for nanoscale NMR." In: *Scientific Reports* 9.1 (2019), p. 6938. DOI: `10.1038/s41598-019-43404-2`.

[145] H. M. Sevian and J. L. Skinner. "T2 can be greater than 2T1." In: *The Journal of Chemical Physics* 91.3 (Aug. 1989), pp. 1775–1782. DOI: `10.1063/1.457648`.

[146] B. J. Shields, Q. P. Unterreithmeier, N. P. de Leon, H. Park, and M. D. Lukin. "Efficient Readout of a Single Spin State in Diamond via Spin-to-Charge Conversion." In: *Phys. Rev. Lett.* 114 (13 2015), p. 136402. DOI: `10.1103/PhysRevLett.114.136402`.

[147] D. Smith and P. Spanel. "Selected ion flow tube mass spectrometry (SIFT-MS) for on-line trace gas analysis." In: *Mass Spectrom. Rev.* 24 (5 2005), pp. 661–700. DOI: `10.1002/mas.20033`.

[148] J. A. S. Smith. "Nuclear quadrupole resonance spectroscopy. General principles." In: *Journal of Chemical Education* 48.1 (1971), p. 39. DOI: `10.1021/ed048p39`.

[149] S. A. Smith, W. E. Palke, and J. T. Gerig. "The Hamiltonians of NMR. Part II." In: *Concepts in Magnetic Resonance* 4.3 (), pp. 181–204. DOI: `10.1002/cmr.1820040302`.

[150] S. A. Smith, W. E. Palke, and J. T. Gerig. "The Hamiltonians of NMR. part I." In: *Concepts in Magnetic Resonance* 4.2 (1992), pp. 107–144. DOI: 10.1002/cmr.1820040202.

[151] J. Smits, J. T. Damron, P. Kehayias, A. F. McDowell, N. Mosavian, I. Fescenko, N. Ristoff, A. Laraoui, A. Jarmola, and V. M. Acosta. "Two-dimensional nuclear magnetic resonance spectroscopy with a microfluidic diamond quantum sensor." In: *Science Advances* 5.7 (2019), eaaw7895. DOI: 10.1126/sciadv.aaw7895.

[152] T. Staudacher, F. Shi, S. Pezzagna, J. Meijer, J. Du, C. A. Meriles, F. Reinhard, and J. Wrachtrup. "Nuclear Magnetic Resonance Spectroscopy on a (5-Nanometer)^3 Sample Volume." In: *Science* 339.6119 (2013), pp. 561–563. DOI: 10.1126/science.1231675.

[153] N. Staudenmaier et al. "Power-law scaling of correlations in statistically polarised nano-NMR." In: *npj Quantum Information* 8.1 (2022), p. 120. DOI: 10.1038/s41534-022-00632-1.

[154] S. Steinert, F. Ziem, L. T. Hall, A. Zappe, M. Schweikert, N. Götz, A. Aird, G. Balasubramanian, L. Hollenberg, and J. Wrachtrup. "Magnetic spin imaging under ambient conditions with sub-cellular resolution." In: *Nature Communications* 4.1 (2013), p. 1607. DOI: 10.1038/ncomms2588.

[155] Q. Stern, Q. Reynard-Feytis, S. J. Elliott, M. Ceillier, O. Cala, K. Ivanov, and S. Jannin. "Rapid and Simple 13C-Hyperpolarization by 1H Dissolution Dynamic Nuclear Polarization Followed by an Inline Magnetic Field Inver-

sion.” In: *Journal of the American Chemical Society* 145.50 (2023), pp. 27576–27586. DOI: 10.1021/jacs.3c09209.

[156] A. O. Sushkov, I. Lovchinsky, N. Chisholm, R. L. Walsworth, H. Park, and M. D. Lukin. “Magnetic Resonance Detection of Individual Proton Spins Using Quantum Reporters.” In: *Phys. Rev. Lett.* 113 (19 2014), p. 197601. DOI: 10.1103/PhysRevLett.113.197601.

[157] P. Tamarat et al. “Spin-flip and spin-conserving optical transitions of the nitrogen-vacancy centre in diamond.” In: *New Journal of Physics* 10.4 (2008), p. 045004. DOI: 10.1088/1367-2630/10/4/045004.

[158] S. Tanaka. “Chapter One - Recent advances in dynamic nuclear polarization-enhanced NMR spectroscopy for organic polymers.” In: ed. by G. A. Webb. Vol. 105. Annual Reports on NMR Spectroscopy. Academic Press, 2022, pp. 1–46. DOI: 10.1016/bs.arnmr.2021.06.002.

[159] F. Taulelle. “NMR crystallography: crystallochemical formula and space group selection.” In: *Solid State Sciences* 6.10 (2004). Thematic section: NMR crystallography, pp. 1053–1057. DOI: 10.1016/j.solidstatesciences.2004.07.033.

[160] J. M. Taylor, P. Cappellaro, L. Childress, L. Jiang, D. Budker, P. R. Hemmer, A. Yacoby, R. Walsworth, and M. D. Lukin. “High-sensitivity diamond magnetometer with nanoscale resolution.” In: *Nature Phys.* 4 (2008), 810–816. DOI: 10.1038/nphys1075.

[161] J.-P. Tetienne, L Rondin, P Spinicelli, M Chipaux, T Debuisschert, J.-F. Roch, and V Jacques. “Magnetic-field-dependent photodynamics of single NV defects in dia-

mond: an application to qualitative all-optical magnetic imaging." In: *New Journal of Physics* 14.10 (2012), p. 103033. DOI: `10.1088/1367-2630/14/10/103033`.

[162] J.-P. Tetienne et al. "Spin properties of dense near-surface ensembles of nitrogen-vacancy centers in diamond." In: *Phys. Rev. B* 97 (8 2018), p. 085402. DOI: `10.1103/PhysRevB.97.085402`.

[163] J.-P. Tetienne, N. Dontschuk, D. A. Broadway, A. Stacey, D. A. Simpson, and L. C. L. Hollenberg. "Quantum imaging of current flow in graphene." In: *Science Advances* 3.4 (2017), e1602429. DOI: `10.1126/sciadv.1602429`.

[164] Y. Tian and K. Larsson. "Protein-Functionalized Diamond Surfaces in a Water Solvent: A Theoretical Approach." In: *The Journal of Physical Chemistry C* 119.16 (2015), pp. 8608–8618. DOI: `10.1021/jp511015m`.

[165] J. Vıcha, J. Novotny, S. Komorovsky, M. Straka, M. Kaupp, and R. Marek. "Relativistic Heavy-Neighbor-Atom Effects on NMR Shifts: Concepts and Trends Across the Periodic Table." In: *Chemical Reviews* 120.15 (2020), pp. 7065–7103. DOI: `10.1021/acs.chemrev.9b00785`.

[166] G. Waldherr, J. Beck, M. Steiner, P. Neumann, A. Gali, T. Frauenheim, F. Jelezko, and J. Wrachtrup. "Dark States of Single Nitrogen-Vacancy Centers in Diamond Unraveled by Single Shot NMR." In: *Phys. Rev. Lett.* 106 (15 2011), p. 157601. DOI: `10.1103/PhysRevLett.106.157601`.

[167] J. Wang et al. "Coherence times of precise depth controlled NV centers in diamond." In: *Nanoscale* 8 (10 2016), pp. 5780–5785. DOI: `10.1039/C5NR08690F`.

[168] T. Wolf, P. Neumann, K. Nakamura, H. Sumiya, T. Ohshima, J. Isoya, and J. Wrachtrup. "Subpicotesla Diamond Magnetometry." In: *Phys. Rev. X* 5 (4 2015), p. 041001. DOI: 10.1103/PhysRevX.5.041001.

[169] A. A. Wood, A. Lozovoi, R. M. Goldblatt, C. A. Meriles, and A. M. Martin. "Wavelength dependence of nitrogen vacancy center charge cycling." In: *Phys. Rev. B* 109 (13 2024), p. 134106. DOI: 10.1103/PhysRevB.109.134106.

[170] K. Wuthrich. *NMR of proteins and nucleic acids*. 1988.

[171] M. Xie, X. Yu, L. V. H. Rodgers, D. Xu, I. Chi-Durán, A. Toros, N. Quack, N. P. de Leon, and P. C. Maurer. "Biocompatible surface functionalization architecture for a diamond quantum sensor." In: *Proceedings of the National Academy of Sciences* 119.8 (2022), e2114186119. DOI: 10.1073/pnas.2114186119.

[172] F. Xue, D. P. Weber, P. Peddibhotla, and M. Poggio. "Measurement of statistical nuclear spin polarization in a nanoscale GaAs sample." In: *Phys. Rev. B* 84 (20 2011), p. 205328. DOI: 10.1103/PhysRevB.84.205328.

[173] J. Zhang, T. Liu, L. Xu, G. Bian, P. Fan, M. Li, C. Xu, and H. Yuan. "A pulsed lock-in method for DC ensemble nitrogen-vacancy center magnetometry." In: *Diamond and Related Materials* 125 (2022), p. 109035. DOI: 10.1016/j.diamond.2022.109035.

[174] J. Zhang, L. Xu, T. Shi, G. Bian, P. Fan, M. Li, P. Chen, C. Xu, N. Zhang, and H. Yuan. "An improved spin readout for nitrogen vacancy center ensemble based on a maximum likelihood estimation method." In: *Journal of*

Physics D: Applied Physics 53 (45 2020), p. 455305. DOI: 10.1088/1361-6463/aba7de.

[175] J. Zhang et al. “Efficient Real-Time Spin Readout of Nitrogen-Vacancy Centers Based on Bayesian Estimation.” In: *IEEE Transactions on Industrial Electronics* (2024), pp. 1–10. DOI: 10.1109/TIE.2023.3347837.

[176] M. Zhang, B.-Y. Li, and J. Liu. “Monitoring Dark-State Dynamics of a Single Nitrogen-Vacancy Center in Nanodiamond by Auto-Correlation Spectroscopy: Photonionization and Recharging.” In: *Nanomaterials* 11.4 (2021). DOI: 10.3390/nano11040979.

[177] B. Zhao, Y. Dong, S. Zhang, X. Chen, W. Zhu, and F. Sun. “Improving the NV generation efficiency by electron irradiation.” In: *Chin. Opt. Lett.* 18.8 (2020), p. 080201. DOI: 10.1364/COL.18.080201.

[178] Z. Zhao, X. Ye, S. Xu, P. Yu, Z. Yang, X. Kong, Y. Wang, T. Xie, F. Shi, and J. Du. “Sub-nanotesla sensitivity at the nanoscale with a single spin.” In: *National Science Review* 10.12 (Apr. 2023), nwad100. DOI: 10.1093/nsr/nwad100.

[179] W. Zheng, K. Bian, J. Xu, X. Chen, S. Zhang, R. Stöhr, A. Denisenko, J. Wrachtrup, S. Meng, and Y. Jiang. “Probing Interfacial Water Dissociation at the Nanoscale with a Quantum Sensor.” In: *Phys. Rev. Lett.* 135 (20 2025), p. 208001. DOI: 10.1103/gpcy-lnc2.

[180] F. Ziem, M. Garsi, H. Fedder, and J. Wrachtrup. “Quantitative nanoscale MRI with a wide field of view.” In: *Scientific Reports* 9.1 (2019), p. 12166. DOI: 10.1038/s41598-019-47084-w.

COLOPHON

This document was typeset using LaTeX and BibTeX with the typographical look-and-feel `classicthesis` developed by André Miede.